Journal of Chemistry

Chemistry of the Built Environment

Lead Guest Editor: Carlos Alves
Guest Editors: Jorge Sanjurjo-Sánchez and Carlos Figueiredo

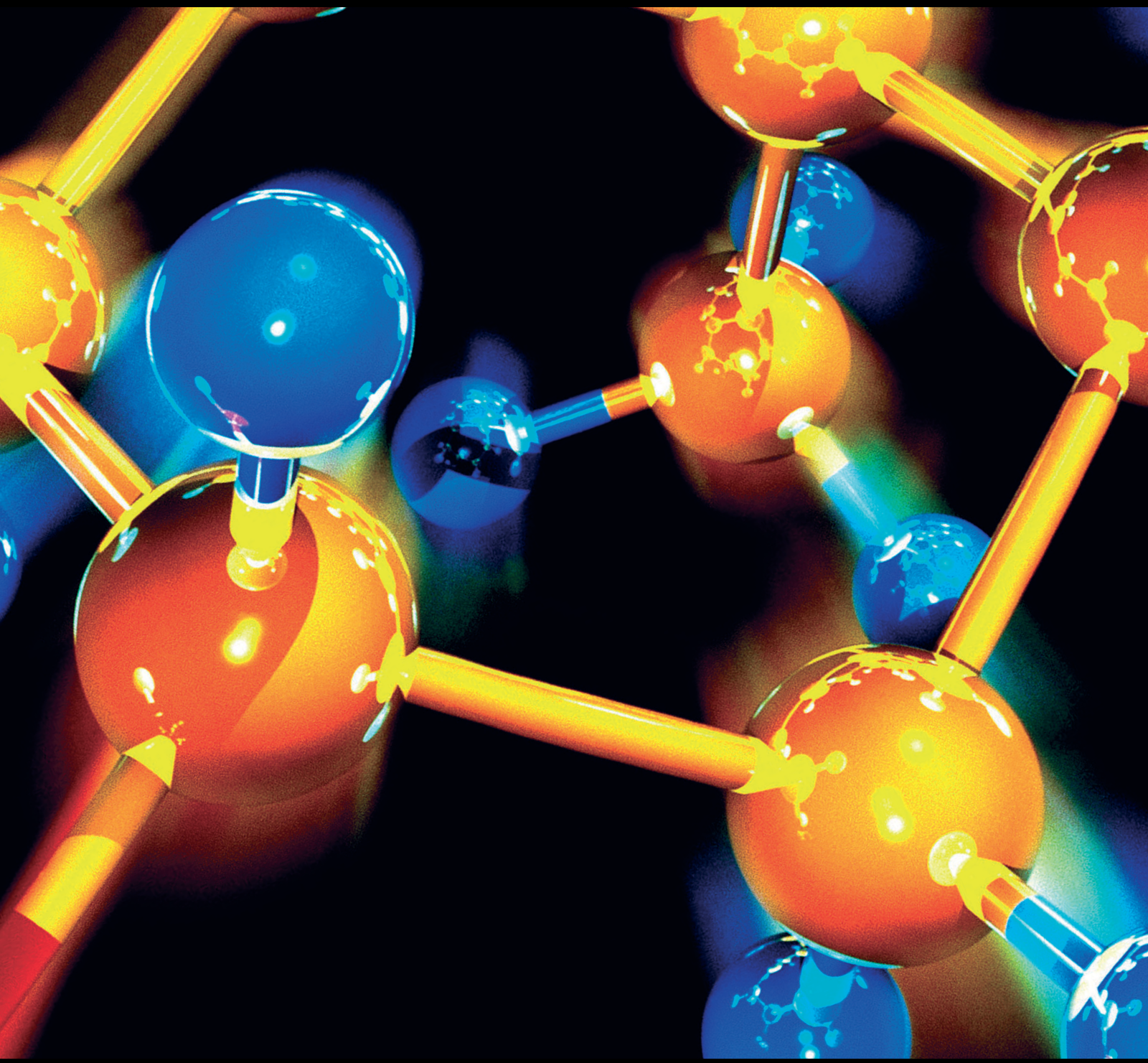

Chemistry of the Built Environment

Journal of Chemistry

Chemistry of the Built Environment

Lead Guest Editor: Carlos Alves
Guest Editors: Jorge Sanjurjo-Sánchez and Carlos Figueiredo

Contents

Hindawi
Journal of Chemistry
Volume 2020, Article ID 5304745, 10 pages
https://doi.org/10.1155/2020/5304745

Research Article

Physicochemical Properties of Hydrated Portland Cement Blended with Rice Husk Ash

Joseph Mwiti Marangu,[1] **Cyprian Muturia M'thiruaine**,[1] **and Mark Bediako**[2]

[1]*Department of Physical Sciences, Meru University of Science & Technology, Meru, Kenya*
[2]*Advanced Material Science Division, CSIR-Building and Road Research Institute, Kumasi, Ghana*

Correspondence should be addressed to Joseph Mwiti Marangu; jmarangu2011@gmail.com

Received 26 April 2020; Revised 6 November 2020; Accepted 21 November 2020; Published 8 December 2020

Academic Editor: Carlos Figueiredo

In the presence of significant quantities of carbon dioxide (CO_2) and elevated temperatures in the atmosphere due to climate change, cement-based materials are susceptible to carbonation. Blended cements are more prone to carbonation attack than Portland cement. There is a need to evaluate the carbonation resistance of blended cements in a carbonation-prone environment. This paper presents experimental findings obtained from an evaluation of carbonation resistance tests on Rice Husk Ash- (RHA-) blended cement. The blended cement was made by intergrinding of Portland Cement (PC) and RHA to make the test cement (PC-RHA). The RHA dosage in the PC-RHA was varied from 0 to 30% by mass of PC. Pozzolanicity, standard consistency, and setting time tests were conducted on PC-RHA. Mortar prisms measuring 160 mm × 40 mm x 40 mm were separately cast at a water/cement ratio (w/c) of 0.50 and 0.60 and cured in water for 2, 7, 14, 28, and 90 days. Compressive strength tests were conducted on the mortar prisms at each of the testing ages. The prepared mortars were also subjected to accelerated carbonation tests in two Relative Humidity (RH) curing regimes, one maintained at an RH greater than 90% and the other between 50–60%. Carbonation resistance of the mixtures was evaluated in terms of the changes in carbonation depth using a phenolphthalein test at the age of 7, 14, 28, and 56 days of curing in a continuous flow of CO_2. Compressive strength measurements were also taken during each of the carbonation testing ages. For comparison, similar tests were conducted using commercial PC. The results showed that PC-RHA was pozzolanic while PC was nonpozzolanic. Higher water demand and longer setting times were observed in PC-RHA than in PC. Moreover, there was increased strength development in water-cured samples with increased curing duration. Carbonation results indicated that there was a marked increase in carbonation depth with increased dosage of RHA in PC-RHA binders, increased duration of exposure to CO_2, and decreased RH (RH between 50–60%). PC-RHA binders exhibited lower carbonation resistance than PC. In conclusion, for mortars at any w/c ratio, carbonation resistance decreased with increase in RHA dosage and increased w/c ratio.

1. Introduction

Presently, there is an increase in greenhouse gas emissions, mainly anthropogenic CO_2, hence adversely affecting the earth's climate [1–3]. Recently, the global average surface air temperature has been reported to have increased [4, 5]. Rising sea levels, decreased snowpacks, and increased glacial melting increased heat waves and drought occurrences and increased extreme precipitation events, leading to increased flood risks in Africa and the rest of the world [6, 7]. As a consequence, the risks of decreased global food production potential for extinction of biodiversity are some of the potential effects of climate change in the world. However, limited attention has been paid to the effect of climate change on cement-based structures [8, 9].

Cement-based structures represent the major components of the built environment [10]. There is a growing need to evaluate the impact of climate change on our cement-based infrastructure. Reinforced concrete structures form an essential part of our world. Climate change has the potential to impact negatively on the durability of a cement-based infrastructure [8, 11]. There is need to recognize the effects that global climate change may have on a cement-based infrastructure in order to develop resilient construction

materials [12]. Due to climate change, there is a prevalence of significant quantities of carbon dioxide (CO_2) and elevated temperatures in the atmosphere, and under these conditions, cement-based materials are susceptible to carbonation [13, 14]. Carbonation of cementitious materials occurs due to a reaction between atmospheric CO_2 and the hydrated phases of cement, leading to a drop in its pH [15]. In reinforced concrete, a drop in pH of pore water leads to the depassivation of embedded rebar. Increased carbonation rates of reinforced concrete structures are expected as a result of increased temperatures and CO_2 concentrations, with the enhanced risk of carbonation-induced corrosion likely affecting the service life of cement-based structures. Therefore climate change may alter the ambient construction environment, especially in the longer-term, causing acceleration of carbonation-induced corrosion that leads to cracking and spalling, which result in more costly and disruptive repairs and maintenance activities, as well as strength loss of concrete structures [16].

Portland Cement (PC) is the main binder used in building and construction worldwide [17]. However, the manufacture of PC is an intensive process both in terms of raw material acquisition and energy. In the process, about 5% of carbon dioxide (CO_2) is emitted into the atmosphere. CO_2 is the main greenhouse gas mainly responsible for global warming and climate change [2]. In addition, due to the high energy demand associated with the production of PC, the resultant cement is expensive, especially to low-income earners. Blending of PC with pozzolanic materials has been found to be an innovative strategy to lower the cost of cement and reduce the amount clinker and, hence, lower CO_2 emission [18–20]. However, blended cements have been found to be susceptible to carbonation than PC due to lower amounts of calcium hydroxide (CH) in their hydrated phases [13, 21, 22]. Therefore, the performance of blended cements must be properly investigated to validate their application in carbonation-prone areas such as coastal and offshore regions and in present atmospheric conditions marked with increased CO_2 emission.

Increased demand for low-cost and environment-friendly cement has increased the demand for supplementary cementitious materials [23]. Rice is an agricultural crop produced in vast quantities globally [24]. Large amount of Rice Husks (RH) generated in the world is mostly burnt in open fields leading to environmental pollution, and the resultant Rice Husk Ash (RHA) is not beneficial to the soil. This is because the silica in RHA is in an unreactive and nonabsorbable form. This results in the use of RHA in land filling as a method of disposal. However, RHA has the potential to meet the growing need for production and use of sustainable construction materials in the world if used as a pozzolana in the manufacture of blended cements [25–30]. The durability of cement-based structures is a global pervasive problem. In view of changing environmental conditions due to climate change, there is a need to evaluate the performance of blended cements in aggressive media such as carbonation-prone environments [31, 32]. The carbonation-induced corrosion is the major cause of degradation and subsequent reduction in the service life of cement-based materials and increased maintenance-related costs more so in structures located in coastal and offshore regions [33, 34]. Replacement of clinker with RHA is recently gaining the world attention as a viable option to lower the cost of cement and promote environmental conservation. However, increased substitution of clinker in cement with RHA has the potential to increase the susceptibility of the resulting cement-based structure to carbonation attack mostly due to prevalence of high quantities of CO_2 and elevated temperatures in the atmosphere due to climate change. It is, therefore, important to evaluate the robustness of PC-RHA cement blend under carbonation conditions to validate its applicability in such aggressive media. In this study, carbonation resistance of blended cement by intergrinding of Ordinary Portland Cement (PC) and Rice Husk Ash to make the test cement (PC-RHA) was investigated. The study aimed to evaluate the performance of a rice husk ash-based cement under ambient and severe carbonation conditions.

2. Materials and Methods

2.1. Materials. Rice Husk (RH) was obtained from a rice processing plant located at Mwea town, Kirinyaga County, Kenya. The RH was incinerated at 600°C for 3 hours using a Muffle furnace model number OSK 9540-MK-SP 38351 to obtain RHA which was used as a pozzolana in the preparation of blended cement. Requisite amounts of RHA and PC were mechanically mixed in an automatic mixer to make PC-RHAs at 0, 10, 15, 25, and 30 percent substitution of PC by mass. Commercial 42.5 N Portland Cement (PC) was supplied by East Africa Portland Cement, located in Athi River, Machakos County, Kenya.

Brunauer–Emmett–Teller (BET) testing was used to evaluate the surface area of RHA. In this test, Nitrogen adsorption-desorption measurements were conducted at 77 K on a Micromeretics Tristar 3000 apparatus to determine the Brunauer–Emmett–Teller (BET) surface area. Prior to measurements being taken, samples were dried at 105°C and kept in a desiccator until testing. In addition, the samples were cooled with liquid nitrogen and analyzed by measuring the volume of gas (N_2) adsorbed at specific pressures. The BET adsorption theory was used for the determination of surface area, using the corresponding values of the relative pressure between 5-35% of the adsorption curve assuming that there was complete pore saturation.

The composition of RHA- and PC-RHA-blended cements used in this study is given in Table 1.

2.2. Methods

2.2.1. Pozzolanicity Test. A saturated lime test was used to assess the pozzolanic activities of the test cements [35]. The testing reagents were prepared by separately dissolving requisite amounts of ethylenediaminetetraacetic acid disodium salt dehydrate (EDTA), concentrated HCl, and NaOH in water to make 0.025M EDTA, 0.1M HCl, and 5M NaOH solutions, respectively. The 0.025M EDTA solution was standardized against dried calcium carbonate while 0.1M HCl was standardized against dried sodium carbonate. Murexide indicator

Table 1: Composition and physical properties of RHA and PC.

Composition	RHA	PC
SiO_2	82.43	20.28
Al_2O_3	1.35	4.98
Fe_2O_3	1.28	3.42
CaO	1.22	62.97
MgO	1.97	2.65
SO_3	0.18	2.75
K_2O	2.51	0.28
Na_2O	0.15	0.36
LOI	2.95	1.38
BET (m^2/g)	51.4	
Blaine surface area (m^2/g)	2.31	
Specific gravity	2.12	2.95

was prepared by intergrinding 0.5 g of murexide and 100 g of dried potassium chloride using a pestle and mortar.

Curing of the test sample for the test was performed by pipetting 100 ml of freshly boiled water into a 0.5 litre plastic container and the sealed container placed in a thermostatic enclosure at $40 \pm 0.2^{\circ}$C until equilibrium was reached in about an hour. The container was removed from the thermostatic enclosure, and 20.00 g of test cement was poured into it using a wide funnel. The container was then immediately sealed and shaken vigorously for about 20 seconds. A horizontal rotary motion was adopted, thus preventing any sample or liquid from being thrown up and remaining separated from the rest of the solution. The container was then placed back in the thermostatic enclosure. After a period of testing (3, 8, 21, or 28 days), the container was removed from the enclosure and filtered immediately under vacuum. A Butchner funnel, a vacuum flask, and dry Whatmann filter paper were used for the filtration. The flask was then sealed immediately to avoid carbonation. The filtrate was allowed to cool to room temperature in about ten minutes.

To determine the concentration of the OH^- ions, 50 ml of the filtrate were pipetted into a 250 ml conical flask, and about five drops methyl orange indicator was added. The resulting solution was titrated against 0.1M HCl. The OH^- concentration in millimoles per litre was calculated using the following equation:

$$[OH^-] = \frac{1000 \times 0.1 \times V}{50}, \quad (1)$$

where V is the volume of the 0.1M HCl used for the titration.

To determine the concentration of CaO, about 5 ml of 5 M NaOH and 50 mg of the murexide indicator were added to a measured solution that remained after completion of OH^- determination. The resulting solution was titrated against the 0.025 M EDTA solution. During titration, the pH of the solution was maintained at 13 by the addition of the NaOH solution. The pH was monitored using a pH meter. The concentration of $Ca(OH)_2$ was calculated using the following equation:

$$[CaO] = \frac{1000 \times .025 \times V}{50}, \quad (2)$$

where, in this case, V is the volume of the EDTA solution used for the titration.

2.2.2. Standard Consistency. Standard consistency was determined in accordance with the KS EAS 148-3:2000. In this test, about 500 g of test cement was weighed and a known quantity of water was added and mixed thoroughly for about 5 minutes on a nonporous surface using two trowels to avoid loss of water or cement. The paste was transferred to the Vicat apparatus, was placed on a lightly greased plane glass base plate, and was filled to excess without compacting or vibrating. The excess paste was removed by a gentle sawing motion with a straight edge. The Vicat apparatus was then calibrated with a plunger by lowering the plunger to rest on the base plate which was used to adjust the pointer to read zero on the scale. The plunger was later raised to the standby position. The mould and the base plate were transferred to the Vicat apparatus immediately after levelling the paste and were positioned centrally under the plunger. The plunger was then lowered gently until it came in contact with the paste.

The plunger was allowed to pause in that position for about two seconds so as to avoid initial velocity. The moving parts were released quickly, and the plunger was allowed to penetrate vertically into the centre of the paste. The scale was read when penetration ceased. The recorded scale reading indicated the distance between the bottom face of the plunger and the base plate. The water content of the paste was expressed as a percentage by mass of the various cement categories. The plunger was cleaned, and the process was repeated with pastes containing different water contents determining to find the one that would produce a distance between plunger and base plate of 6 ± 2 mm; the water content of this paste was calculated as a percentage by mass and was recorded as water that was required for standard consistency.

2.2.3. Setting Time. The setting time of test cement was determined in accordance with the KS EAS 148-3:2000. In this method, the Vicat apparatus were used for the determination of both initial and final setting times of the samples. For the determination of initial setting time, the calibrated Vicat apparatus were used. The needle with a diameter 1 mm (0.04 inch) was lowered to rest on the base plate used, and the pointer was adjusted to read zero from the scale. The needle was raised to a standby position which was followed by filling the Vicat mould with the paste under a prescribed standard consistency. The filled mould and paste were placed in the curing room, and after 45 minutes, they were transferred and positioned under the needle. The point at which the needle penetrated to a point of 5 mm (0.2 inch) from the bottom of the mould after adding water to the cement signalled that the initial set had occurred and was taken as the initial setting time. KS EAS 18 : 2001 prescribes a minimum initial setting time of 75 minutes for Portland pozzolana cements.

Final setting time was determined using the replacement needle with a hollow circular metal attachment of diameter 5 mm and was set 0.5 mm behind the tip of the needle. The

filled mould and the base plate were placed in the room after determination of the initial setting time. After 30 minutes, it was transferred and positioned under the needle. The final set occurred when the needle circular ring would fail to make a mark on the paste, and the time was recorded from the zero scale of the Vicat apparatus. KS EAS 18 : 2001 prescribes 600 minutes as the maximum final setting time for Portland pozzolanic cement.

2.2.4. Compressive Strength. Compressive strength for the mortars was determined in accordance to KS EAS 148-1: 2000. From each cement category, three mortar prisms measuring 160 mm × 40 mm *x* 40 mm were separately cast at a water/cement ratio (w/c) of 0.50 and 0.60 and cured in water for 2, 7, 14, and 28 days. Compressive strength tests were conducted on the mortar prisms at each of the testing ages using the compressive machine. The prisms were tested for compressive strength using a compressive strength machine model number SSC-546 following the instructions on the instrument manual. Average of triplicate measurements was taken as the final compressive strength.

2.2.5. Carbonation Test. Accelerated carbonation tests were performed on cement mortars prepared from each test cement. For each type of cement, at a particular w/c ratio, six mortar prisms measuring 40 mm × 40 mm × 160 mm were cast. The prisms were placed in a curing chamber maintained at 23 ± 1°C and a relative humidity greater than 90% for 24 hours. After 24 hours ± 30 minutes, the specimens were demoulded and marked accordingly for identification purposes. Half of the specimens were placed in the humidity chamber maintained at 23 ± 1°C and 50–60% relative humidity in a closet for 14 days. Another half of the specimens was placed in the humidity chamber maintained at 23 ± 1°C and relative humidity greater than 90% for 14 days as well.

After 14 days of curing, all specimens were introduced into the closed box which had a continuous flow of CO_2. At the age of 7, 14, 28, and 56 days, the specimens were taken out from the box and each specimen was broken longitudinally into half. The weight and compressive strength measurements were taken on each specimen. The depth of carbonation was measured by taking measurements over multiple points perpendicular to the edges of the split face after application of a phenolphthalein indicator solution on each half of the broken prism.

3. Results and Discussions

3.1. Pozzolanic Activity. The pozzolanic activity was used to measure the degree of reaction between an RHA and $Ca(OH)_2$ in the presence of water at ambient temperature. The quantity of $Ca(OH)_2$ in the test cement solution was evaluated in terms of the concentration of CaO and OH^- at different curing durations, as shown in Figures 1 and 2, respectively. Generally, the lower the resulting quantity of CaO and OH^-, the higher the pozzolanicity, and vice versa.

In both Figures 1 and 2, a progressive decrease in the concentration of CaO and OH^- was observed in all the

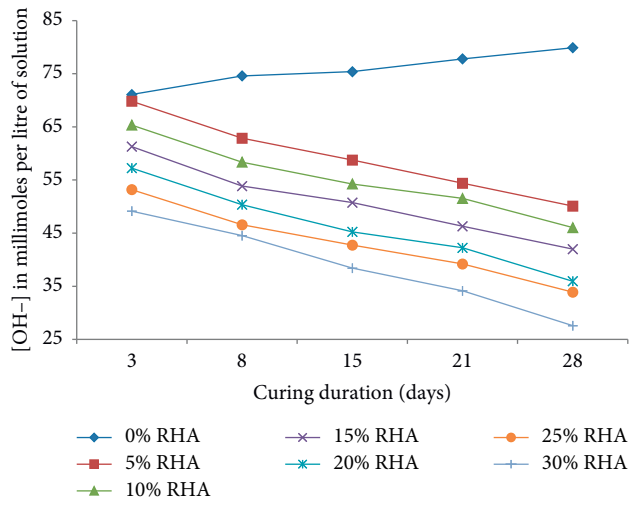

Figure 1: Concentration of OH^- in RHA-PC-blended cements.

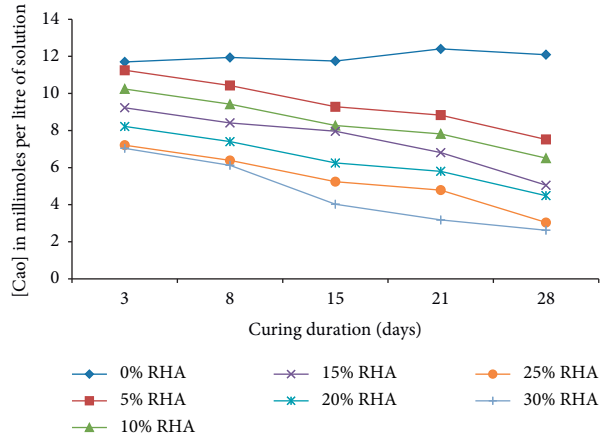

Figure 2: Concentration of CaO in RHA-PC-blended cements.

RHA-PC-blended cements and decreased in PC with increased curing duration. This can be attributed to the differences in their cement hydration processes. During the hydration process in PC, C_3S and C_2S undergo hydration reactions to produce CH as shown in the following equations:

$$2C_3S + 6H \longrightarrow 3CSH + 3CH \quad (3)$$

$$2C_2S + 4H \longrightarrow 2CSH + 2CH \quad (4)$$

The CSH formed in equations (3) and (4) is mainly responsible for strength development in the cement-based structures. The increase in concentration of CaO and OH- in PC can be attributed to the production of CH with continued curing.

Conversely, the decrease in concentration of OH^- and CaO can be attributed to the consumption of CH during the pozzolanic reaction in RHA-blended cements. RHA contains amorphous silica and alumina and, therefore, exhibits pozzolanic properties. During the pozzolanic reaction, the hydration of PC produces CH which reacts with silica and

alumina present in RHA as shown in the following equations:

$$3CH + S + H \longrightarrow CSH \quad (5)$$

$$A + H + CH \longrightarrow CAH \quad (6)$$

Increased curing period results in higher consumption of CH in pozzolanic reactions and results in progressive decrease in the amount of CH in the hydrated RHA-blended cement matrix.

It was observed that the concentration of OH^- and CaO decreased with increase in the amount of RHA added. This could be possibly due to the fact that increased amount of RHA introduced more amorphous silica and alumina in RHA-blended cement mixtures. Increased availability of amorphous silica and alumina results in greater pozzolanic activity. In conclusion, RHA was found to exhibit pozzolanic properties.

3.2. Standard Consistency. The standard consistency as a function of percentage replacement of RHA of the test cements is presented in Figure 3.

It was observed that the standard consistency of RHA-blended cements increases from 25.10 to 35.52 percent as RHA replacement increased from 0 to 30 percent. Increase in standard consistency with increase in RHA addition can be attributed to the high fineness and surface area of RHA. According to Raheem and Kareem [36], RHA is considered hygroscopic; hence, more water is required for wetting the particles as the total specific surface of the particle increases.

3.3. Setting Time. The initial and final setting time of RHA-blended cements are presented in Figure 4.

PC (0% RHA) exhibited shorter initial and final setting time than RHA-blended cements. This could be attributed to higher content of clinker phases (C_3S and C_3A) in PC (0%RHA) than in the other blended cements. C_3S hardens rapidly in the presence of water; hence, it is responsible for the early setting of cement paste. Hydration of C_3A produces significant amount of heat that increase the prevailing setting temperature resulting to faster setting behaviour of PC (0%RHA) compared with blended cements. The setting time of cement decreases with a rise in temperature. Moreover, the slow pozzolana reactions that take place in RHA-blended cements result in slow cement hydration and, hence, increased setting times [37].

It was observed that both initial and final setting time of RHA-blended cements were observed to increase with increase in addition of RHA in the order% 0 RHA< 5% RHA< 10% RHA <20% < 25 RHA< 30% RHA. This is could be attributed to the increased quantity of RHA added at 0, 5, 10, 15, 20, 25, and 30 percent, respectively. Increase in the content of RHA incorporated in the RHA-blended cements resulted to longer initial and final setting times, perhaps due to the fact that the increased addition of RHA in RHA-blended cements progressively

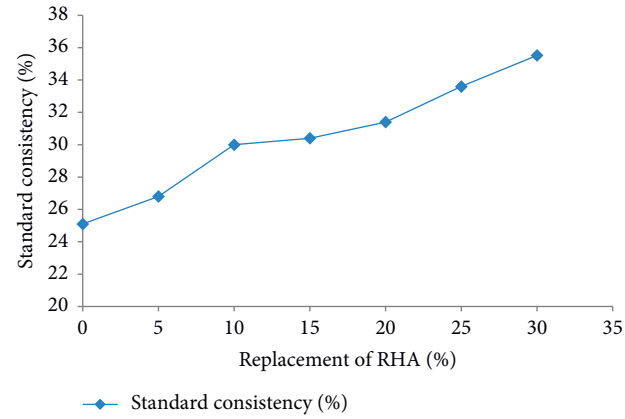

Figure 3: Standard consistency as a function of percentage replacement of RHA.

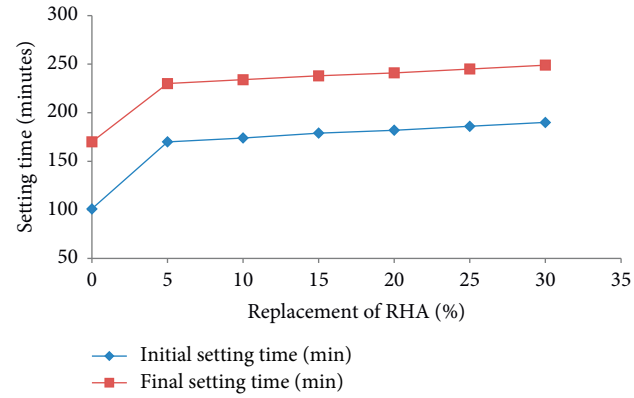

Figure 4: Setting time of RHA-blended cements at different replacements of RHA.

reduced the amounts of C_3S and C_3A components resulting in the slow setting of these cements.

In conclusion, the EAS 148-3:2000 prescribes that blended cements should have setting times of between 180 ± 10 minutes and 240 ± 10 minutes while PC should be between 100 ± 10 minutes and 170 ± 10 minutes for initial and final setting times, respectively. All the test cements conformed to this specification. Generally, for each cement category, nonblended cement exhibited shorter setting time than RHA-blended cements.

3.4. Compressive Strength. The compressive strength results for various RHA-blended cements at different curing duration and *w/c* are shown in Figure 5.

Compressive strength increased with increased duration of curing for all the RHA-blended cements. This can be attributed to the hydration reactions occurring in the hydrated cement matrix resulting in the formation of CSH, as shown in equations (3) and (4). The reference nonblended binder (0% RHA) exhibited higher compressive strength than the other RHA-blended cements at all the *w/c* ratios. This can be attributed to the fact that the 0% RHA contained the highest proportion of PC; hence, the clinker phases (C_3S and C_2S) which are mainly responsible for strength are

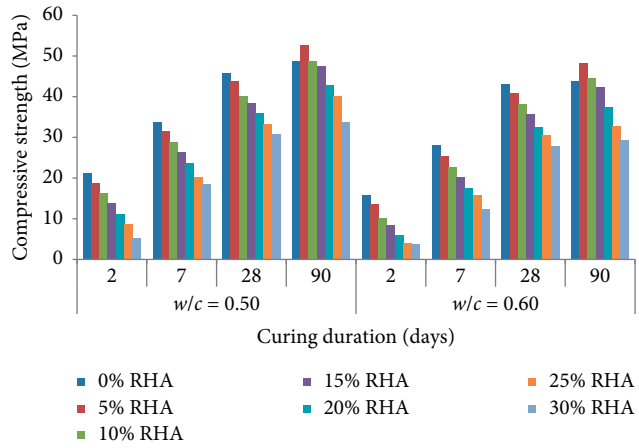

Figure 5: Compressive strength verses curing duration for RHA-blended cement.

relatively high in proportion compared to the RHA-blended cements mixtures [23, 38]. Similarly, there was a progressive decrease in compressive strength with increased substitution of PC with RHA due to the progressive decrease in the amount of PC in RHA-blended cements at all the w/c ratios. This implied that the added RHA did not contribute to strength development but was mainly a filler material in mortar.

At each curing age, an increase in w/c ratio resulted in decrease in compressive strength of all cements considered. The strength decreased in the order $w/c = 0.50 > w/c = 0.60$. w/c ratio is considered as the most important factor affecting mortars/concrete strength. This is because it affects the porosity of the hardened paste. Increased quantity as a result of use of high w/c ratio also affects the flow or rheology of the mixture, as well as cohesion between paste and aggregate. High w/c increases the voids and reduces the cohesion in the mortar matrix, and as a result, it reduces the overall strength of the mortar [39].

In conclusion, the KS EAS 18:1-2001 requires that blended cements should have a minimum compressive strength of 32.5 MPa at 28 days of curing. The RHA-blended cements satisfied this requirement up to 20 percent of replacement with RHA.

3.5. Carbonation

3.5.1. Depth of Carbonation. The carbonation depth obtained from the phenolphthalein test profiles for various RHA-blended cement mixtures at different humidity regimes is given in Figure 6.

It was observed that carbonation depths in mortars cured at 50–60 percent relative humidity was greater than that found in mortars cured at 90 percent relative humidity. The differences in relative humidity during curing explain the difference in carbonation depths observed. In the presence low relative humidity (50–60 percent), mortars were relatively dry; hence, the penetration of carbon dioxide in the mortar matrix is high resulting in greater depths of carbonation than at high relative humidity (90 percent). At low humidity, the hydration of cement is poor due to insufficient moisture; hence, limited hydration of cement occurs resulting in the formation of low amounts of CSH and calcium hydroxide (CH) [13, 14, 40, 41]. CH binds the ingressed carbon dioxide, preventing further penetration into the mortar. Low quantities of CSH result in a very porous hydrated mortar matrix which increases the permeability of hardened cement and allows greater depth of CO_2 penetration. On the other hand, at high RH, the mortars were relatively wet; hence, greater amount of CSH is formed, thus reducing the porosity of the hydrated mortars. Low porosity leads to low permeability of the hydrated mortars and, hence, low CO_2 penetration [13, 42].

It was observed that the depth of carbonation also increased with increase in the curing period for all the cement categories considered. Increase in curing duration has been found to effectively increase the extent of carbon dioxide penetration in the mortars [43]. Similar observations were made by Balayssac et al. [44] while studying the effects of curing upon carbonation of concrete.

RHA-blended cement (5% RHA and 20% RHA) mortars exhibited higher depth of carbonation than OPC mortars (0% RHA-blends). This can be attributed to the fact that blended cements contain lower quantities of $Ca(OH)_2$ than 0%RHA mortars. The SiO_2 and Al_2O_3 in the calcined clays react with $Ca(OH)_2$ resulting from the hydration of Portland cement. As a consequence, the blended cement leads to a lower $Ca(OH)_2$ content in the hardened cement paste so that a smaller amount of CO_2 is required to remove all the $Ca(OH)_2$ by producing $CaCO_3$ during carbonation [45–47]. Therefore, the depth of carbonation was observed to be greater in blended cements since the amount of $Ca(OH)_2$ present was lower. It follows that the presence of RHA resulted in a more rapid carbonation. In a related study [48], it was observed that PC showed shorter depth of carbonation than blended cements. The workers attributed this to the differences in the content of $Ca(OH)_2$ present in both PC and blended cements.

There was a slight increase in the depth of carbonation with increase in w/c. The depth of CO_2 penetration increased in the order $w/c = 0.50 < w/c = 0.60$. This can be attributed to the fact that increased w/c results in increased permeability

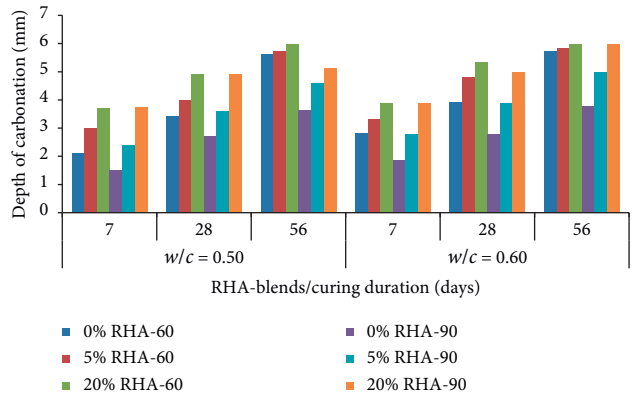

Figure 6: Depth of carbonation at different curing periods verses RHA-blends.

of the hydrated mortar matrix and, thus, higher penetration of CO_2 [11, 41, 49–51].

3.5.2. Effects of Carbonation on Compressive Strength. The compressive strength development for various RHA-blended cement mortars exposed to different curing humidity is shown in Figure 7.

Higher compressive strengths were observed in mortars cured at 90 percent than their corresponding mortars cured at 60 percent relative humidity. This can be attributed to the different curing humidity conditions that the mortars were subjected to. Low humidity (60 percent) allows more ingress of CO_2 than mortars cured at high humidity (90 percent) [41]. CH which is one of the products formed during hydration of cement readily reacts with CO_2 resulting in precipitation of sparingly soluble calcium carbonate ($CaCO_3$) as shown in the following equations [52–55]:

$$CO_2 + Ca(OH)_2 \longrightarrow CaCO_3 + H_2O \quad (7)$$

$$CSH + CO_2 \longrightarrow SiO_2 + 2CaCO_3 + H_2O \quad (8)$$

Equation (7) represents the moderate carbonation process that occurs on the surface layer of cement-based materials leading to the formation of $CaCO_3$. The $CaCO_3$ formed is deposited on the pore network in the hydrated cement matrix resulting in pore refinement of the carbonated layer [56–60]. This is beneficial since pore refinement subsequently results in increased strength, reduced porosity, and improved durability of hydrated cement. This explains why there was an increase in compressive strength of mortars with continued curing when exposed to a CO_2-laden environment [60]. Conversely, equation (8) shows that continued ingress of CO_2 attacks CSH resulting in its disintegration, and subsequent loss of strength in cement-based structures mostly occurs if there is low RH. This explains why mortars cured at 60% RH exhibited lower compressive strength than those cured at 90% RH [13, 61].

During carbonation, OH^- present in CH is consumed resulting in the decrease of pore solution pH. In case of reinforced concrete, reduction in the pH value leads to the destruction of the protective passive surface layer around steel

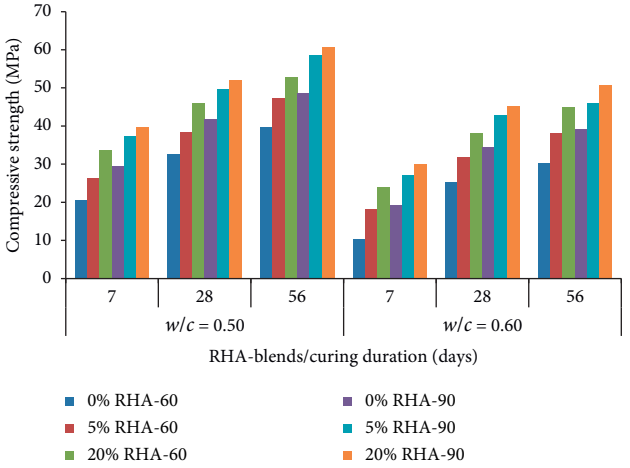

Figure 7: Compressive strength development at different curing durations verses RHA-blends type.

reinforcement resulting in rebar corrosion [15, 61, 62]. In areas with high concentration of dissolved CO_2, for example, in estuaries, the effects of carbonation are more deleterious since carbonic water is more acidic in seawater than in fresh water [63]. This can be worsened by the decaying organic matter releasing CO_2 [63]. The carbonation-related chemical reactions that result in the degradation of cement-based materials due to dissolved CO_2 are presented as follows [13, 13]:

$$CO_2 + H_2O \longrightarrow H_2CO_3 \quad (9)$$

$$H_2CO_3 + H_2O \longrightarrow HCO_3^- + H_3O^+ \quad (10)$$

$$HCO_3^- + H_2O \longrightarrow CO_3^{2-} + H_3O^+ \quad (11)$$

$$H_2CO_3 + Ca(OH)_2 \longrightarrow CaCO_3 + 2H_2O \quad (12)$$

$$CaCO_3 + H_2CO_3 \longrightarrow Ca(HCO_3)_2 \quad (13)$$

Equation (9) represents the formation of carbonic acid (H_2CO_3) from dissolved CO_2 present in the pore solution or

due to decaying organic matter or polluted water bodies. Based on equations (10) and (11), H_3O^+ produced results in significant reduction in the pH of the pore solution in the hydrated cement matrix [63]. Reduction in the alkalinity of the pore solution is deleterious since it results in carbonation-induced corrosion of rebars through dissolution of its passive surface layer. In addition, equations (12) and (13) show that significant penetration of CO_2 results in the conversion of insoluble $CaCO_3$ to soluble $Ca(HCO_3)_2$ which is easily leached out, thus decreasing porosity and subsequent strength of hydrated cements [13]. This explains why continued exposure of mortar prisms results in progressive loss of strength.

4. Conclusions

The following conclusions can be drawn from the study:

(1) The RHA-blended cement was pozzolanic while PC used was nonpozzolanic. This shows that the blended RHA was reactive.

(2) RHA-blended cement satisfied the EAS 18:1-2001 standards for blended cements up to 20 percent substitution with RHA. This implied that the RHA was a potential pozzolanic material for the production of blended cement.

(3) Nonblended cements (0% RHA) exhibited greater resistance to carbonation at all the *w*/*c* ratios used than RHA-blended cement. Therefore, one needs to be cautious if the RHA-blended cements are considered for application in CO_2-rich areas such as estuaries or marine construction activities.

(4) all the mortars at any *w*/*c* ratio, carbonation resistance decreased with increase in RHA dosage and increased *w*/*c* ratio. This is mainly due to the decreased amount of calcium hydroxide in hydrated mortars as a result of pozzolana reaction. Low amount of calcium hydroxide effectively reduces the buffering capacity of hydrated cements against carbonation attack.

Data Availability

The data used to support the findings of this study can be obtained from the corresponding author upon request.

Conflicts of Interest

The authors declare that there are no conflicts of interest.

Acknowledgments

This research was financially supported by Meru University of Science & Technology Internal Research Fund. Partial funding received from Centre for Materials and Technologies (CEMATTE) is acknowledged with gratitude. The Department of Materials Testing under the Ministry of Roads in Kenya and East Africa Portland Cement Company is dully acknowledged for providing the laboratory facilities used in this research.

References

[1] S. Solomon, G.-K. Plattner, R. Knutti, and P. Friedlingstein, "Irreversible climate change due to carbon dioxide emissions," *Proceedings of the National Academy of Sciences*, vol. 106, no. 6, pp. 1704–1709, 2009.

[2] R. Andrew, "Global CO_2 emissions from cement production," *Earth System Science Data*, vol. 11, pp. 1675–1710, 2019.

[3] P. J. Rayner, M. R. Raupach, M. Paget, P. Peylin, and E. Koffi, "A new global gridded data set of CO2emissions from fossil fuel combustion: methodology and evaluation," *Journal of Geophysical Research*, vol. 115, no. 19, p. D19306, 2010.

[4] P. D. Jones, M. New, D. E. Parker, S. Martin, and I. G. Rigor, "Surface air temperature and its changes over the past 150 years," *Reviews of Geophysics*, vol. 37, no. 2, pp. 173–199, 1999.

[5] L. A. Gil-Alana, "Time trend estimation with breaks in temperature time series," *Climatic Change*, vol. 89, no. 3-4, pp. 325–337, 2008.

[6] S. I. Seneviratne, N. Nicholls, D. Easterling et al., "Changes in climate extremes and their impacts on the natural physical environment," in *Managing the Risks of Extreme Events and Disasters to Advance Climate Change Adaptation*, C. B. Field, V. Barros, T. F. Stocker, and Q. Dahe, Eds., Cambridge University Press, Cambridge, UK, 2012.

[7] H. Carcel and L. A. Gil-Alana, "Climate warming: is there evidence in Africa?" *Advances in Meteorology*, vol. 2015, pp. 1–9, 2015.

[8] B. Mizzi, Y. Wang, and R. P. Borg, "Effects of climate change on structures; analysis of carbonation-induced corrosion in reinforced concrete structures in malta," *IOP Conference Series: Materials Science and Engineering*, vol. 442, Article ID 012023, 2018.

[9] S. Talukdar and N. Banthia, "Carbonation in concrete infrastructure in the context of global climate change: model refinement and representative concentration pathway scenario evaluation," *Journal of Materials in Civil Engineering*, vol. 28, Article ID 04015178, 2016.

[10] K. L. Scrivener, V. M. John, and E. M. Gartner, "Eco-efficient cements: potential economically viable solutions for a low-CO2 cement-based materials industry," *Cement and Concrete Research*, vol. 114, pp. 2–26, 2018.

[11] A. Silva, R. Neves, and J. De Brito, "Statistical modelling of carbonation in reinforced concrete," *Cement and Concrete Composites*, vol. 50, pp. 73–81, 2014.

[12] S. Talukdar and N. Banthia, "Carbonation in concrete infrastructure in the context of global climate change: development of a service lifespan model," *Construction and Building Materials*, vol. 40, pp. 775–782, 2013.

[13] J. M. Marangu, J. K. Thiong'o, and J. M. Wachira, "Review of carbonation resistance in hydrated cement based materials," *Journal of Chemistry*, vol. 2019, pp. 1–6, 2019.

[14] A. Leemann and F. Moro, "Carbonation of concrete: the role of CO2 concentration, relative humidity and CO_2 buffer capacity," *Materials and Structures*, vol. 50, no. 1, p. 30, 2016.

[15] D. J. Anstice, C. L. Page, and M. M. Page, "The pore solution phase of carbonated cement pastes," *Cement and Concrete Research*, vol. 35, no. 2, pp. 377–383, 2005.

[16] A. Morandeau, M. Thiéry, and P. Dangla, "Impact of accelerated carbonation on OPC cement paste blended with fly ash," *Cement and Concrete Research*, vol. 67, pp. 226–236, 2015.

[17] T. R. Naik, "Sustainability of concrete construction," *Practice Periodical on Structural Design and Construction*, vol. 13, no. 2, pp. 98–103, 2008.

[18] M. Tyrer, C. R. Cheeseman, R. Greaves et al., "Potential for carbon dioxide reduction from cement industry through increased use of industrial pozzolans," *Advances in Applied Ceramics*, vol. 109, no. 5, pp. 275–279, 2010.

[19] J. M. Marangu, "Physico-chemical properties of Kenyan made calcined clay -limestone cement (LC3)," *Case Studies in Construction Materials*, vol. 12, Article ID e00333, 2020.

[20] F. Ngui Musyimi, J. M. Wachira, J. K. Thiong'o, and J. M. Marangu, "Performance of ground clay brick mortars in simulated chloride and sulphate media," *Journal of Engineering*, vol. 2019, pp. 1–12, 2019.

[21] C.-Q. Lye, R. K. Dhir, and G. S. Ghataora, "Carbonation resistance of GGBS concrete," *Magazine of Concrete Research*, vol. 68, no. 18, pp. 936–969, 2016.

[22] M. Glinicki, D. Jóźwiak-Niedźwiedzka, K. Gibas, and M. Dąbrowski, "Influence of blended cements with calcareous fly ash on chloride ion migration and carbonation resistance of concrete for durable structures," *Materials*, vol. 9, no. 1, p. 18, 2016.

[23] E. Aprianti, P. Shafigh, S. Bahri, and J. N. Farahani, "Supplementary cementitious materials origin from agricultural wastes-a review," *Construction and Building Materials*, vol. 74, pp. 176–187, 2015.

[24] H. Beidaghy Dizaji, T. Zeng, I. Hartmann et al., "Generation of high quality biogenic silica by combustion of rice husk and rice straw combined with pre- and post-treatment strategies-a review," *Applied Sciences*, vol. 9, no. 6, p. 1083, 2019.

[25] J. M. Wachira, J. K. Thiong'o, J. M. Marangu, and L. G. Murithi, "Physicochemical performance of portland-rice husk ash-calcined clay-dried acetylene lime sludge cement in sulphate and chloride media," *Advances in Materials Science and Engineering*, vol. 2019, pp. 1–12, 2019.

[26] J. James and P. K. Pandian, "Industrial wastes as auxiliary additives to cement/lime stabilization of soils," *Advances in Civil Engineering*, vol. 2016, Article ID 126739, 1 page, 2016.

[27] E. A. Basha, R. Hashim, H. B. Mahmud, and A. S. Muntohar, "Stabilization of residual soil with rice husk ash and cement," *Construction and Building Materials*, vol. 19, no. 6, pp. 448–453, 2005.

[28] S. Rukzon and P. Chindaprasirt, "Use of ternary blend of Portland cement and two pozzolans to improve durability of high-strength concrete," *KSCE Journal of Civil Engineering*, vol. 18, no. 6, pp. 1745–1752, 2014.

[29] M. Anwar, T. Miyagawa, and M. Gaweesh, "Using rice husk ash as a cement replacement material in concrete," in *Waste Management Series*, G. R. Woolley, J. J. J. M. Goumans, and P. J. Wainwright, Eds., Elsevier, Amsterdam, Netherlands, 2000.

[30] S. K. Antiohos, V. G. Papadakis, and S. Tsimas, "Rice husk ash (RHA) effectiveness in cement and concrete as a function of reactive silica and fineness," *Cement and Concrete Research*, vol. 61-62, pp. 20–27, 2014.

[31] S. A. Zareei, F. Ameri, F. Dorostkar, and M. Ahmadi, "Rice husk ash as a partial replacement of cement in high strength concrete containing micro silica: evaluating durability and mechanical properties," *Case Studies in Construction Materials*, vol. 7, pp. 73–81, 2017.

[32] J. M. Wachira, R. Wangui Ngari, J. K. Thiong'o, and J. M. Marangu, "Effect of sulphate and chloride ingress on selected cements mortar prisms immersed in seawater and leather industry effluent," *Advances in Civil Engineering*, vol. 2019, pp. 1–16, Article ID 8191689, 2019.

[33] J. A. Bogas and S. Real, "A review on the carbonation and chloride penetration resistance of structural lightweight aggregate concrete," *Materials*, vol. 12, no. 20, p. 3456, 2019.

[34] M. Sosa, T. Pérez-López, J. Reyes et al., "Influence of the marine environment on reinforced concrete degradation depending on exposure conditions," *International Journal of Electrochemical Science*, vol. 6, p. 19, 2011.

[35] S. Donatello, M. Tyrer, and C. R. Cheeseman, "Comparison of test methods to assess pozzolanic activity," *Cement and Concrete Composites*, vol. 32, no. 2, pp. 121–127, 2010.

[36] A. A. Raheem and M. A. Kareem, "Chemical composition and physical characteristics of rice husk ash blended cement," *International Journal of Engineering Research in Africa*, vol. 32, pp. 25–35, 2017.

[37] D. K. Sharma and R. Sharma, "Influence of rice husk ash and rice tiller ash along with chromate reducing agents on strength and hydration properties of ordinary portland cement," *Construction and Building Materials*, vol. 169, pp. 843–850, 2018.

[38] D. G. Nair, K. S. Jagadish, and A. Fraaij, "Reactive pozzolanas from rice husk ash: an alternative to cement for rural housing," *Cement and Concrete Research*, vol. 36, no. 6, pp. 1062–1071, 2006.

[39] A. Zhang and L. Zhang, "Influence of cement type and water-to-cement ratio on the formation of thaumasite," *Advances in Materials Science and Engineering*, vol. 2017, Article ID 7643960, 12 pages, 2017.

[40] A. Leemann, H. Pahlke, R. Loser, and F. Winnefeld, "Carbonation resistance of mortar produced with alternative cements," *Materials and Structures*, vol. 51, no. 5, p. 114, 2018.

[41] D. Russell, P. A. M. Basheer, G. I. B. Rankin, and A. E. Long, "Effect of relative humidity and air permeability on prediction of the rate of carbonation of concrete," *Proceedings of the Institution of Civil Engineers - Structures and Buildings*, vol. 146, no. 3, pp. 319–326, 2001.

[42] S. T. Pham and W. Prince, "Effects of carbonation on the microstructure of cement materials: influence of measuring methods and of types of cement," *International Journal of Concrete Structures and Materials*, vol. 8, no. 4, pp. 327–333, 2014.

[43] B. Lagerblad, *Carbon Dioxide Uptake During Concrete Life Cycle – State of The Art*, Swedish Cement and Concrete Research Institute, Borås, Sweden, 2005.

[44] J. P. Balayssac, C. H. Détriché, and J. Grandet, "Effects of curing upon carbonation of concrete," *Construction and Building Materials*, vol. 9, no. 2, pp. 91–95, 1995.

[45] W. Ashraf, "Carbonation of cement-based materials: challenges and opportunities," *Construction and Building Materials*, vol. 120, pp. 558–570, 2016.

[46] A. Leemann, P. Nygaard, J. Kaufmann, and R. Loser, "Relation between carbonation resistance, mix design and exposure of mortar and concrete," *Cement and Concrete Composites*, vol. 62, pp. 33–43, 2015.

[47] Y. Chen, P. Liu, and Z. Yu, "Effects of environmental factors on concrete carbonation depth and compressive strength," *Materials*, vol. 11, no. 11, p. 2167, 2018.

[48] K. K. Sideris, A. E. Savva, and J. Papayianni, "Sulfate resistance and carbonation of plain and blended cements," *Cement and Concrete Composites*, vol. 28, no. 1, pp. 47–56, 2006.

[49] J. Peng, H. Tang, J. Zhang, and S. C. S. Cai, "Numerical simulation on carbonation depth of concrete structures considering time- and temperature-dependent carbonation process," *Advances in Materials Science and Engineering*, vol. 2018, p. 1, 2018.

[50] H.-C. Cho, H. Ju, J.-Y. Oh, K. J. Lee, K. W. Hahm, and K. S. Kim, "Estimation of concrete carbonation depth considering multiple influencing factors on the deterioration of durability for reinforced concrete structures," *Advances in Materials Science and Engineering*, vol. 2016, pp. 1–12, Article ID 4814609, 2016.

[51] Y.-Y. Kim, K.-M. Lee, J.-W. Bang, and S.-J. Kwon, "Effect of *w/c* ratio on durability and porosity in cement mortar with constant cement amount," *Advances in Materials Science and Engineering*, vol. 2014, p. 1, 2014.

[52] S. Boualleg, M. Bencheikh, L. Belagraa, A. Daoudi, and M. A. Chikouche, "The combined effect of the initial cure and the type of cement on the natural carbonation, the portlandite content, and nonevaporable water in blended cement," *Advances in Materials Science and Engineering*, vol. 2017, pp. 1–17, Article ID 5634713, 2017.

[53] J. M. Chi, R. Huang, and C. C. Yang, "Effects of carbonation on mechanical properties and durability of concrete using accelerated testing method," *Journal of Marine Science and Technology*, vol. 10, pp. 14–20, 2002.

[54] B. L. D. S. Costa, J. C. D. O. Freitas, P. H. S. Santos, D. M. D. A. Melo, R. G. D. S. Araujo, and Y. H. D. Oliveira, "Carbonation in oil well Portland cement: influence of hydration time prior to contact with CO2," *Construction and Building Materials*, vol. 159, pp. 252–260, 2018.

[55] J. Liu, S. Yao, M. Ba, Z. He, and Y. Li, "Effects of carbonation on micro structures of hardened cement paste," *Journal of Wuhan University of Technology-Material Science Eduacation*, vol. 31, no. 1, pp. 146–150, 2016.

[56] M. Criado, A. Palomo, and A. Fernandezjimenez, "Alkali activation of fly ashes. Part 1: effect of curing conditions on the carbonation of the reaction products," *Fuel*, vol. 84, no. 16, pp. 2048–2054, 2005.

[57] L. Czarnecki and P. Woyciechowski, "Prediction of the reinforced concrete structure durability under the risk of carbonation and chloride aggression," *Bulletin of the Polish Academy of Sciences: Technical Sciences*, vol. 61, no. 1, pp. 173–181, 2013.

[58] B. Dong, Q. Qiu, J. Xiang, C. Huang, F. Xing, and N. Han, "Study on the carbonation behavior of cement mortar by electrochemical impedance spectroscopy," *Materials*, vol. 7, no. 1, pp. 218–231, 2014.

[59] L. S. Ho, K. Nakarai, Y. Ogawa, T. Sasaki, and M. Morioka, "Strength development of cement-treated soils: effects of water content, carbonation, and pozzolanic reaction under drying curing condition," *Construction and Building Materials*, vol. 134, pp. 703–712, 2017.

[60] H. Yang, L. Jiang, Y. Zhang, Q. Pu, and Y. Xu, "Predicting the calcium leaching behavior of cement pastes in aggressive environments," *Construction and Building Materials*, vol. 29, pp. 88–96, 2012.

[61] A. V. Saetta, B. A. Schrefler, and R. V. Vitaliani, "The carbonation of concrete and the mechanism of moisture, heat and carbon dioxide flow through porous materials," *Cement and Concrete Research*, vol. 23, no. 4, pp. 761–772, 1993.

[62] Q. Pu, L. Jiang, J. Xu, H. Chu, Y. Xu, and Y. Zhang, "Evolution of pH and chemical composition of pore solution in carbonated concrete," *Construction and Building Materials*, vol. 28, no. 1, pp. 519–524, 2012.

[63] K. Abid, R. Gholami, P. Choate, and B. H. Nagaratnam, "A review on cement degradation under CO 2-rich environment of sequestration projects," *Journal of Natural Gas Science and Engineering*, vol. 27, pp. 1149–1157, 2015.

Hindawi
Journal of Chemistry
Volume 2020, Article ID 6154152, 13 pages
https://doi.org/10.1155/2020/6154152

Research Article

Numerical Investigation of the Pressure Drop Characteristics of Isothermal Ice Slurry Flow under Variable Ice Particle Diameter

Shehnaz Akhtar[1], **Taqi Ahmad Cheema**[2], **Haider Ali**[3], **Moon Kyu Kwak**[1], **and Cheol Woo Park**[1]

[1]*School of Mechanical Engineering, Kyungpook National University, 80 Daehakro Bukgu, Daegu 41566, Republic of Korea*
[2]*Department of Mechanical Engineering, GIK Institute of Engineering Sciences and Technology, Topi 23460, Pakistan*
[3]*Department of Chemical Engineering, Norwegian University of Science and Technology, Trondheim, NO-7491, Norway*

Correspondence should be addressed to Cheol Woo Park; chwoopark@knu.ac.kr

Received 26 June 2020; Revised 26 October 2020; Accepted 28 October 2020; Published 11 November 2020

Academic Editor: Carlos Alves

Ice slurry is an advanced secondary refrigerant that has been attracting considerable attention for the past decade due to the growing concerns regarding energy shortage and environmental protection. To stimulate the potential applications of ice slurry, the corresponding pressure drop of this refrigerant must be comprehensively investigated. The flow of ice slurry is a complex phenomenon that is affected by various parameters, including flow velocity, ice particle size, and ice mass fraction. To predict the pressure drop of ice slurry flow in pipes, a mixture computational fluid dynamic model was adopted to simulate a two-phase flow without considering ice melting. The numerical calculations were performed on a wide range of six ice particle sizes (0.1, 0.3, 0.5, 0.75, 1, and 1.2 mm) and ice mass fraction ranging within 5%–20% in the laminar range of ice slurry flow. The numerical model was validated using experimental data. Results showed that the ice volumetric loading and flow velocity have a direct effect on pressure drop; it increases with the increase in volumetric concentration and flow velocity. The findings also confirmed that for constant ice mass fraction and flow velocity, the pressure drop is directly and inversely related to the particle and pipe diameters, respectively. Moreover, the rise in pressure drop is more significant for large ice particle diameter in comparison to smaller size ice particles at high values of ice concentration and flow velocity.

1. Introduction

The acceleration of global warming exerts a significant effect on environmental sustainability and is directly linked with increased greenhouse gas emissions and power consumption [1]. The building sector, which is one of the main energy consumption sectors, accounts for approximately 40% of the total energy consumption and carbon dioxide emission. A large portion of this percentage can be attributed to heating, ventilation, air conditioning, and refrigeration (HVAC and R) systems, which are designed for human comfort [2, 3]. Therefore, the development of sustainable and environmental friendly materials is crucial to improve the energy efficiency of HVAC and R systems [4]. Phase change materials (PCMs) are potential substitutes for such systems due to their enhanced energy transport density and cold energy storage medium [5–7].

Ice slurry, a type of PCM, is a mixture of ice particles dispersed in aqueous solution. This material is considered as an environmental friendly secondary refrigerant [8, 9]. The size of ice particles ranges from 1 mm to 1.2 mm in diameter, so it can be pumped through pipes or stored in tanks [10]. Owing to the combined effect of latent and sensible heats, ice slurry possesses high energy density, excellent heat transfer capabilities, and fast cooling rates [11, 12]. Consequently, this refrigerant has become a promising alternative to the traditional single-phase fluid used in cold energy storages and cold chains.

However, the implementation of ice slurry in engineering applications is not as straightforward as anticipated

because of the numerous complexities involved [13, 14]. One of the main problems is transporting the ice slurry in the cooling network to fulfil the cold requirements. Ice concentration and particle size are the critical parameters that significantly affect the ability to transport ice slurry through piping without particle aggregation, pipe plugging, and large pressure drop. If the values of above mentioned parameters are optimised, ice slurry can be transported as a single-phase flow (i.e., without any complication) in a wide range of conditions.

The pressure drop in the two-phase flow of ice slurry is an important consideration in engineering applications that has been extensively studied by many researchers [15–18]. For ice slurry flow in pipes, the pressure drop initially increases up to 10% due to flow velocity and ice mass fraction and eventually increases because of the ice mass fraction [19]. Bel et al. [20] obtained the same inference and stated that the frictional pressure drop for narrow tubes increases with the increase in ice concentration and the rate of augmentation is high in the low Reynolds number (Re) range [20]. Pressure drop increases due to the increase in flow velocity and ice concentration [18, 21–23], and the sensitivity of such drop to the variation in both factors is strongly influenced by the flow regime [24]. On the contrary, Knodal et al. [17] and Lieu et al. [25] reported that the pressure drop in low velocity regions decreased with the increase in ice concentration.

Related experiments rarely provided comprehensive information on the velocity distribution, ice concentration distribution, and particle size of ice slurry in pipes due to technical difficulties. Given the advancement in the numerical techniques and the complexity involved in experimental setups, computational fluid dynamics (CFD) emerge as an excellent tool for obtaining extensive knowledge on two-phase flows, particularly ice slurry flow and accurate pressure drop estimation in pipes. Some researchers developed numerical modelling approaches to simulate ice slurry flow in pipes [26–29].

Wang et al. [30] adopted the Eulerian–Eulerian model to evaluate the pressure drop of an isothermal ice slurry flow under various pipe configurations (e.g., vertical, horizontal, and elbow pipes). The results confirmed that the pressure drop in all configuration increases with ice concentration and flow velocity. Similarly, Tian et al. [31] investigated the effect of ice concentration, pipe, and ice particle size on safe transportation of ice slurry by using the Eulerian–Eulerian multiphase model. The findings revealed that the safe transportation of ice slurry in cooling systems can be achieved at an ice concentration of up to 20% and ice particle size of 100 μm [31].

Niezgoda-Zelasko and Zalewski [32] combined the mixture multiphase and Eulerian–Eulerian models to investigate the pressure drop in the laminar flow range of a horizontal pipe with a pipe diameter of 16 mm. The Eulerian–Eulerian model underestimates the pressure drop, whereas the former provides a reasonably correct description of the pressure drop with respect to experimental results. The maximum percentage error of the numerical predictions obtained through the mixture multiphase model of pressure drop is approximately 15% of the experimental results [33].

Within the available literature, however, there is not much work that addresses the application of a numerical model to describe the ice slurry flow [18]. Therefore, if ice slurry is categorized as solid-liquid flow, the mixture multiphase CFD model is appropriate [34]. It is reported that the mixture method has been extensively applied to ice slurry horizontal slurry pipe flows and to water and kerosene mixtures, which have density ratio nearly identical to ice slurry for a wide range of particle sizes (ranging from 0.1 mm to 2 mm) [32, 35–38]. The mixture model is recommended for multiphase flow with small differences in density between the phases [34]. Given that the particle relaxation time is short, the mixture model formulation can also be successfully applied to the two-phase flow with a significant density difference [39].

Zhang and Shi [7] used the Eulerian–Eulerian model to investigate the isothermal ice slurry flow under various ice particle diameters (0.1 mm and 0.27 mm). However, they only considered the ice particle velocity and solid particle distribution and disregarded the particle-dependent pressure drop characteristics. Moreover, they did not investigate the ice particle size-dependent flow characteristics of ice slurry in different pipe diameters. Clarifying the influence of ice particle diameter on pressure drop and flow structure is important, especially for choosing a suitable ice generation technique.

On the basis of the discussion above, the studies on the particle size-dependent pressure drop characteristics are lacking. Moreover, previous studies only considered limited particle sizes and disregarded the particle-based pressure drop characteristics of ice slurry flow. To demonstrate the effect of ice particle diameter on pressure drop, the present study aims to analyse the pressure drop estimation of isothermal ice slurry flow based on pipe diameter and particle size using an aqueous solution of 10.3% ethanol in horizontal pipes with diameters of 9 mm and 23 mm. To the best of the authors' knowledge, no previous study has investigated the particle size-dependent flow characteristics of isothermal ice slurry within such dimeter range. The mixture CFD model is applied to describe the pressure drop characteristics of isothermal ice slurry flow without considering ice melting. Simulations are performed considering the laminar range of the ice slurry flow for six different particle diameters (0.1-1.2 mm). The ice mass fraction for each particle diameter ranges within 5%–20%.

2. Problem Description

This study aims to investigate the pressure drop and flow characteristics of isothermal ice slurry flowing through horizontal pipes with diameters of 9 mm and 23 mm by using a mixture multiphase model. Ice slurry is a mixture of ice and aqueous solution of the carrier liquid (10.3% ethanol–water). Simulations were performed for six different particle diameters (0.1-1.2 mm) in the laminar regime. An ice mass fraction of 5%–20% was set for each particle diameter. The effects of various parameters, including flow

velocity, ice mass fraction, and ice particle diameter, on the pressure drop characteristics of the isothermal ice slurry were analysed using numerical calculations. The mathematical modelling and property calculation correlations for ice slurry are discussed in the following subsections.

2.1. Mathematical Modelling. The mixture multiphase model is adopted to simulate the isothermal ice slurry flow. This model is a simplified model that utilises mixture properties to capture the two-phase flows, in which the liquid and solid phases move at different velocities but assume local equilibrium over short spatial length scales. An algebraic slip formulation is used to describe the relative velocity between the liquid and solid phases, and the numerical solution is reduced to a set of equations for the mixture phase, which comprises continuity, momentum, and particle volume fraction equations for the secondary phase. Given the small number of equations involved in the mixture model, the stability and convergence of the numerical solution are encouraging which greatly reduces the computational efforts. The fundamental governing equations for the mixture model are given below. The continuity equation for the mixture multiphase model is expressed as

$$\frac{\partial}{\partial t}(\rho_m) + \nabla \cdot (\rho_m \vec{u}_m) = 0, \tag{1}$$

where ρ_m denotes the density of mixture, and u represents the local velocity. The momentum equation for the mixture model is written as

$$\begin{aligned}\frac{\partial}{\partial t}(\rho_m \vec{u}_m) + \nabla \cdot (\rho_m \vec{u}_m \vec{u}_m) &= -\nabla p + \nabla \cdot \left[\mu_m\left(\nabla \vec{u}_m + \nabla \vec{u}_m{}^T\right)\right] + \rho_m \vec{g} + \nabla \\ &\cdot \left(\sum_{i=1}^{2} \alpha_i \rho_i \vec{u}_{Di} \vec{u}_{Di}\right),\end{aligned} \tag{2}$$

where subscript i denotes the phase i ($i = (1(l)/2(s))$ represents the liquid phase and solid phase, respectively), μ_m represents mixture viscosity, α is the ice volume fraction, and u_{Di} is the drift velocity defined as the ith phase velocity relative to the mixture phase. The drift velocity is defined by the relationship proposed by Taivassalo and Kallio [34].

$$\begin{aligned}\vec{u}_{Ds} &= \vec{u}_s - \vec{u}_m = \vec{u}_{ls} - \sum_{i=1}^{2} \frac{\alpha_i \rho_i}{\rho_m} \vec{u}_{li}, \\ \vec{u}_{Dl} &= \vec{u}_l - \vec{u}_m = -\vec{u}_{ls} - \sum_{i=1}^{2} \frac{\alpha_i \rho_i}{\rho_m} \vec{u}_{si},\end{aligned} \tag{3}$$

where u_{ls} is the slip velocity, which is defined using an algebraic slip formulation introduced by Schiller [40].

$$\vec{u}_{ls} = \vec{u}_l - \vec{u}_s = \frac{(\rho_m - \rho_s) {d_s}^2}{18 \mu_l f_{\text{drag}}} \left(\vec{g} - \frac{\partial \vec{u_m}}{\partial t}\right). \tag{4}$$

The drag function proposed by Schiller [40] is expressed as

$$f_{\text{drag}} = \begin{cases} 1 + 0.15 \text{Re}_s^{0.687}, & \text{Re}_s \le 1000, \\ 0.018 \text{Re}_s, & \text{Re}_s \ge 1000, \end{cases} \tag{5}$$

where d_s denotes the particle diameter, and Re_s represents the Re of the particle.

$$\text{Re}_s = \frac{\rho_l |u_s - u_l|}{\mu_l} \tag{6}$$

The viscosity and mixture density in the mixture multiphase model are respectively defined as

$$\begin{aligned}\mu_m &= \sum_{i=1}^{2} \alpha_i \mu_i, \\ \rho_m &= \sum_{i=1}^{2} \alpha_i \rho_i.\end{aligned} \tag{7}$$

From the continuity equation, the volume fraction equation for dispersed phase is expressed as

$$\frac{\partial}{\partial t}(\alpha_s \rho_s) + \nabla \cdot (\alpha_s \rho_s \vec{u}_m) = -\nabla \cdot (\alpha_s \rho_s \vec{u}_{Ds}). \tag{8}$$

The boundary conditions for the inlet, outlet, and pipe walls in mixture and dispersed phases are as follows: (1) uniform velocity is applied to the pipe inlet in the mixture phase, and ice volume fraction is adopted for the dispersed phase, (2) atmospheric boundary condition is adopted for the outlet in mixture and dispersed phases, and (3) a no-slip boundary condition is applied to the pipe wall in mixture and dispersed phases. The influence of temperature change on the flow is excluded due to the isothermal conditions (Figure 1).

2.2. Physical Properties of the Ice Slurry. The corelations for the determination of the physical properties of the ice slurry are obtained from the handbook of ice slurry [41].

$$\rho_m = \alpha_s \rho_s + (1 - \alpha_s) \rho_l, \tag{9}$$

$$\mu_m = \mu_l\left(1 + 2.5\alpha_s + 10.05\alpha_s^2 + 0.00273 e^{16.6\alpha_s}\right), \tag{10}$$

where α_s and α_ρ, respectively, denote the ice volume fraction and density of the ice particles, ρ_l and ρ_m are the densities of the carrier liquid, and μ_m and μ_l represent the viscosity of the ice slurry and carrier liquid (10.3% ethanol–water solution), respectively. Table 1 presents the physical properties of the carrier liquid and ice particles calculated at a phase equilibrium temperature of 268.65 K.

3. Numerical Details

The commercial CFD software ANSYS Fluent (version 13) was used to investigate the pressure drop of the isothermal ice slurry in a horizontal pipe with diameters of 9 mm and 23 mm. The pipe length was set according to the relation $L \ge 100$ D to attain the fully developed flow. Variable density-based meshes were generated using the ICEM software; meshes near the wall are finer than the far ones. A mesh

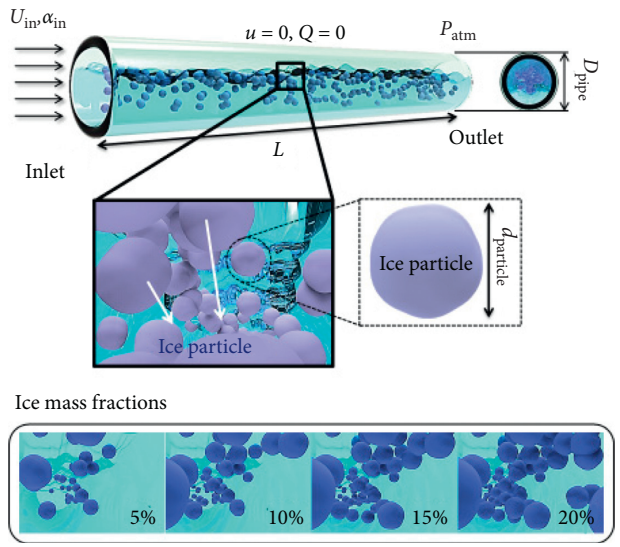

Figure 1: Schematic of the pipe flow with relevant boundary conditions.

Table 1: Physical properties of ice slurry [45].

	Properties	Expression	Value
Aqueous solution (10.3%)	Density	$\rho_l = 987.44108 - 2.45747 \times e^{(T-273.15/24.21577)}$	987 kg/m^3
	Viscosity	$\mu_l = 0.70354 + 3.3244 \times e^{-(T-273.15/16.63572)}$	5.032×10^{-3} Pa. s
Ice particles	Density	$\rho_s = 917 - 0.13 \times (T - 273.15)$	917 kg/m^3

independence study was performed to validate the high precision of the results using minimum computational resources by considering three different levels of mesh refinement and varying these levels by a factor of three (total number of elements for $D = 23$ mm: $G1 = 67{,}155$, $G2 = 188{,}889$, and $G3 = 284{,}138$; for $D = 9$ mm: $G1 = 109{,}020$, $G2 = 301{,}500$, and $G3 = 603{,}980$). The marginal difference in the numerical calculations of the pressure drop was evident for all grid sizes. Therefore, grid size $G2$ was adopted in the subsequent simulations to save computation time (Figures 2 and 3).

All governing equations were discretised using the finite volume approach, where the second-order upwind and SIMPLEC schemes were used for convective diffusive terms and pressure velocity coupling, respectively. The convergence requirement for all variables was fixed to 10^{-4}.

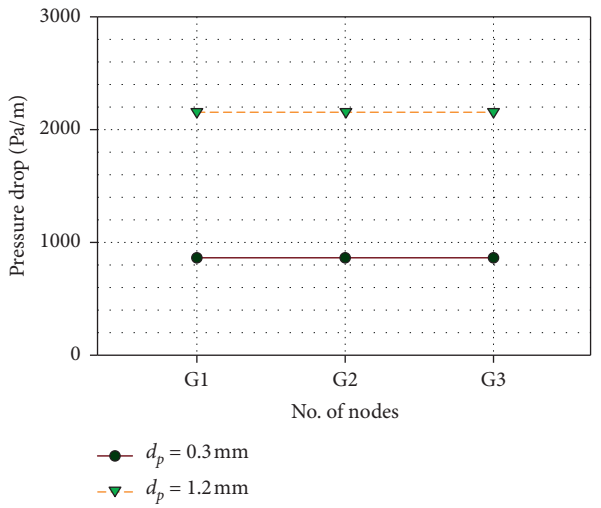

Figure 2: Grid sensitivity test at a pipe diameter of 9 mm, ice mass fraction of 10%, and flow velocity of 0.4306 m/s.

4. Results and Discussion

To confirm the accuracy of the mixture CFD model, the numerical results are compared with the experimental results obtained by Grozdek et al. [21]. The validation is conducted under a wide range of flow velocities and ice mass fractions. The validation is conducted over laminar range of ice slurry flow $\mathrm{Re} \leq = 2190$. For a two-phase flow of ice slurry, the flow pattern transition from laminar to turbulent can be observed within the range of Reynolds number from 2000 to 2300 depending upon the pipe diameter and ice mass fraction [21, 32]. It should be noted that for constant flow velocity and pipe diameter, the Reynolds number decreases as the ice mass fraction increases. Since viscosity increases and mixture density decreases with the increase in ice mass fraction. The flow behaviour was evaluated on the basis of Reynolds number given by

$$Re_m = \frac{\rho_m U D}{\mu_m}, \tag{11}$$

where Re_m is the Reynolds number of mixture, and the mixture density is ρ_m, and the mixture viscosity μ_m was calculated from equations (9) and (10).

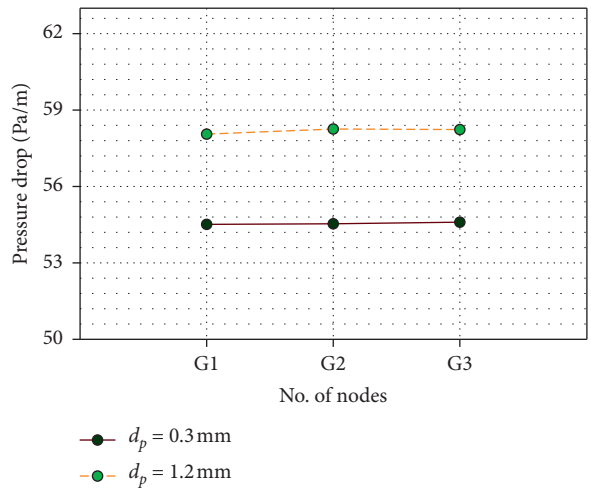

Figure 3: Grid sensitivity test at a pipe diameter of 23 mm, ice mass fraction of 10%, and flow velocity of 0.16851 m/s.

A pipe diameter of 9 mm is considered to match the experimental conditions in the study of Grozdek et al. [21]. As shown in Figures 4(a)–4(c), the mixture CFD model provides a reasonable estimation of the pressure drop of isothermal ice slurry flow. All numerical predictions by the CFD model are in close agreement with the experimental data, and the relative errors for all considered cases are restricted to 15%. However, at high ice mass fraction of 10% and specifically 15%, the general concavity of the graph is different than those of at ice mass fraction of 5%. This could be well explained by the phenomenon of laminarization. The high concentration of ice delays the transition from laminar to turbulent flow. As the concentration of ice rises, the critical number of Reynolds where transition happens also increases and can reach even higher values than $Re_c = 2300$. These results are consistent with the other findings [32, 42].

4.1. Pressure Drop. The pressure drop for ice slurry flow is an important characteristic because it reflects the pumping power requirement. In this section, the influence of ice particle diameter on the pressure drop characteristics of the isothermal ice slurry flowing through a horizontal pipe with diameters of 9 mm and 23 mm is discussed. The results have been discussed in the laminar range of flow for both pipes evaluated on the basis of bulk Reynold number. The maximum Reynolds number is 1798 and 1998 for pipe diameter 23 mm and 9 mm, respectively.

The results are presented in terms of pressure gradient as a function of variable ice particle size for a wide range of flow velocity and ice mass fraction. For a given ice concentration, the pressure drop per unit length increases with the increase in ice particle diameter for all flow velocities (Figure 4). However, at a fixed ice concentration, the increase in pressure drop is high for large ice particle diameters at high flow velocity. For low velocities (velocities approximately below 0.3592 m/s), the effect of ice particle diameter on the pressure drop is small.

For small particle diameters (0.1–0.3 mm), the rise in the pressure drop at low velocities is marginal. As the ice particle size increases from 0.3 mm to 1.2 mm, the effect of particle diameter on pressure drop becomes increasingly pronounced (Figures 5(a)–5(d)). For instance, at fixed ice mass fraction (5%) and flow velocity (0.1796 m/s), the percentage increase in pressure drop as the particle diameter increases from 0.1 mm to 0.3 mm is 10% (Figure 5(a)). When the particle diameter is 1.2 mm, the percentage increase in pressure drop is 37%, which is approximately 3.5% of the original value. For the same ice concentration and flow velocity of 0.5389 m/s, the percentage increase in pressure drop when the particle diameter increases from 0.1 mm to 0.3 mm is 13%; the increment when the particle diameter is 1.2 mm is approximately 76%, which is almost 5.5% of the pressure drop at 0.1 mm. Large ice particle size leads to a larger drag force which causes larger relative velocity of ice particles. Because of this, larger lift force will act on the ice particle which will increase its flotation tendency. Consequently, the heterogeneity of ice particles distribution will increase with the increase in the size of the particle, thereby resulting in additional frictional losses. Furthermore, the effect of ice particle reinforcement becomes increasingly evident when the particle diameter is large [30].

At a fixed velocity, the pressure drop of slurry with high volume fraction is large. For instance, at a constant velocity of 0.1796 m/s, the pressure drop increases by an average of 2%, 3%, and 4% for each additional 5% of ice concentration as the particle size increases from 0.1 mm to 1.2 mm; the increment at an ice concentration of 5% is 1% (Figures 5(a)–5(d)). The reason for this phenomenon is that the addition of more ice particles, i.e., increasing ice mass fraction, results in an increased viscosity of ice slurry, which alters the density of the mixture as well as the number of Reynolds (results in decrease of the number of Reynolds, which leads to the accumulation of ice particles in the walls, and raises the potential of ice blockage, which increases resistance to flow) [15, 43]. This affects the safe transport of ice slurry in pipes at high ice concentrations.

The pressure drop per unit length is illustrated as a function of ice particle diameter (pipe diameter = 23 mm) in Figures 6(a)–6(d). Figure 6 demonstrates that the pressure

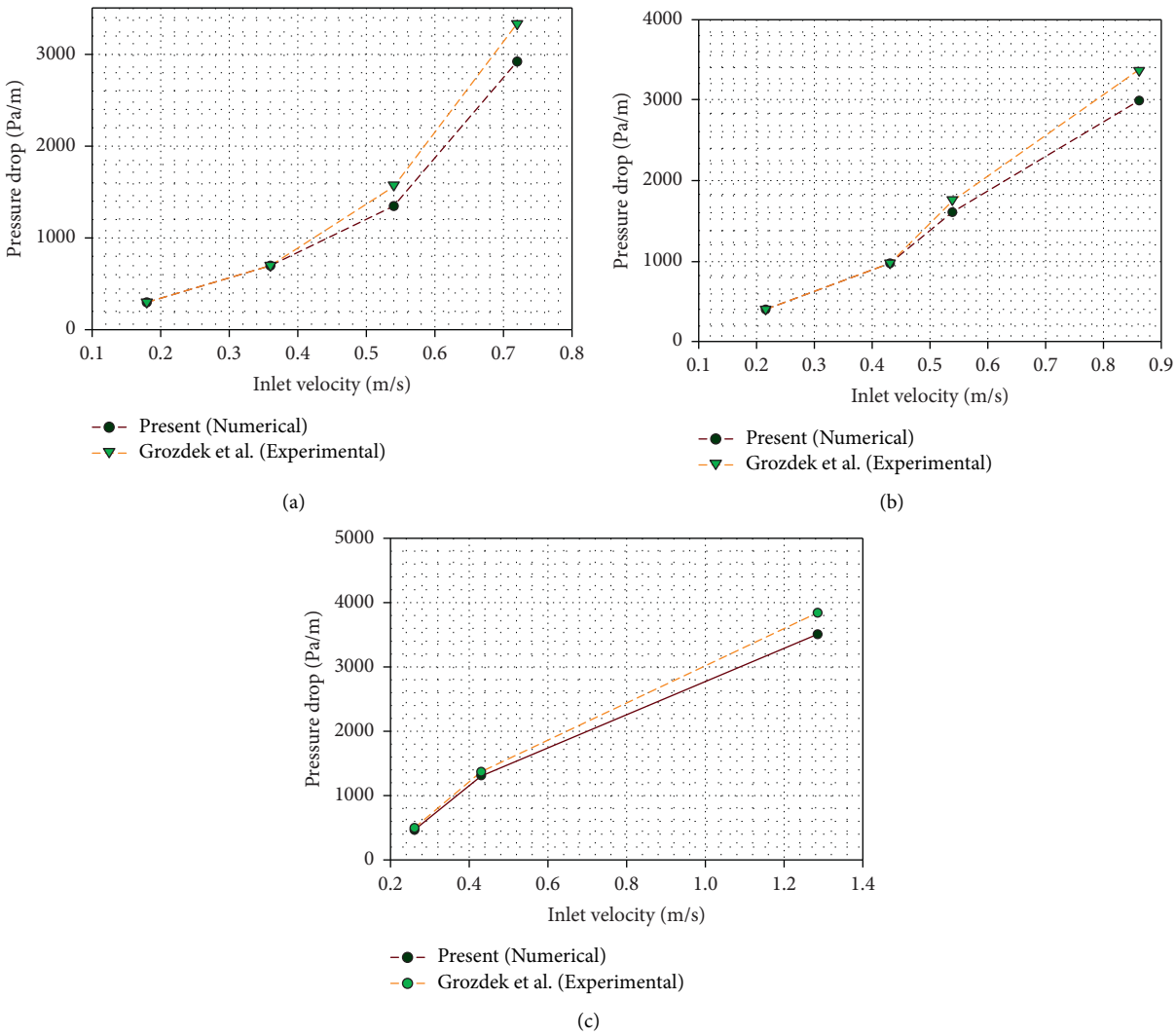

Figure 4: Comparison of the obtained results with the experimental results of Grozdek et al. (pipe diameter = 9 mm) at constant ice mass fractions of (a) 5%, (b) 10%, and (c) 15%.

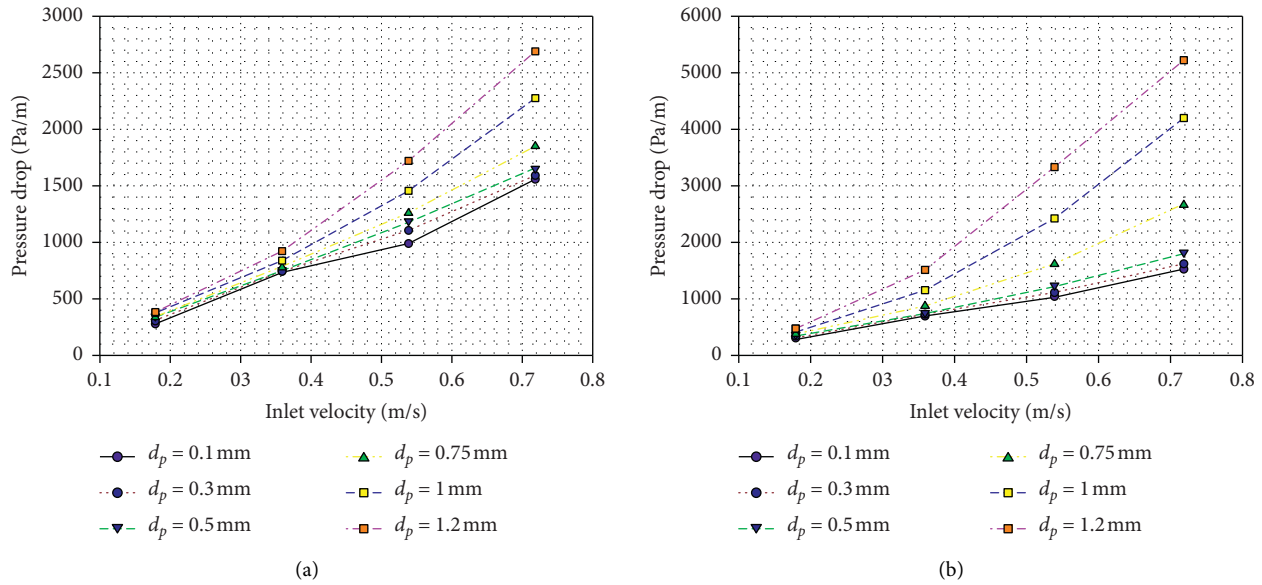

Figure 5: Continued.

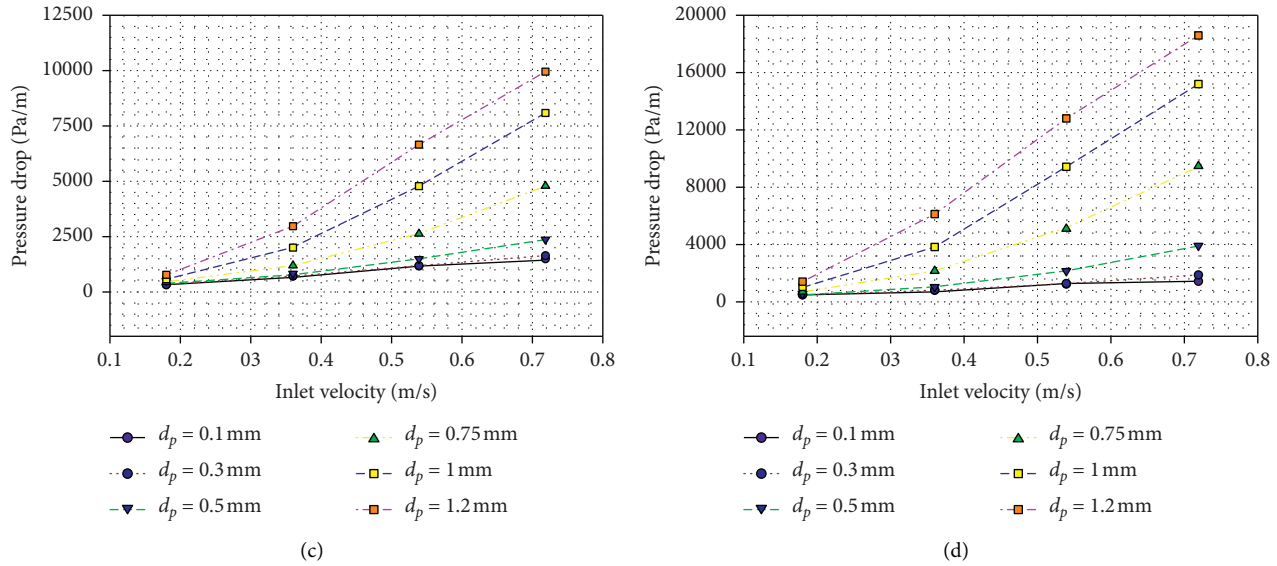

Figure 5: Variation of pressure drop per unit length as a function of ice particle diameter at a pipe diameter of 9 mm and ice mass fractions of (a) 5%, (b) 10%, (c) 15%, and (d) 20%.

gradient increases with the increase in ice particle size. However, the pressure drop at a pipe diameter of 23 mm is lower than that at smaller ones. For a given velocity, the pressure drop increases with the decreases in pipe diameter and vice versa. Liu et al. [44] concluded that the ice particles in pipes with large diameters provide a coherent structure to the fluid and reduce the amount of energy dissipated by the viscous frictions. On the basis of the results, the pressure drop associated with ice slurry pipe flow is a function of particle size. Ice slurry with large particle size that flows through pipes with small diameters yields unwanted increments in pressure drop and maximises the pumping power penalties.

4.2. Velocity Contours. Figures 7–9 show the contours of the velocity distribution of the solid phase at the perpendicular cross-section in the outlet of the 9 mm pipe. The contours correspond to varying inlet velocities (0.1796, 0.3592, and 0.5389 m/s) at different ice particle diameters (0.1, 0.75, and 1.2 mm) and constant ice mass fraction of 10%.

The velocity contours indicate that the local velocity along the pipe wall is minimal and almost stagnant because viscous forces are dominating the vicinity of the wall. Moreover, when the ice slurry flows in the low velocity region with high ice concentration, the ice particles cluster together at the walls, and the value of the velocity increases towards the centre of the pipe. The Figures 7–9 depict that given a constant inlet velocity, the local velocity value increases with the increase in ice particle size towards the centre of the pipe. In addition, the velocity distribution becomes increasingly homogeneous as the inlet velocity increases when the volume fraction of ice is constant [43]. Furthermore, no difference is observed in the velocity distribution between the solid and liquid phases of all cases.

4.3. Velocity and Concentration Profile. One way to assess the flow patterns of ice slurry flow is to examine the velocity distribution in the cross-section of the flow. The influence of ice particle diameter on the mixture velocity distribution profiles in the vertical diameter direction along the horizontal cross-section of the pipe outlet is illustrated in Figures 10 and 11. The mixture velocity distributions of three different particle diameters (0.1, 0.75, and 1.2 mm) at ice mass fractions of 5% and 10% are plotted under different inlet velocities (pipe diameter = 9 mm).

Figures 10 and 11 show mixture velocity profile distribution in the cross-section of the flow at distance $L = 0.5$ (mid-length) and at the outlet cross-section of the pipe. It has been observed that at around 0.5 m distance from the entrance of the pipe, the velocity profile is still developing. However, after this length, the ice slurry flow is fully developed, and the velocity profile is parabolic in nature. Hence, the entrance length is around 0.5 m for the present case, and the ice slurry flow is fully developed after this distance (data after $L = 0.5$ m showed the fully developed flow and are not included to avoid complexity). The velocity fields for all particle size subjected to the present study are symmetrical with respect to the vertical diameter, and the extremes values of velocity occur on the centre of diameter.

Similarly, the ice concentration distribution along the vertical diameter for pipe diameter = 9 mm at constant ice mass fraction of 10%, for different inlet velocities, and ice particle diameter of 0.1 mm, 0.75 mm, and 1.2 mm are presented in Figure 12. It is clear from the figure that for constant ice volume fraction, heterogeneity of ice slurry flow increases with the increase in ice particle diameter and flow velocity. The larger particles exert larger drag force, which in turn results in the larger relative velocity and increases the heterogeneity of ice particles.

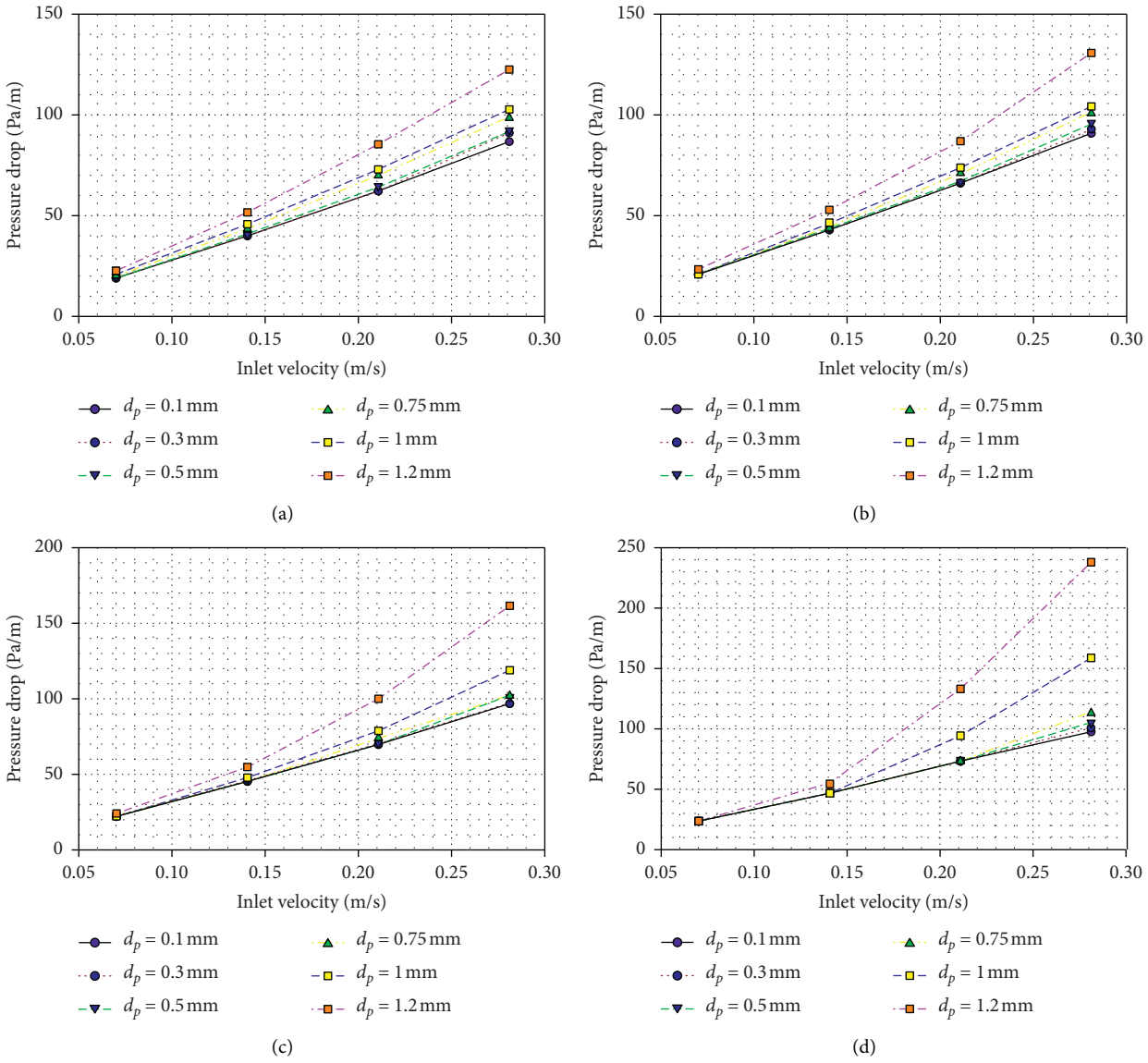

Figure 6: Variation of pressure drop per unit length as a function of ice particle diameter at a pipe diameter of 23 mm and ice mass fractions of (a) 5%, (b) 10%, (c) 15%, and (d) 20%.

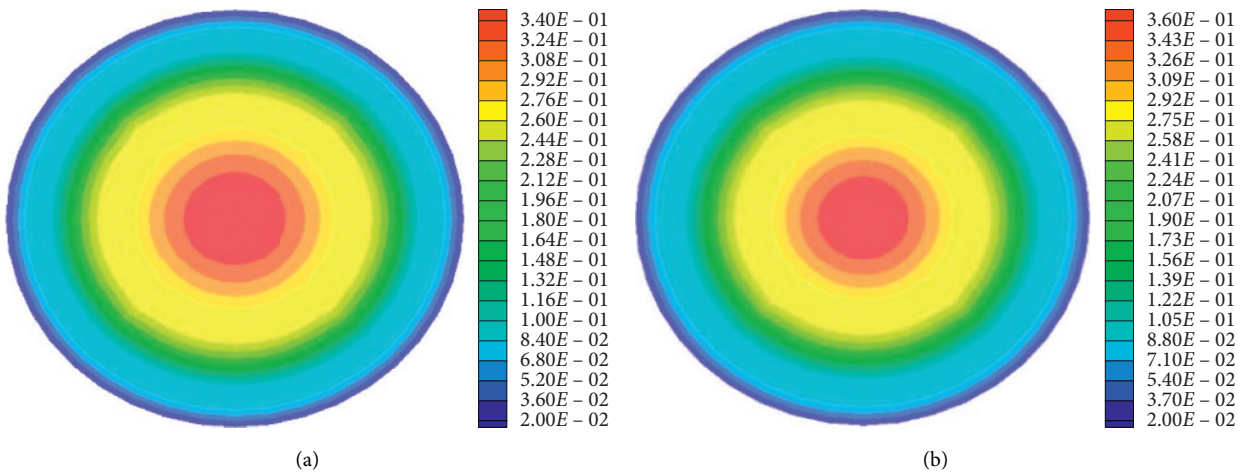

Figure 7: Continued.

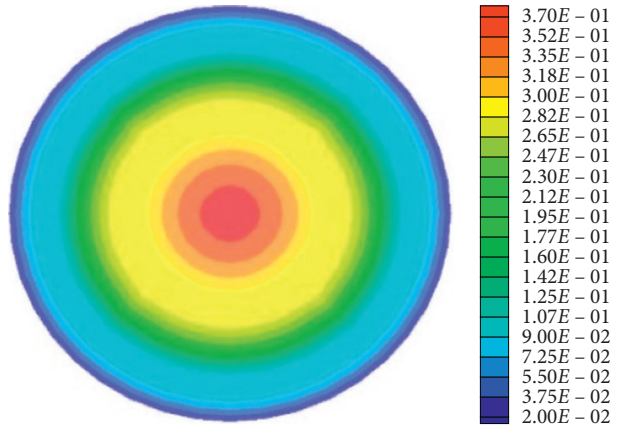

(c)

Figure 7: Contours of the solid velocity profile at a constant flow velocity of 0.1796 m/s and ice mass fraction of 10% at different ice particle diameters (dp): (a) 0.1, (b) 0.75, and (c) 1.2 mm.

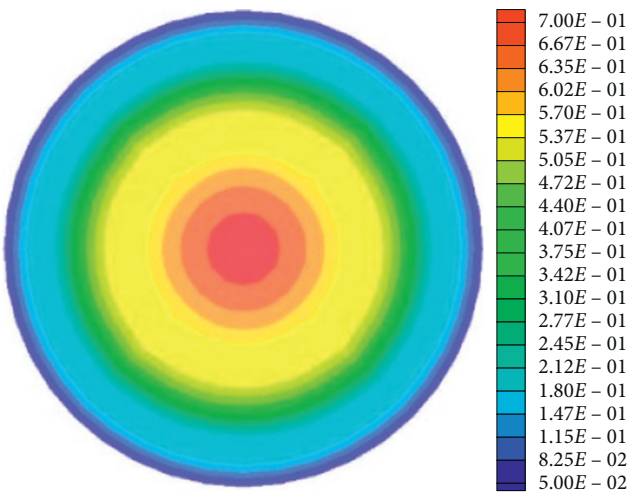

(a)

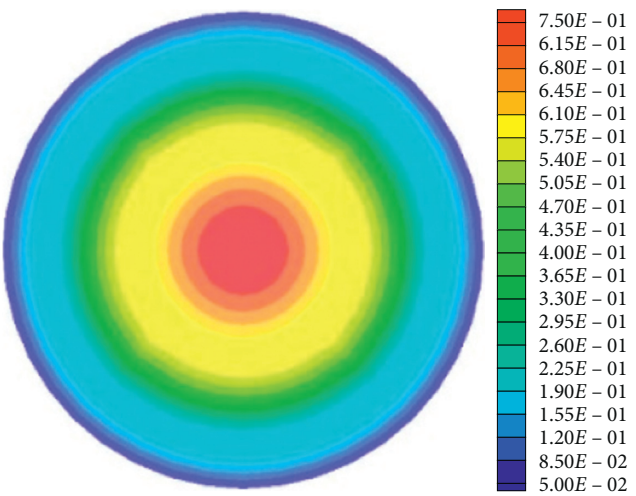

(b)

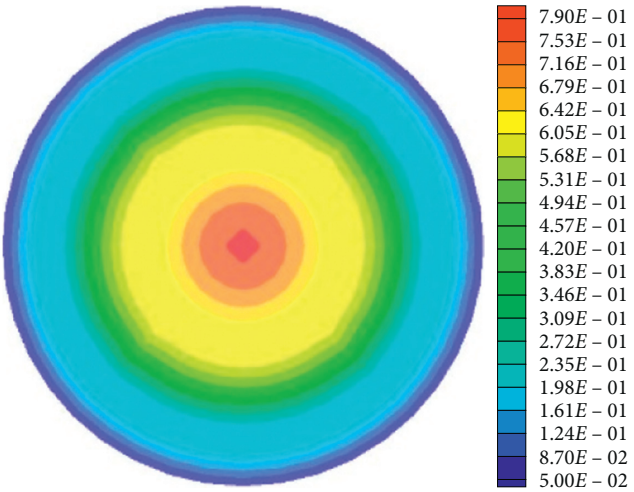

(c)

Figure 8: Contours of the solid velocity profile at a constant flow velocity of 0.3592 m/s and ice mass fraction of 10% at different dp: (a) 0.1, (b) 0.75, and (c) 1.2 mm.

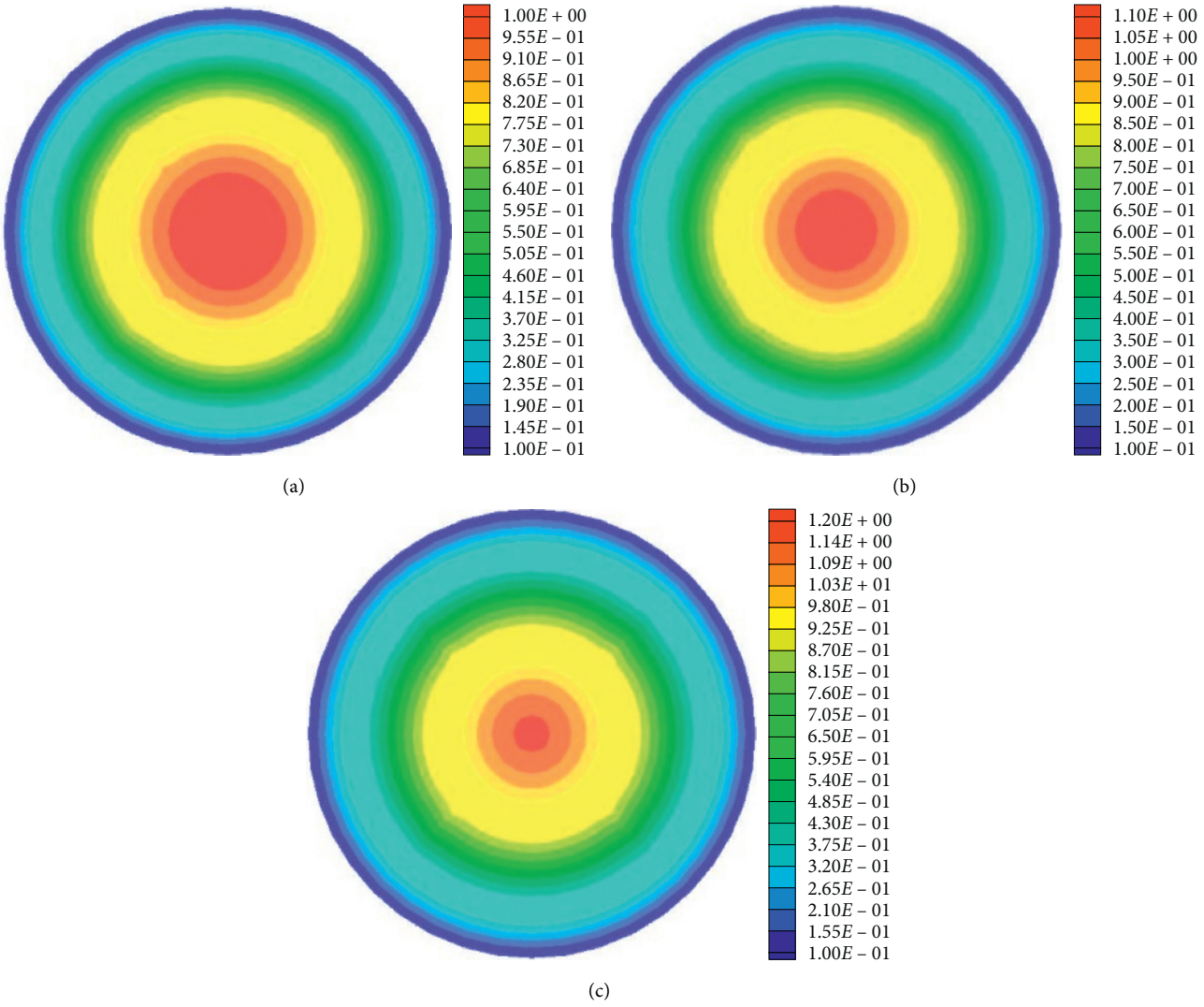

Figure 9: Contours of the solid velocity profile at a constant flow velocity of 0.5389 m/s and ice mass fraction of 10% at different dp: (a) 0.1, (b) 0.75, and (c) 1.2 mm.

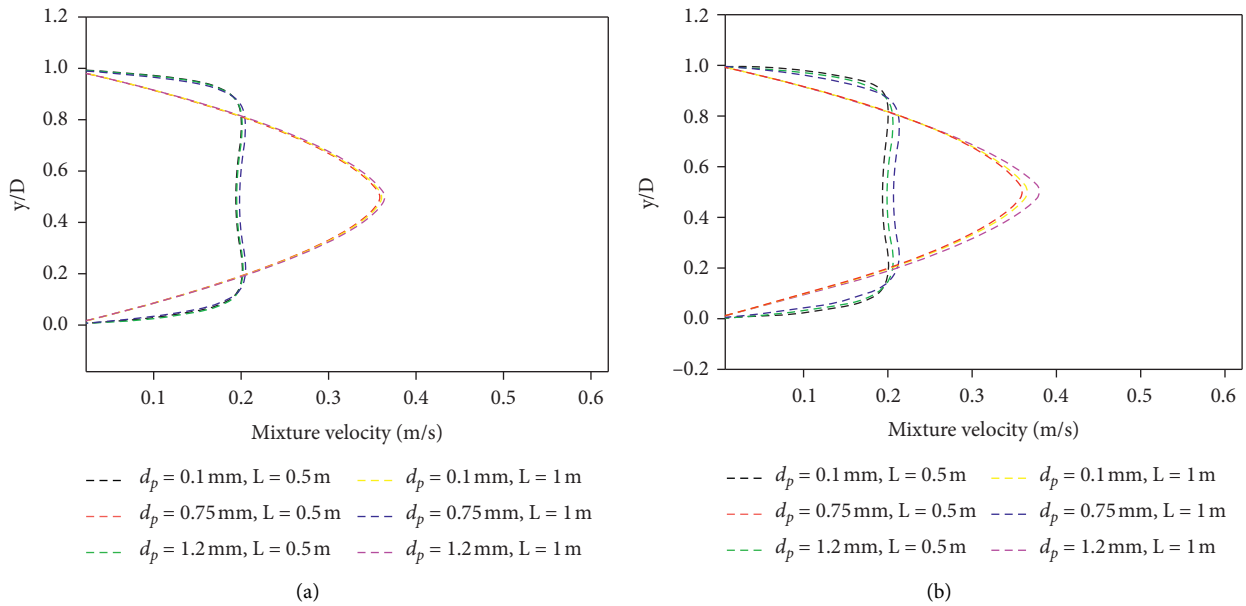

Figure 10: Effect of ice particle size on the ice slurry velocity profile at $D = 9$ mm, $V = 0.1796$ m/s, and (a) $\alpha = 5\%$ and (b) $\alpha = 10\%$.

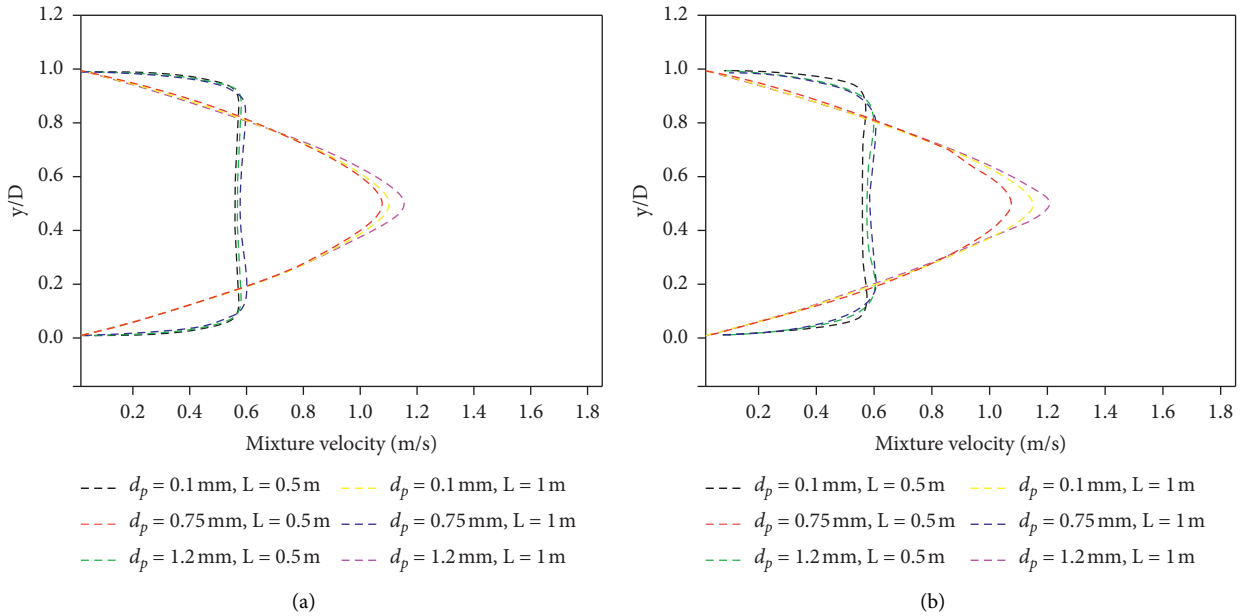

Figure 11: Effect of ice particle size on the ice slurry velocity profile at $D = 9$ mm, $V = 0.5389$ m/s, and (a) $\alpha = 5\%$ and (b) $\alpha = 10\%$.

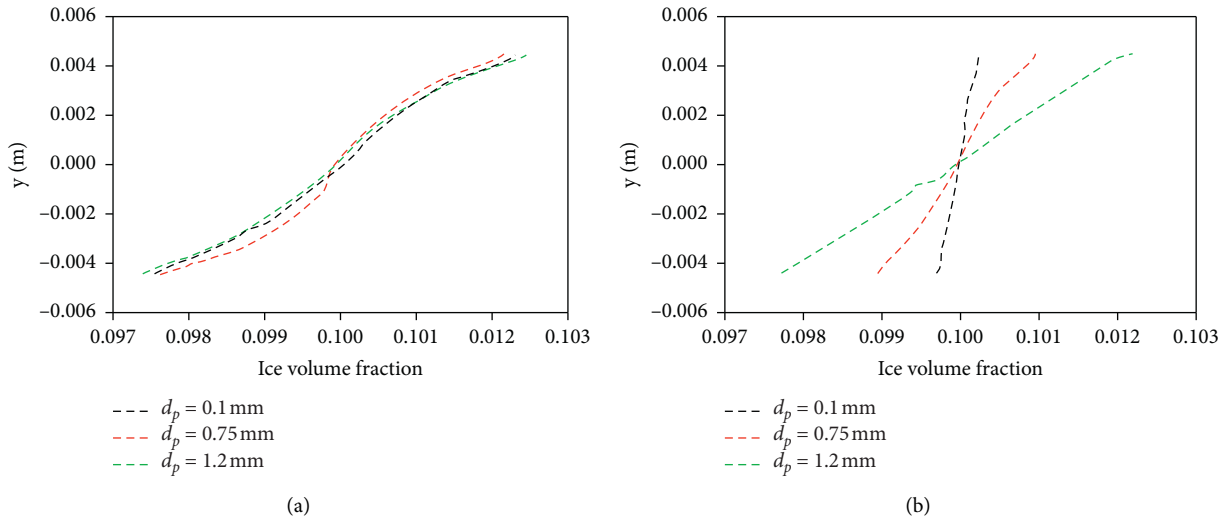

Figure 12: Effect of ice particle size on ice volume fraction distribution at $D = 9$ mm, $\alpha = 10\%$, and (a) $V = 0.1796$ m/s and (b) $V = 0.5389$ m/s.

5. Conclusion

The study presented the CFD modelling of the two-phase flow of isothermal ice slurry through horizontal pipes with diameters of 9 mm and 23 mm within the laminar range. The pressure drop characteristics are evaluated under six ice particle sizes (0.1, 0.3, 0.5, 0.75, 1, and 1.2 mm) at an ice mass fraction range of 5%–20%. The results of the present study are validated by the experimental findings. The pressure drop predictions are in excellent agreement with the experimental results obtained by Grozdek et al. [21] for a wide range of inlet velocity and ice mass fraction under the laminar regime. The following conclusions are derived from the numerical calculations.

(i) The pressure drop per unit length significantly increases with the increase in ice mass fraction and flow velocity, and the pressure loss rapidly rises at high ice concentration and flow velocity.

(ii) Pressure drop per unit length increases with the increase in ice particle size and decreases with the increase in pipe diameter.

(iii) The increase in the pressure drop per unit length of ice particles with large diameters at high flow velocity and ice concentration is significant. The rate of increase for the particle with a diameter of 1.2 mm is approximately 3–5 times higher than that of the particle with a diameter of 0.1 mm as the flow

velocity increases from 0.1796 m/s to 0.5381 m/s. Moreover, the pressure drop increases by an average of 2%, 3%, and 4% for every 5% increment in ice concentration; the corresponding drop is only 1% when the ice concentration is 5%.

(iv) The local velocity near the pipe wall is minimal and almost stagnant due to the dominance of the viscous forces near the wall region. This value, however, increases towards the centre of the pipe.

Results suggest that pipes with small diameters are not recommended to transport ice slurry because of their higher pressure drop than those with large diameters. In addition, given that a large particle size results in undesirable increments in pressure drop, the size of the ice particle must be kept small to reduce the pumping power penalties. In the future, the effect of ice particle size on the performance of ice slurry should be explored using various performance evaluation criteria.

Nomenclature

L: Pipe length, m
Re: Reynolds number
d_p, d_s: Particle diameter, m
D: Pipe diameter, m
U, V: Inlet velocity, m/s
g: Gravitational acceleration, m/s^2
T: Temperature, K
f_D: Drag force
uD_i: Drift velocity, m/s
u_{ls}: Slip velocity, m/s
i: Phase index
p: Pressure, Pa

Greek symbols

μ: Viscosity, Pa·s
ρ: Density, kg/m^3
α: Volume fraction

Subscripts

l: Liquid phase, aqueous solution
s: Solid phase, ice particles
m: Mixture, ice slurry
sl, ls: Interaction between the solid and liquid phases
p: Particle.

Data Availability

The data used to support the findings of this study are included within the article.

Conflicts of Interest

The authors declare that they have no conflicts of interest.

Acknowledgments

This study was supported by the National Research Foundation of Korea and funded by the Korean government (MSIP, 2020R1A2B5B02002512 and 2020R1A4A1018652).

References

[1] P. Nejat, F. Jomehzadeh, M. M. Taheri, M. Gohari, and M. Z. Abd. Majid, "A global review of energy consumption, CO 2 emissions and policy in the residential sector (with an overview of the top ten CO 2 emitting countries)," *Renewable and Sustainable Energy Reviews*, vol. 43, pp. 843–862, 2015.

[2] C. Amaral, R. Vicente, P. A. A. P. Marques, and A. Barros-Timmons, "Phase change materials and carbon nanostructures for thermal energy storage: a literature review," *Renewable and Sustainable Energy Reviews*, vol. 79, pp. 1212–1228, 2017.

[3] L. Pérez-Lombard, J. Ortiz, and C. Pout, "A review on buildings energy consumption information," *Energy and Buildings*, vol. 40, no. 3, pp. 394–398, 2008.

[4] N. Soares, J. Bastos, L. D. Pereira et al., "A review on current advances in the energy and environmental performance of buildings towards a more sustainable built environment," *Renewable and Sustainable Energy Reviews*, vol. 77, pp. 845–860, 2017.

[5] P. Zhang and Z. W. Ma, "An overview of fundamental studies and applications of phase change material slurries to secondary loop refrigeration and air conditioning systems," *Renewable and Sustainable Energy Reviews*, vol. 16, no. 7, pp. 5021–5058, 2012.

[6] N. A. C. Sidik, T. H. Kean, H. K. Chow, A. Rajaandra, S. Rahman, and J. Kaur, "Performance enhancement of cold thermal energy storage system using nanofluid phase change materials: a review," *International Communications in Heat and Mass Transfer*, vol. 94, pp. 85–95, 2018.

[7] P. Zhang and X. J. Shi, "Thermo-fluidic characteristics of ice slurry in horizontal circular pipes," *International Journal of Heat and Mass Transfer*, vol. 89, pp. 950–963, 2015.

[8] J. Bellas, I. Chaer, and S. A. Tassou, "Heat transfer and pressure drop of ice slurries in plate heat exchangers," *Applied Thermal Engineering*, vol. 22, no. 7, pp. 721–732, 2002.

[9] K. Kasza, U. Choi, and J. Kaminsky, "Reducing the high costs of district heating and cooling," *English For Specific Purposes Journal*, vol. 56, no. 4, pp. 39–42, 1986.

[10] P. W. Egolf and M. Kauffeld, "From physical properties of ice slurries to industrial ice slurry applications," *International Journal of Refrigeration*, vol. 28, no. 1, pp. 4–12, 2005.

[11] M. Kauffeld, M. J. Wang, V. Goldstein, and K. E. Kasza, "Ice slurry applications," *International Journal of Refrigeration*, vol. 33, no. 8, pp. 1491–1505, 2010.

[12] T. W. Davies, "Slurry ice as a heat transfer fluid with a large number of application domains," *International Journal of Refrigeration*, vol. 28, no. 1, pp. 108–114, 2005.

[13] F. Illán and A. Viedma, "Experimental study on pressure drop and heat transfer in pipelines for brine based ice slurry. Part I: operational parameters correlations," *International Journal of Refrigeration*, vol. 32, no. 5, pp. 1015–1023, 2009.

[14] F. Illán and A. Viedma, "Experimental study on pressure drop and heat transfer in pipelines for brine based ice slurry Part II: dimensional analysis and rheological model," *International Journal of Refrigeration*, vol. 32, no. 5, pp. 1024–1031, 2009.

[15] D. W. Lee, C. I. Yoon, E. S. Yoon, and M. C. Joo, "Experimental study on flow and pressure drop of ice slurry for various pipes," in *Proceedings of the 5th Workshop on Ice-Slurries of the International Institute of Refrigeration*, Stockholm, Sweden, May 2002.

[16] B. Niezgoda-Zelasko and J. Zelasko, "Generalized non-Newtonian flow of ice-slurry," *Chemical Engineering and Processing: Process Intensification*, vol. 46, no. 10, pp. 895–904, 2007.

[17] B. D. Knodel, D. M. France, U. S. Choi, and M. W. Wambsganss, "Heat transfer and pressure drop in ice-water slurries," *Applied Thermal Engineering*, vol. 20, no. 7, pp. 671–685, 2000.

[18] A. C. S. Monteiro and P. K. Bansal, "Pressure drop characteristics and rheological modeling of ice slurry flow in pipes," *International Journal of Refrigeration*, vol. 33, no. 8, pp. 1523–1532, 2010.

[19] E. N. Jensen, K. G. Christensen, T. M. Hansen, P. Schneider, and M. Kauffeld, "Pressure drop and heat transfer with ice slurry," *Science and Technology du froid*, pp. 572–580, 2001.

[20] O. Bel, *Contribution à l'étude du comportement thermo-hydraulique d'un mélange diphasique dans une boucle frigorifique à stockage d'énergie*, INSA, Lyon, France, 1996.

[21] M. Grozdek, R. Khodabandeh, and P. Lundqvist, "Experimental investigation of ice slurry flow pressure drop in horizontal tubes," *Experimental Thermal and Fluid Science*, vol. 33, no. 2, pp. 357–370, 2009.

[22] M. Kauffeld, K. G. Christensen, S. Lund, and T. M. Hansen, "Experience with ice slurry," in *Proceedings of the 1st workshop on Ice Slurries*, Yverdon-les-Bains, Switzerland, June 1999.

[23] C. Hägg, "*Ice Slurry as Secondary Fluid in Refrigeration Systems. School of Industrial Engineering and Management*," Royal Institute of Technology (KTH) Licentiate Thesis, Stockholm, Sweden, 2005.

[24] J. Wang, S. Wang, T. Zhang, and F. Battaglia, "Mathematical and experimental investigation on pressure drop of heterogeneous ice slurry flow in horizontal pipes," *International Journal of Heat and Mass Transfer*, vol. 108, pp. 2381–2392, 2017.

[25] Y. H. Liu, E. Z. Zhang, J. M. Zhao, and P. L. Chen, "Experiment study on friction loss characteristics of pipes with ice slurry," *Science and Technology du froid*, pp. 490–494, 1997.

[26] S. Mi, L. Cai, K. Ma, and Z. Liu, "Investigation on flow and heat transfer characteristics of ice slurry without additives in a plate heat exchanger," *International Journal of Heat and Mass Transfer*, vol. 127, pp. 11–20, Dec. 2018.

[27] L. Onokoko, M. Poirier, N. Galanis, and S. Poncet, "Experimental and numerical investigation of isothermal ice slurry flow," *International Journal of Thermal Sciences*, vol. 126, pp. 82–95, 2018.

[28] D. Xu, Z. Liu, L. Cai, Y. Tang, Y. Yu, and A. Xu, "A CFD-PBM approach for modeling ice slurry flow in horizontal pipes," *Chemical Engineering Science*, vol. 176, pp. 546–559, 2018.

[29] S. Akhtar, H. Ali, and C. W. Park, "Thermo-Fluidic characteristics of two-phase ice slurry flows based on comparative numerical methods," *Processes*, vol. 7, no. 12, p. 898, 2019.

[30] J. Wang, S. Wang, T. Zhang, and Y. Liang, "Numerical investigation of ice slurry isothermal flow in various pipes," *International Journal of Refrigeration*, vol. 36, no. 1, pp. 70–80, 2013.

[31] Q. Tian, G. He, H. Wang, and D. Cai, "Simulation on transportation safety of ice slurry in ice cooling system of buildings," *Energy and Buildings*, vol. 72, pp. 262–270, 2014.

[32] B. Niezgoda-Zelasko and W. Zalewski, "Momentum transfer of ice slurry flows in tubes, modeling," *International Journal of Refrigeration*, vol. 29, no. 3, pp. 429–436, 2006.

[33] J. Wang, T. Zhang, and S. Wang, "Heterogeneous ice slurry flow and concentration distribution in horizontal pipes," *International Journal of Heat and Fluid Flow*, vol. 44, pp. 425–434, 2013.

[34] V. Taivassalo and S. Kallio, "On the mixture model for multiphase flow," *VTT Publications*, vol. 288, pp. 3–67, 1996.

[35] C. X. Lin and M. A. Ebadian, "A numerical study of developing slurry flow in the entrance region of a horizontal pipe," *Computers & Fluids*, vol. 37, no. 8, pp. 965–974, 2008.

[36] D. Gidaspow, *Multiphase Flow and Fluidization: Continuum and Kinetic Theory Descriptions*, Academic Press, Cambridge, MA, USA, 1994.

[37] Ł. Mika, "Ice slurry flow in a poppet-type flow control valve," *Experimental Thermal and Fluid Science*, vol. 45, pp. 128–135, 2013.

[38] H. M. El-Batsh, M. A. Doheim, and A. F. Hassan, "On the application of mixture model for two-phase flow induced corrosion in a complex pipeline configuration," *Applied Mathematical Modelling*, vol. 36, no. 11, pp. 5686–5699, 2012.

[39] G. He, Y. Yamazaki, and A. Abudula, "A droplet size dependent multiphase mixture model for two phase flow in PEMFCs," *Journal of Power Sources*, vol. 194, no. 1, pp. 190–198, 2009.

[40] L. Schiller, "A drag coefficient correlation," *Zeit. Ver. Deutsch. Ing.*vol. 77, pp. 318–320, 1933.

[41] P. W. Egolf, M. Kauffeld, and M. Kawaij, "Handbook on ice slurries-fundamentals and engineering," *International Institute of Refrigeration*, pp. 259–263, 2005.

[42] M. Kauffeld, M. Kawaji, and P. W. Egolf, "Handbook on ice slurries," *International Institute of Refrigeration Paris*, vol. 359, 2005.

[43] K. S. Rawat and A. K. Pratihar, "Numerical investigation of ice slurry flow in a horizontal pipe," *IOP Conference Series: Materials Science and Engineering*, vol. 310, no. 1, 2018.

[44] K. V Liu, U. S. Choi, and K. E. Kasza, "Measurements of pressure drop and heat transfer in turbulent pipe flows of particulate slurries," *NASA STI/Recon Tech. Rep. N*, vol. 89, 1988.

[45] Å. Melinder, "Properties and other aspects of aqueous solutions used for single phase and ice slurry applications," *International Journal of Refrigeration*, vol. 33, no. 8, pp. 1506–1512, 2010.

Hindawi
Journal of Chemistry
Volume 2020, Article ID 6062128, 9 pages
https://doi.org/10.1155/2020/6062128

Research Article

Study on Synergies of Fly Ash with Multiwall Carbon Nanotubes in Manufacturing Fire Retardant Epoxy Nanocomposite

Tuan Anh Nguyen and Quang Tung Nguyen

Faculty of Chemical Technology, Hanoi University of Industry, No. 298 Cau Dien, North District Tu Liem, Hanoi, Vietnam

Correspondence should be addressed to Tuan Anh Nguyen; anhnt@haui.edu.vn

Received 25 March 2020; Revised 27 June 2020; Accepted 18 July 2020; Published 8 August 2020

Guest Editor: Carlos Alves

In this study, fly ash (FA) and multiwalled carbon nanotubes (MWCNTs) were used to make environmentally friendly nanocomposites, which have high fire retardant properties and high mechanical properties. Industrial waste such as fly ash has become a major concern during the treatment of environmental pollution. MWCNTs were used in this experiment to enhance the flame retardant properties and mechanical properties of materials with fly ash additives. MWCNTs content (0.03, 0.04, and 0.05 wt.%) and fly ash content (30, 40, and 50 wt.%) were studied for three different levels. The flame retardancy of the material is significantly improved by the addition of fly ash/MWCNTs at different rates, especially at 0.04 wt. % MWCNTs and 40 wt. % fly ash with LOI at 26.8%. Regarding mechanical properties, tensile strength increases as fly ash/MWCNTs increase, up to a critical point. On the other hand, the compressive strength of composite increases continuously as fly ash/MWCNTs increase. Scanning electron microscopy (SEM) was used to observe the morphology of fly ash and MWCNTs as well as its distribution in the matrix. This will help analyze the influence of the effectiveness of the combination of fly ash and MWCNTs to the flame retardancy and mechanical properties of fly ash/MWCNTs/epoxy nanocomposites.

1. Introduction

Epoxy resins have high adhesion characteristics with many reinforcements, good chemical resistance and corrosion resistance, and superior electrical properties; they are widely used in various industrial fields such as coatings, bearing structures, adhesives, and composite materials. However, one of the main disadvantages of epoxy resin is its inherent flammability, which has limited its application in many areas because the safety is considered. So this is an important issue to improve flame retardant of epoxy resin.

Fly ash (FA) is an industrial solid waste produced by coal power plants. The disposal of fly ash waste by landfill at landfills has polluted the environment, which is a major concern about environmental pollution [1]. FA is one of the additives used in composites, making applications of materials in different fields. In recent times, fly ash has been studied by many scientists around the world as an additive for polymers. In order to expand the application of fly ash and diversify products [2], Sroka et al. studied the use of fly ash in the manufacture of thermal insulating materials [3]. Sroka et al. also studied fly ash denaturation by [3- (2-aminoethylamino) propyl] trimethoxysilane. The results show that the mechanical properties have been significantly improved compared to the unmodified fly ash. The work has demonstrated the use of modified fly ash as an additive to make epoxy composite materials that can be applied in the field of civil electricity [4]. Research on the effect of fly ash on the mechanical properties of epoxy composites shows that increasing the mass of fly ash results in reduced tensile strength and increased flexural and compressive strength [5]. In particular, the recent studies published by scientists are about the use of fly ash in manufacturing materials with high fire resistance and, at the same time, the mechanical properties remain stable; the content of fly ash used for the study was 5, 10, and 20 wt.% [6]. V. C. Divya and his colleagues have conducted research on making composite materials based on polyethylene based plastic using fly ash

and MWCNTs. The results showed that with 0.2 wt. % MWCNTs, 20 wt. % fly ash gave the best fire resistance [7]. M. Soyama et al. also studied the flame retardant properties of polycarbonate composites with 25 wt.% resulting in samples with a high flame retardant [8]. Sim et al. [9] studied fly ash at levels of 10, 30, and 50 wt.%, showing that the compressive strength increases with increasing fly ash content. Several other studies are about the effects of aging on the mechanical properties of epoxy composites with 20 wt.% [10]. In addition, fly ash is also used to make epoxy composites with insulating properties, studied by Pham Thi Huong [11]. Fly ash is also used to make geopolymer; however, to improve some mechanical properties such as tensile strength and bending strength, some scientists have added nanoadditives such as MWCNTs to enhance some of the degraded durability in the desired green concrete production [12–14]. This is the study on flame retardant properties and mechanical properties of epoxy nanocomposites materials in the presence of fly ash additives and reinforced by MWCNTs. During the study of using fly ash additives to make composites, some mechanical strength was reduced, hence, this research sought to overcome the above limitation by adding nanoadditives, namely, MWCNTs.

(i) Curing agent: epoxy resin is converted into solid and insoluble three-dimensional networks by curing with cross-linkers. This study collected amine function curing agent diethylenetriamine of Dow Chemical Company to research. Diethylenetriamine: $H_2N(CH_2)_2NH(CH_2)_2NH_2$ (DETA), density 0.953 g/cm^3 at 20°C, boiling point 207°C, Mw: 103.2 gmol^{-1}, and epoxy curing reaction with DETA (see Figure 1).

(ii) HCl, NaOH of Dow Chemicals (USA).

(iii) Fly ash is supplied from Song Da 12- Cao Cuong Joint Stock Company (Vietnam). This is real; the product is extracted from waste ash and ash from Pha Lai Thermal Power Plant (Vietnam). It consists of a solid mixture and the spherical particles have different sizes (from 1 μm to 100 μm, average size: 28 μm).

(iv) Multiwall carbon nanotubes (MWCNTs) of Showa Denko (Japan) are synthesized by catalyst deposition method. MWCNTs have an average diameter of 40–45 nm, an average length of 3 μm, and a density of 0.08 g/cm^3.

2. Materials and Methods

2.1. Materials

(i) Epoxy Epikote 240 (EP) resin of Shell Chemicals (USA) (see Table 1)

2.2. Methods

2.2.1. Sample Preparation. The Fly ash was prepared according to Table 2. Fly ash (30, 40, and 50 wt%) and MWCNT (0.03, 0.04, and 0.05 wt%) were dispersed in epoxy Epikote 240 resin, stirred at 3000 rpm for 8 h (HS-100T, WiseStir, Korea). In order to break up the MWCNT bundles and disperse the additives, the ultrasonic vibration uses an ultrasonic bath (Elmasonic S300 H, 37 kHz, Germany) for 6 h, 65°C. After the mixtures were homogenously mixed, the curing agent DETA (amount of curing agent was calculated by epoxy content of epoxy resin and stirred for 15 min at 200 rpm/min) was added and the mixtures were moulded for curing. The mould was coated with a uniform thin film of silicone, a releasing agent for easy removal of cured specimen. The samples were cured at room temperature for about 24 h and further cured at 80°C in the laboratory oven for 3 h. Then, the samples were removed from the mould and, after 7 days, the mixture was analyzed and mechanical properties were measured.

2.2.2. Characterizations

(1) Mechanical Properties

(i) Tensile strength is determined according to ISO 527–1993 on INSTRON 5582–100 kN (United States) with a pulling speed of 5 mm/min, temperature of 25°C, and humidity of 75%.

(ii) Flexural strength is determined according to ISO 178–1993 standard on INSTRON 5582–100 kN (United States) with bending speed of 5 mm/min, temperature of 25°C, and of humidity 75%.

(iii) Compressive strength is determined according to ISO 604–1993 on INSTRON 5582–100 kN (United States), compression speed of 5 mm/min, and temperature of 25°C.

(iv) Izod impact resistance is determined according to ASTM D265 on Tinius Olsen (USA), measured at Polymer Materials Research Center, Hanoi University of Science & Technology (HUST).

(2) Flame Retardants Properties

(i) Limit oxygen index (LOI) according to ASTM D2863-12 and JIS K720 (Japan): the bars used for the test are $150 \times 6.5 \times 3$ mm^3.

(ii) Horizontal combustion tests (UL-94HB): the test piece of the standard bar must be 125 ± 5 mm long, 13.0 ± 0.5 mm wide, and supplied in minimum thickness and thickness of 3.0 $(-0.0 + 0.2)$ mm (ASTM D635-12).

(iii) Fire resistance: equipment, specially designed for fire and flame retardant of thermoplastic, thermosetting, hard, and thin laminates, designed and engineered to meet the following standards: ASTM D 757; specimen size of $3.17 \times 12.7 \times 121$ mm^3; and maximum temperature of 950°C, measured at Polymer Materials Research Center, Hanoi University of Science & Technology (HUST).

(3) Method of Determining the Structural Morphology of Materials

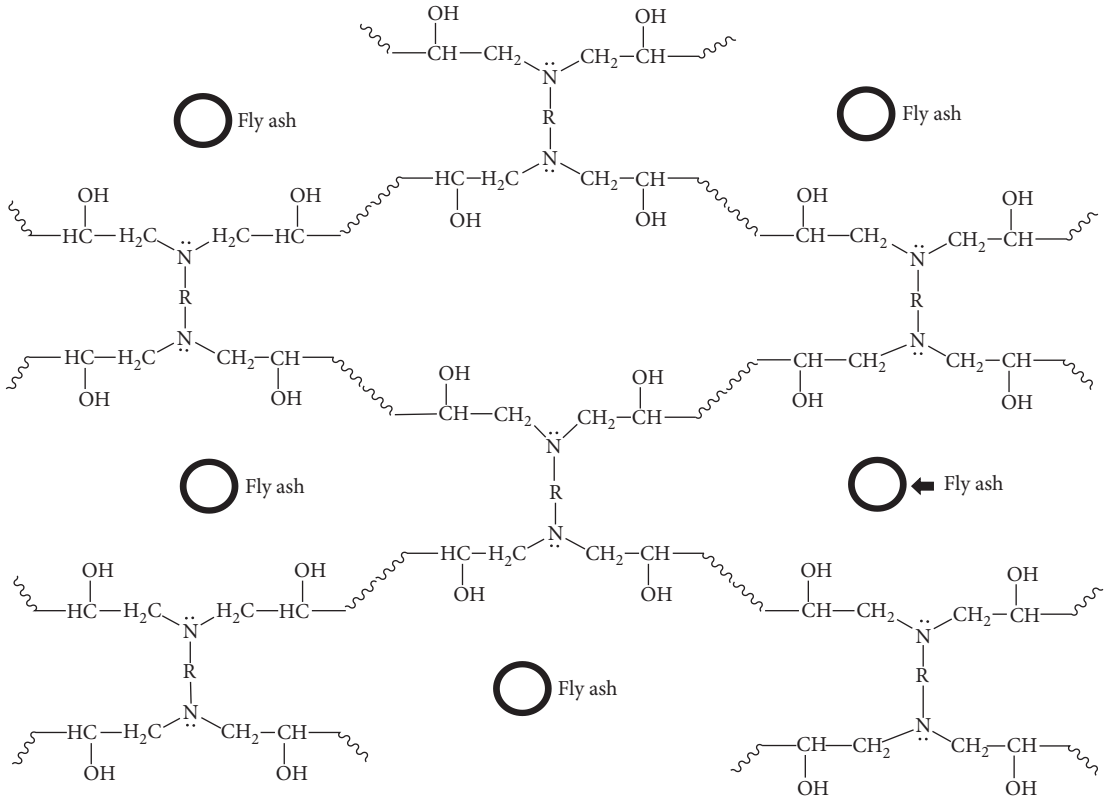

Figure 1: Images of fly ash particles alternating between epoxy molecules after plastic curing [15].

Table 1: Specification of epoxy Epikote 240 resin.

Property	Test method	Unit	Value
Epoxy group content	SMS 2026	mmol/kg	5100–5400
Epoxy molar mass*		g	185–196
Viscosity at 25°C	ASTM D445	Pa.s**	0.7–1.1
Colour	ASTM D1209	Pt-Co	200 max
Density at 25°C	ASTM D4052	kg/L	1.12

*Number of grams of resin containing 1g equivalent of epoxide (weight per equivalent, (WPE) is an alternative term). **1 Pa.s = 10 poise.

Table 2: Taguchi orthogonal array of designed experiments based on the coded levels.

Trial	Fly ash (wt%)	MWCNTs content (wt%)	Sample code
1	0	0.03	FA01
2	30	0	FA02
3	30	0.03	FAST1
4	40	0.03	FAST2
5	50	0.03	FAST3
6	30	0.04	FAST4
7	40	0.04	FAST5
8	50	0.04	FAST6
9	30	0.05	FAST7
10	40	0.05	FAST8
11	50	0.05	FAST9

(i) The morphology of the samples was carried out by scanning electron microscope (SEM, S4800-NIHE, 10.0 kV, Japan).

3. Results and Discussion

3.1. Morphology of Nanocomposites. The fractured surface morphology of epoxy and composites is shown in Figure 2, with 40 wt.%

Images show a separation between fly ash particles (orbs) and epoxy resin. This phenomenon shows a poor communication link between epoxy and fly ash.

Mechanical stirring method combined with ultrasonic vibration was selected to conduct mixing in the fabrication of samples. The degree distribution observed by SEM image is shown in Figure 3. Figure 3 shows the uniformly distributed fly ash particles and clearly shows good wetting and bonding well with epoxy substrates. The evidence is that after the material is broken, the fly ash particles are still retained on the broken surface and the epoxy resin surrounds the particle.

The structural morphology image (Figure 4(a)) shows that fly ash particles are strongly bonded with the epoxy resin. However, there are still small (small) gaps around the fly ash element.

On the other hand, from another perspective, when there is external force, a part of fly ash is broken (red arrow), but it has not been removed from the substrate (Figure 4(b)).

In that gas, MWCNTs are also distributed evenly (the position of the arrows), there is no phenomenon of clustering and agglomeration, showing the good compatibility of MWCNTs-fly ash-epoxy combination. From the results of SEM image, fly ash was dispersed quite well and wet well,

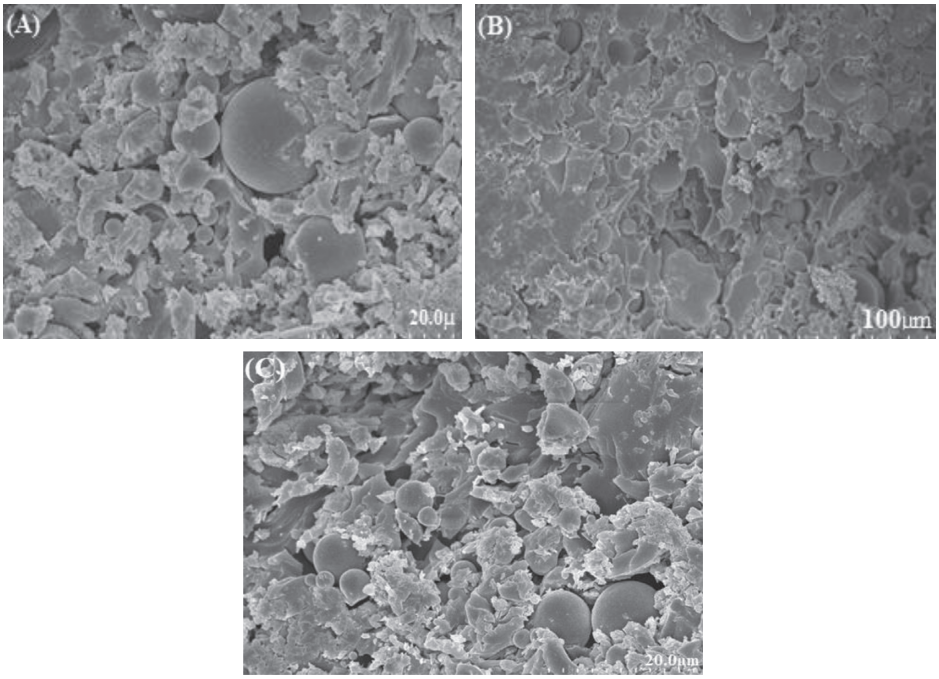

Figure 2: SEM image of epoxy composite material/fly ash: fly ash 40 wt.% ((a), (b)).

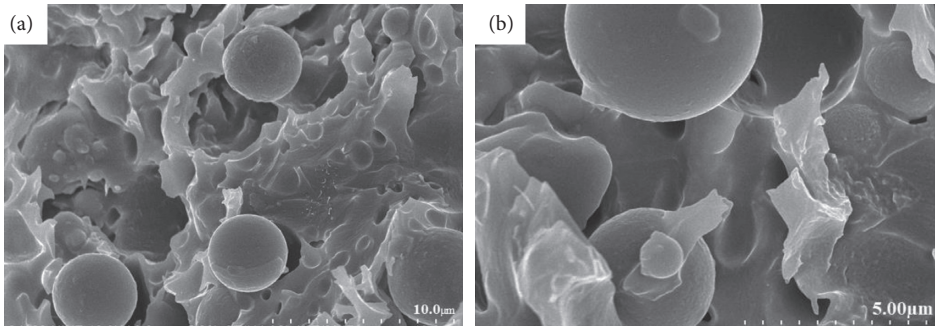

Figure 3: SEM images of nanocomposites: 30 wt.% fly ash/0.03 wt.% MWCNTs/epoxy ((a), (b)).

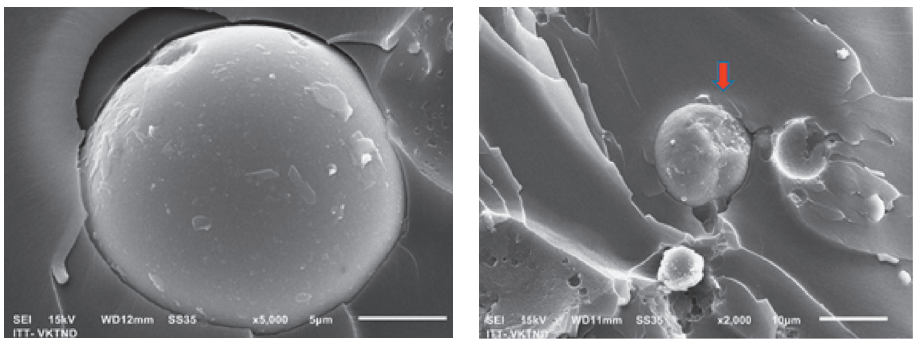

(a) (b)

Figure 4: SEM images of nanocomposites: 40 wt.% fly ash/0.04 wt.% MWCNTs/epoxy ((a), (b)).

there were no holes and fly ash particles adhered well to epoxy E 240, broken surface of smooth material (see Figure 5).

The scanning electron microscope was used to observe the dispersion/fracture morphology of the MWCNT/epoxy resin/fly ash composites with higher resolution. SEM

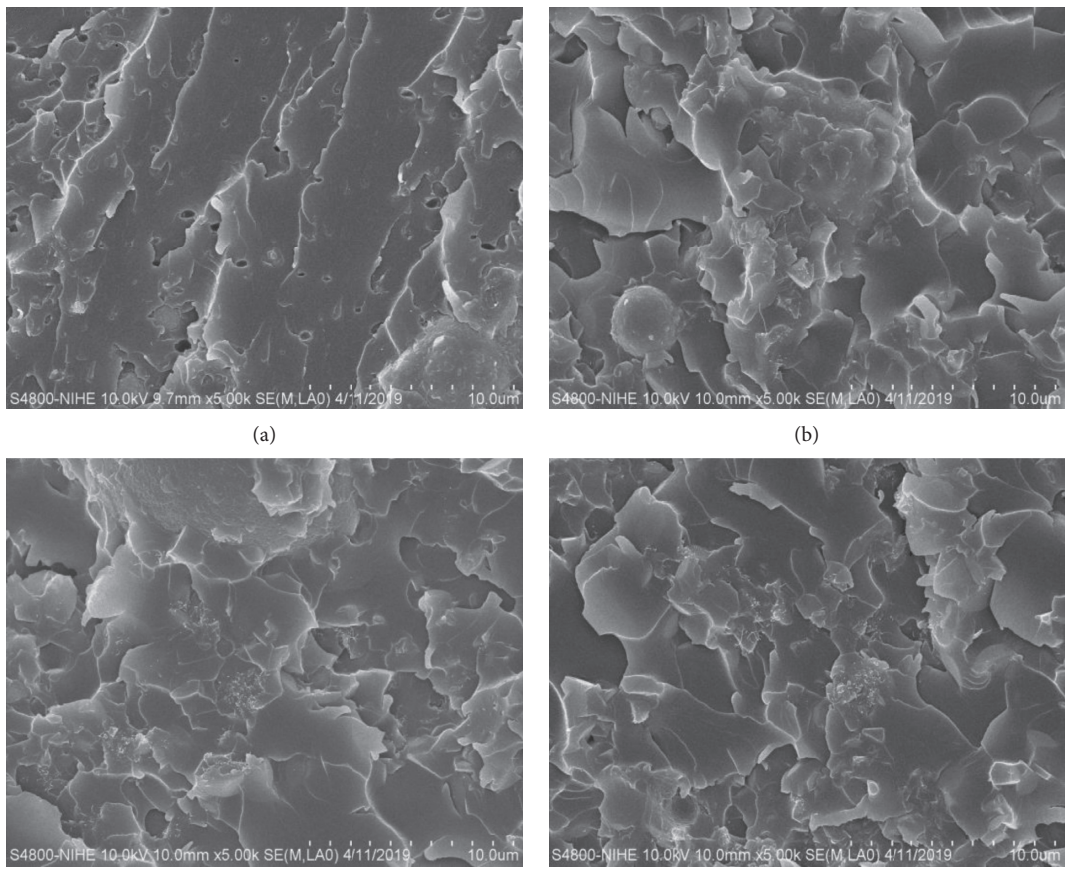

Figure 5: SEM images of nanocomposites fly ash/MWCNTs/epoxy: (a) 30 wt.% fly ash/0.03 wt.% MWCNTs/epoxy; (b) 40 wt.% fly ash/0.03 wt.% MWCNTs/epoxy; (c) 40 wt.% fly ash/0.04 wt.% MWCNTs/epoxy; and (d) 40 wt.% fly ash/0.05 wt.% MWCNTs/epoxy.

micrograph shows the dispersion (Figures 6(a) and 6(b)) and agglomeration (Figure 6(c)) of MWCNT in epoxy resin.

Meanwhile, the MWCNTs are evenly distributed and crept into the area interspersed with fly ash; there is no clustering and agglomeration phenomenon, which shows the good compatibility of the MWCNTs-fly ash-epoxy E240 combination, especially at manufacturing rates: 0.04% MWCNTs/40% fly ash (see Figures 7(a) and 7(b)).

This can be explained that at the mixing level of 40% by weight of fly ash and 0.04% by weight of MWCNTs, the material achieves high compatibility, the condensed structure is suitable for mechanical properties and fire resistance.

3.2. Mechanical Properties. The fractured surface is very rough which proves that the material has a high strength, so the destruction is difficult. MWCNTs play an important role in limiting the development of fractures (Table 3) and require great force.

The mechanical strength of nanocomposite materials (tensile strength, flexural strength, compressive strength, and Izod impact resistance) is shown in Table 3.

The mechanical strength of the sample has been improved at the mixing ratio of 40% by weight of fly ash and 0.04% by weight of MWCNTs. In other proportions, the mechanical properties tend to decrease, possibly due to the limited dispersion ability, thus reducing the mechanical strength.

From the research, the results show that tensile strength, flexural strength, and impact strength tend to decrease as fly ash content increases while compressive strength increases. However, when adding nanoadditive MWCNTs, the mechanical strength above has been significantly improved. The research results show that at the rate of 40 wt.% fly ash combined with 0.04 wt.% MWCNTs, the mechanical durability is at a high level suitable to meet the needs of manufacturing applied products. This can be explained as follows: at the content of 40 wt.% fly ash, 0.04 wt.% MWCNTs achieved the best compatibility, when increasing the content of fly ash and MWCNTs, the viscosity increased sharply and, hence, the properties of the material were reduced, resulting in insufficient base resin to cover the fly ash particles. Therefore, a part of fly ash additive does not absorb enough plastic, causing defects in the material to reduce durability.

Under the effect of stress, the epoxy material will show cracks in the most critical areas and those cracks will grow, in the presence of MWCNTs which are dispersed evenly with nanometer size in epoxy; cracks can be effectively

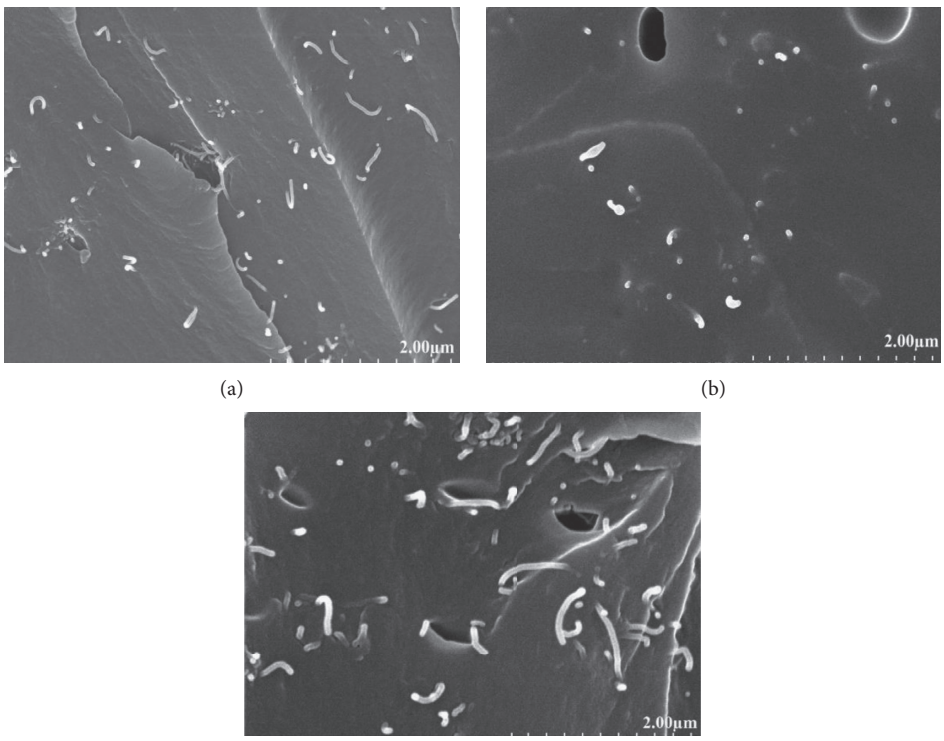

(a) (b)

(c)

Figure 6: SEM images of nanocomposites fly ash/MWCNTs/epoxy: (a) 40 wt.% fly ash/0.04 wt.% MWCNTs/epoxy; (b) 40 wt.% fly ash/0.03 wt.% MWCNTs/epoxy; and (c) 40 wt.% fly ash/0.05 wt.% MWCNTs/epoxy.

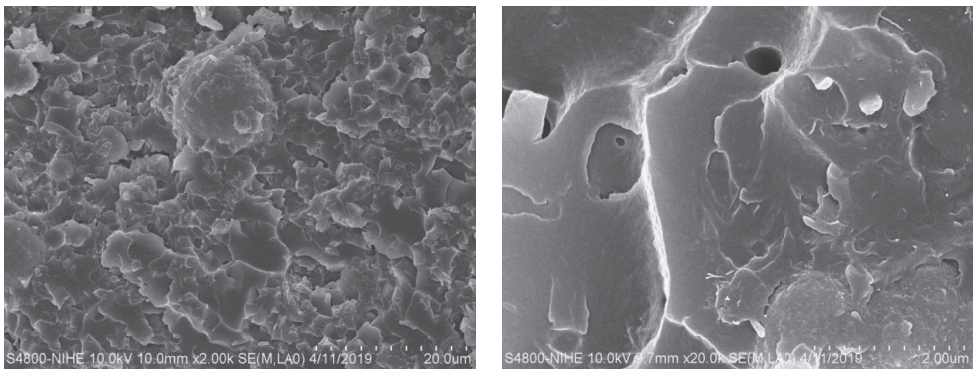

(a) (b)

Figure 7: SEM images of nanocomposites fly ash/MWCNTs/epoxy: 40 wt.% fly ash/0.04 wt.%/epoxy.

prevented, and cracks change direction when they pass over the point where MWCNTs are present. As a result, cracks begin to become difficult to develop.

From the table of results of mechanical properties, the tensile strength compared with the results of Sroka et al. published was almost similar. In the work of Sroka et al. [3, 4], fly ash was modified, while in this work, the interwoven structure of nano additives (MWCNTs) increased material sustainable cooperation and had reinforcing role for materials. The mechanical properties have been improved and still ensure the tensile strength is kept at the prescribed level.

3.3. Fire Retardant Properties. If a layer of ash can be formed during the combustion of polymers, it can act as an insulating sheet, limiting heat transfer from the source to the polymers. Therefore, the number and texture of ash layers is important to limit the combustion of polymers.

Fly ash flame retardants and MWCNTs are dispersed in epoxy resins to enhance the flame retardant properties of epoxy resins. The results of fire resistance assessment of the fly ash/MWCNTs combination for epoxy are shown in Table 4.

From Table 4, it was found that the best results were a combination of 0.04% by weight of MWCNTs and 40% by weight of fly ash, LOI index of 26.8%, combustion rate of

Table 3: Optimum mechanical properties of epoxy/fly ash/MWNT nanocomposites from fine tuning experiments.

Trial	Sample code	Fly ash content (wt%)	MWCNTs content (wt%)	Tensile strength (MPa)	Flexural strength (MPa)	Compressive strength (MPa)	Impact strength (kJ/m^2)
1	**Epoxy**	0.00	0.00	55.90	86.75	156.08	7.11
2	FA01	0.00	0.03	65.89	91.37	189.39	10.07
3	FA02	30	0.00	39.47	60.08	165.12	5.90
4	FAST1	30	0.03	52.50	77.09	170.00	6.50
5	FAST2	40	0.03	50.04	72.10	173.25	7.90
6	FAST3	50	0.03	44.44	68.25	175.05	8.80
7	FAST4	30	0.04	59.03	78.55	188.89	10.75
8	**FAST5**	**40**	**0.04**	**58.79**	**79.39**	**225.09**	**16.09**
9	FAST6	50	0.04	47.02	71.19	220.21	14.68
10	FAST7	30	0.05	56.15	76.97	218.09	14.87
11	FAST8	40	0.05	54.12	73.60	223.09	16.37
12	FAST9	50	0.05	49.60	71.77	229.88	15.76

The bold values indicate that at the fabrication rate of 40 percent by weight of fly ash combined with 0.04 percent by weight of MWCNTs, the mechanical properties of the material are improved more than the others.

Table 4: Results for flammability tests (reaction to small flame) oxygen index (OI) and UL 94 for fly ash/MWCNTs/epoxy nanocomposites.

Trial	Material	Fly ash content (wt%)	MWCNTs content (wt%)	LOI (vol% O2 $\pm 2\sigma$)	Combustion rate (mm/min)	UL94 HB (mm/min)
1	Epoxy	0.00	0.00	20.6	28.41	Not rated (NR)
2	FA01	0.00	0.03	21.9	24.90	21.76 (HB)
3	FA02	30	0.00	21.5	26.12	22.08 (HB)
4	FAST1	30	0.03	23.7	25.21	20.87 (HB)
5	FAST2	40	0.03	24.1	22.05	18.55 (HB)
6	FAST3	50	0.03	25.0	21.44	17.71 (HB)
7	FAST4	30	0.04	25.4	18.45	16.45 (HB)
8	**FAST5**	**40**	**0.04**	**26.8**	**16.05**	**15.67 (HB)**
9	FAST6	50	0.04	26.3	15.34	15.05 (HB)
10	FAST7	30	0.05	26.3	17.32	17.67 (HB)
11	FAST8	40	0.05	26.8	16.47	16.79 (HB)
12	FAST9	50	0.05	26.3	27.81	18.09 (HB)

The bold values indicate that at the manufacturing rate of 40 percent by weight of fly ash combined with 0.04 percent by weight of MWCNTs, the flame retardant properties of the material are improved more than other rates.

16.05 mm/minute, and combustion rate with UL. 94HB reaches 15.67 mm/minute.

A layer of coal (ash) is spread evenly keeping the sample without the drip and improved the flame resistance of epoxy. The combination of fire protection mechanisms has improved the fire resistance of the material.

When MWCNTs are well dispersed in the substrate, the created coal layer will cover more evenly on the surface. And this shield will minimize the ability ignition as well as exposure to air oxygen. At the same time, it reduces the tendency to catch fire again, making the fire unable to spread and extinguish. It can be seen that the more uniform the distribution of fire retardant additives in the substrate, the greater the fire resistance and mechanical properties of nanocomposite are improved.

A layer of residue generated from MWCNTs and fly ash on the sample surface during combustion is very important, acting as a heat shield and preventing heat spread. It may delay the transfer of heat from the flame, resulting in a slower increase in temperature. It can be said that MWCNTs and fly ash have synergized to increase the high fire resistance of composites; these are environmentally friendly flame retardants that promise great applicability in life.

This was confirmed by the qualitative investigation by FE-SEM, which revealed the presence and dispersion of some relatively large MWCNT agglomerates, as shown in Figure 7. The fracture surface shows a typical brittle failure in between the nanotubes and epoxy resin. This indicates that the strong adhesion takes place in between MWCNT–epoxy resin and fractured in different planes. When the loading increases, the cracks will form in the weak area of the MWCNT network.

The multiwalled carbon nanotubes play an important role in pinning crack (Figure 8(b)) and carry more external force (the crack (red arrow) is blocked by nanoparticles). They have a firm connection and strong interaction with the matrix. So, the carbon nanotubes, effectively, prevent the expansion of microcracks resulting from the stress concentration and improve the strength of composites.

Multiwalled carbon nanotube increases the performance of pure epoxy resin because of resisting the deformation of matrix. However, uniform dispersion and perfect adhesion of MWCNTs in the epoxy resin is the main reason to increase the mechanical properties of epoxy resin. Therefore, the mechanical properties and flame retardant of nanocomposite materials (40% by weight of fly ash, 0.04% by weight of MWCNTs) achieved better value than the other samples.

When increasing the percentage of fly ash to 50 parts by weight, the fire retardation tends to decrease. At this ratio the

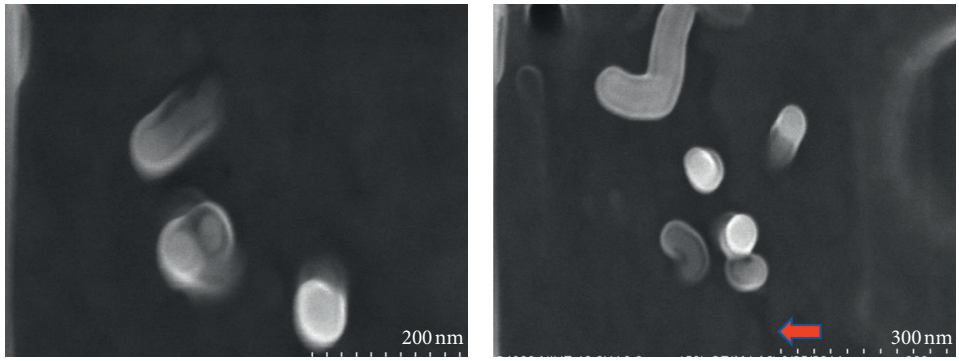

(a) (b)

Figure 8: FE-SEM images of nanocomposites fly ash/MWCNTs/epoxy: 40 wt.% fly ash/0.04 wt.% MWCNTs/epoxy ((a), (b)).

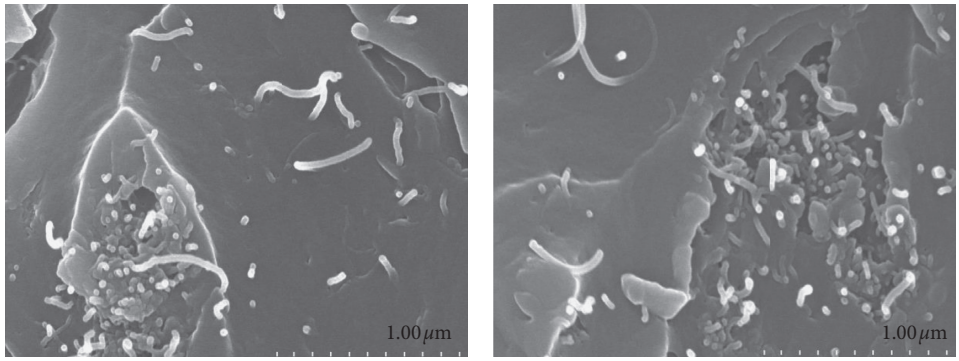

(a) (b)

Figure 9: FE-SEM images of nanocomposites: (a) fly ash/MWCNTs/epoxy: 50 wt.% fly ash/0.03 wt.% MWCNTs/epoxy and (b) fly ash/MWCNTs/epoxy: 50 wt.% fly ash/0.05 wt.% MWCNTs/epoxy.

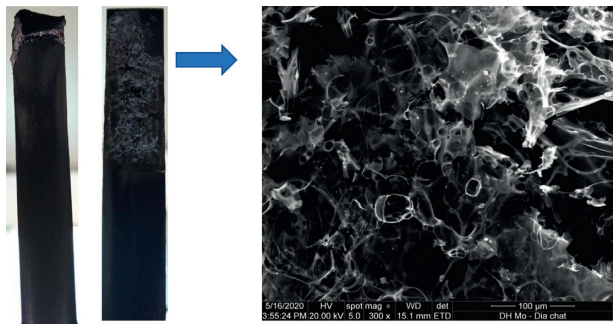

Figure 10: SEM morphologies of the residua of nanocomposites fly ash/MWCNTs/epoxy: 40 wt.% fly ash/0.04 wt.% from ignition by alcohol burner (UL 94HB).

compatibility between fly ash and MWCNTs decreases, because then the viscosity of the mixture increases due to fly ash. Therefore, the dispersion ability of MWCNTs will be more difficult. The agglomeration as well as poor dispersion ability of MWCNTs will seriously affect the fireproof properties as well as the mechanical properties (see Figures 9(a) and 9(b)).

Extraordinarily, the residual char of nanocomposite (Figure 10) was very dense and continuous; no holes could be found. This was determined by the dispersion states of CNTs in the residues. In the char of nanocomposite (Figure 10), a lot of MWCNTs aggregates could be found. This implies that MWCNTs reaggregated during combustion.

From the results of Table 4, the role of nanoadditives (MWCNTs) in the fire resistance of materials is clearly recognized . Compared to the results published by Divya et al. [7], the trend is the same rule despite different background studies. Divya et al. published that 0.2 wt.%

MWCNTs combined with 20 wt.% fly ash is the optimal value. In this work, meanwhile, the optimal ratio is 0.04 wt.% MWCNTs combined with 40 wt.% fly ash.

4. Conclusions

We found that fly ash, which is a byproduct of thermal power plants, greatly enhanced the fire resistance of epoxy and thus reduced the amount of energy needed to produce flame retardant epoxy. Adding a large amount of fly ash (40 wt.%) reduces the mechanical properties and molding capabilities of the material. However, the fire retardation is enhanced and the mechanical properties are significantly improved due to the presence of MWCNTs with 0.04 wt.%. The results of structural morphology (SEM) showed that fly ash mixed with epoxy at high content (30, 40, and 50 wt.%) had good compatibility with the substrate even in the presence of nanoadditives (MWCNTs), thus promising the future environmentally friendly green composites with many practical applications.

In this work, the surface of fly ash has not been modified so the compatibility with the base resin is not strong compared with what has been observed in previous works [2, 3]. However, due to the synergies between unmodified fly ash and multiwalled carbon nanotubes (MWCNTs) at an appropriate fabrication rate, the manufacturing materials ensure mechanical properties and fire retardation at the prescribed level. Nanocomposite materials can be applied in industrial consumer electronics and construction materials with high fire resistance.

Data Availability

The data used to support the findings of this study are included within the article.

Conflicts of Interest

The authors declare that there are no conflicts of interest regarding the publication of this paper

Acknowledgments

The authors wish to thank the Faculty of Chemical Technology, Hanoi University of Industry, for funding this work.

References

[1] A. A. Jumaat, N. F. Afandi, A. Manap, R. A. Zainuddin, S. Mahalingam, and N. F. Abd Kadir, "Synthesis of multiwall carbon nanotube with fly ash in the production of desired green concrete," *Journal of Physics: Conference Series*, vol. 1349, Article ID 012021, 2019.

[2] M. Singla and V. Chawla, "Mechanical properties of epoxy resin-fly ash composite," *Journal of Minerals and Materials Characterization and Engineering*, vol. 9, no. 3, pp. 199–210, 2010.

[3] J. Sroka, A. Rybak, R. Sekula et al., "An investigation into the influence of filler silanization conditions on mechanical and thermal parameters of epoxy resin-fly ash composites," *Journal of Polymers and the Environment*, vol. 24, no. 4, pp. 298–308, 2016.

[4] J. Sroka, A. Rybak, R. Sekula et al., "Two-step procedure of fly ash modification as an alternative method for creation of functional composite," *Journal of Polymers and the Environment*, vol. 25, no. 4, pp. 1342–1347, 2016.

[5] T. Chaowasakoo and N. Sombatsompop, "Mechanical and morphological properties of fly ash/epoxy composites using conventional thermal and microwave curing methods," *Composites Science and Technology*, vol. 67, no. 11-12, pp. 2282–2291, 2007.

[6] T. A. Nguyen, Q. T. Nguyen, T. P. Bach, and V. H. Nguyen, "Study on fire resistance ability and mechanical properties of composites based on epikote 240 epoxy resin and thermoelectric fly ash: an ecofriendly additive," *Journal of Chemistry*, vol. 2019, Article ID 2635231, 8 pages, 2019.

[7] V. C. Divya, M. A. Khan, B. N. Rao, R. R. N. Sailaja, and S. Vynatheya, "Fire retardancy characteristics and mechanical properties of high-density polyethylene/ultrafine fly ash/MWCNT nanocomposites," *Polymer-Plastics Technology and Engineering*, vol. 56, no. 7, pp. 762–776, 2016.

[8] M. Soyama, K. Inoue, and M. Iji, "Flame retardancy of polycarbonate enhanced by adding fly ash," *Polymers for Advanced Technologies*, vol. 18, no. 5, pp. 386–391, 2007.

[9] J. Sim, Y. Kang, B. J. Kim, Y. Ho Park, and Y. C. Lee, "Preparation of fly ash/epoxy composites and its effects on mechanical properties," *Polymers*, vol. 12, no. 79, pp. 1–12, 2020.

[10] A. Pattanaik, M. Mukharjee, and S. C. Mishra, "Effect of environmental aging conditions on the properties of fly ash filled epoxy composites," *Advanced Composite Materia*, vol. 29, no. 1, pp. 1–30, 2020.

[11] P. Bachtrong, L. Nguyenthanh, and H. Phamthi, "Effect of fly ash from thermal power plant on the dielectric properties of polymer composites materials based on matrix epoxy DER 331," *Chemical Engineering Transactions*, vol. 56, pp. 1207–1212, 2017.

[12] P. Rovnaník, H. Šimonová, L. Topolář, P. Schmid, and Z. Keršner, "Effect of carbon nanotubes on the mechanical fracture properties of fly ash geopolymer," *Procedia Engineering*, vol. 151, pp. 321–328, 2016.

[13] M. Saafi, K. Andrew, P. L. Tang et al., "Multifunctional properties of carbon nanotube/fly ash geopolymeric nanocomposites," *Construction and Building Materials*, vol. 49, pp. 46–55, 2013.

[14] T. A. Nguyen, "Effects of the amount of fly ash modified by stearic acid compound on mechanical properties, flame retardant ability, and structure of the composites," *International Journal of Chemical Engineering*, vol. 2020, Article ID 2353827, 8 pages, 2020.

[15] T. A. Nguyen, "Effects of the amount of fly ash modified by stearic acid compound on mechanical properties, flame retardant ability, and structure of the composites," *International Journal of Chemical Engineering*, vol. 2020, Article ID 2079189, 6 pages, 2020.

Hindawi
Journal of Chemistry
Volume 2020, Article ID 1472923, 13 pages
https://doi.org/10.1155/2020/1472923

Research Article

Biocementation Influence on Flexural Strength and Chloride Ingress by *Lysinibacillus sphaericus* and *Bacillus megaterium* in Mortar Structures

Daniel Karanja Mutitu,[1] **Jackson Muthengia Wachira**,[1] **Romano Mwirichia**,[2] **Joseph Karanja Thiong'o**,[3] **Onesmus Mulwa Munyao**,[3] **and Muriithi Genson**[2]

[1]*Department of Physical Sciences, University of Embu, Embu, Kenya*
[2]*Department of Biological Sciences, University of Embu, Embu, Kenya*
[3]*Department of Chemistry, Kenyatta University, Nairobi, Kenya*

Correspondence should be addressed to Daniel Karanja Mutitu; mutsonjnr@gmail.com

Received 27 January 2020; Revised 2 April 2020; Accepted 27 April 2020; Published 28 May 2020

Guest Editor: Jorge Sanjurjo-Sánchez

The concrete/mortar durability performance depends mainly on the environmental conditions, the microstructures, and its chemistry. Cement structures are subject to deterioration by the ingress of aggressive media. This study focused on the effects of *Bacillus megaterium* and *Lysinibacillus sphaericus* on flexural strength and chloride ingress in mortar prisms. Microbial solutions with a concentration of 1.0×10^7 cells/ml were mixed with ordinary Portland cement (OPC 42.5 N) to make mortar prisms at a water/cement ratio of 0.5. Four mortar categories were obtained from each bacterium based on mix and curing solution. Mortar prisms of 160 mm × 40 mm × 40 mm were used in this study. Flexural strength across all mortar categories was determined at the 14^{th}, 28^{th}, and 56^{th} day of curing. Mortars prepared and cured using bacterial solution across all curing ages exhibited the highest flexural strength as well as the highest percent flexural strength gain. *Lysinibacillus sphaericus* mortars across all mortar categories showed higher flexural strength and percent flexural strength gain than *Bacillus megaterium* mortars. The highest percent flexural strength gain of 33.3% and 37.0% was exhibited by the 28^{th} and 56^{th} day of curing, respectively. The mortars were subjected to laboratory prepared 3.5% by mass of sodium chloride solution under the accelerated ion migration test method for thirty-six hours using a 12 V Direct Current power source after their 28^{th} day of curing. After subjecting the mortar cubes to Cl media, their core powder was analyzed for Cl content. From these results, the apparent diffusion coefficient, D_{app}, was approximated from solutions to Fick's 2^{nd} Law using the error function. *Bacillus megaterium* mortars across all mortar categories showed lower apparent diffusion coefficient values with the lowest being 2.6456×10^{-10} while the highest value for *Lysinibacillus sphaericus* mortars was 2.8005×10^{-10}. Both of the test bacteria lowered the ordinary Portland cement Cl-ingress but *Bacillus megaterium* was significantly more effective than *Lysinibacillus sphaericus* in inhibition.

1. Introduction

The durability of concrete/mortar is related to the characteristics of its pore structure [1]. Furthermore, permeability of concrete/mortar is dependent on the porosity and the connectivity of the pores [2, 3]. The degradation mechanisms often depend on the way potentially aggressive substances can penetrate the cement-based material, possibly causing damage [4]. The more open the pore structure and connectivity of the pores, the more vulnerable it is to degradation caused by penetrating substances [5, 6].

One of the predominant causes of the corrosion of steel in cement-based structures is chloride attack [7–9]. Chloride ions may be present in a cementitious material either as a result of aggressive ions ingress or incorporation of the aggressive ions during concrete/mortar preparation.

Chloride ions may also penetrate from external sources such as seawater or deicing salts. In the marine environment, the ingress of chloride is the most important problem [10, 11].

Chloride is bound if it has reacted with cement and is free if it is available in pore solution [10]. Several chemical interactions between chloride and the cement constituents do affect the chloride penetration into the concrete/mortar bulk [5, 12]. The chemical reactions of chlorides with cement paste start with calcium hydroxide and calcium aluminate hydrate, depending on the cations in solution [13].

Chloride ingress in cement-based materials is mainly through capillary absorption, permeation, and diffusion [14]. However, it may also occur through a multiple of the aforementioned mechanisms. Diffusion is the most prevalent process [15]. The ingress of chlorides/sulphates due to the various transport mechanisms obeys different laws [16]. Fick's second law of diffusion is commonly applied to quantify the aggressive ion ingress due to the multiple transport phenomena.

Chlorides react with C_3A and the C_4AF present in Portland cement to produce Friedel's salt, $Ca_6Al_2O_6{\cdot}CaCl_2{\cdot}10H_2O$, or calcium chloroferrite, $Ca_6Fe_2O_6{\cdot}CaCl_2{\cdot}10H_2O$, respectively [5, 14]. No deleterious effect is associated with these products. The reaction between the C_3A phase and free chlorides in hydrated cement leads to a reduction of Cl^- from the pore solution [17]. This lowers the risk of rebar corrosion [18]. Solutions with high concentrations of $CaCl_2$ or $MgCl_2$ may cause chemical attack which may lead to a drop in pore water pH and disruption of the cement matrix [19]. This is due to the consumption of the sparingly soluble $Ca(OH)_2$. $MgCl_2$ reacts with portlandite as shown in

$$MgCl_2\,(aq) + Ca\,(OH)_2\,(s) + 2H_2O\,(l) \longrightarrow CaCl_2 \cdot 2H_2O\,(aq) + Mg\,(OH)_2\,(s) \quad (1)$$

Biocementation in OPC lowers chloride ingress and permeability into the cement matrix [20]. This is due to the refinement of the pore structure [5]. Chloride ions penetrate a pore system and form chloride salts which may crystallize within the pores inducing internal cracks [21]. The cracks affect the mechanical and durability properties of concrete/mortar [20, 22, 23].

The high alkalinity of the concrete/mortar introduced during the bacteria MICP prevents the breakup of the passive film [25, 24]. Its carbonation accompanied by the presence of chloride ions lowers the alkalinity of pore water. Rasheeduzafar et al. [18], Dousti et al. [21], and Rao and Meena [26] observed the amount of free chloride decrease with increasing C_3A and the amount of bound chloride decreased with increasing OH-concentration from the cement. Given this, the high corrosion of rebars exposed to chloride media can be assumed to be due to the low alkalinity of pore solution [21, 22, 27].

OPC based structures are well known for achieving high early compressive and flexural strength due to large content and early hydration of C_3S [15, 28, 29]. Despite the various OPC concrete/mortar advantages, it has a more open pore structure than blended cement structures [3, 15, 30]. OPC-made structures also have a high tendency to form cracks during and after curing allowing aggressive substances to penetrate the structure. Permeability or cracks are one of the main causes of deterioration of these structures and decrease in durability. Treatment of cracks and pores are generally divided into passive and active treatments. Passive treatments can only heal the surface cracks, while active treatments can heal both interior and exterior cracks [22, 25].

Microbial concrete/mortar biologically produce calcium carbonate (limestone) to seal pores that appear within its matrix or seal/repair cracks that appear on the structure's surface [25, 31]. These microbial deposits could also establish nucleation sites that enhance the early cement hydration process leading to improved compressive and flexural strengths. Microbial precipitation of calcium carbonate mainly occurs by hydrolyzing urea. Urea hydrolysis is a chemical reaction in which urea reacts with water and produces ionic products as shown in the following equation:

$$CO\,(NH_2)_2 + 2H_2O \xrightarrow{\text{Urease}} {CO_3}^{2-} + {NH_4}^{1+} \quad (2)$$

When this reaction occurs in the presence of Ca^{2+}, $CaCO_3$ (solid) is formed as shown in the following equation:

$$Ca^{2+} + {CO_3}^{2-} \longrightarrow CaCO_3 \quad (3)$$

When this reaction occurs inside a cementitious porous material, after settling, it produces sediment, a coating, and a bridge is formed sequentially around and between the particles and increases interparticle linkage [31].

Specific types of the bacteria genus such as *Bacillus* along with a calcium-based nutrient, such as calcium lactate, or calcium nitrate could be added to the ingredients of the concrete/mortar when it is being mixed [21]. The soluble calcium-containing nutrient is converted to insoluble calcium carbonate [22, 32]. The calcium carbonate solidifies on the cracked surface, thereby sealing it up.

The densification of cementitious material due to microbial reaction is important in reducing the permeability of aggressive ions. This paper reports on findings of the flexural strength gain of MICP-containing Kenyan-made OPC and lowered diffusivity of chloride in such laboratory-made mortars.

2. Materials and Methods

2.1. Cement Chemical Analysis. In this study, the ordinary Portland cement (OPC 42.5 N), KS EAS 18-1:2017 [33], and standard sand, ISO 679:1989 [34], were used. Flexural strength tests were carried out in accordance to ASTM C293: 1990 [35]. 100 g sample of the test cement sample was prepared and analyzed in the usual manner following KS EAS 18-1:2017 [33]. Loss on ignition was done following ASTM D7348: 2013 [37]. The results are given in Table 1.

Using Bogues formula [36], the average phase composition for the test OPC is $65.115 \pm 0.854\%$, $14.485 \pm 0.913\%$, $3.899 \pm 0.013\%$, and $10.355 \pm 0.018\%$ for C_3S, C_2S, C_3A, and C_4AF, respectively.

Table 1: OPC chemical analysis results.

Sample	Cement composition % w/w ± SD									
	Al_2O_3	SiO_2	SO_3	Na_2O	K_2O	CaO	MgO	Fe_2O_3	MnO	LOI
Avg.	3.643 ± 0.010	22.182 ± 0.010	2.695 ± 0.021	0.410 ± 0.001	0.975 ± 0.006	64.627 ± 0.042	2.084 ± 0.025	3.403 ± 0.012	0.173 ± 0.001	1.519 ± 0.001

2.2. Microbial Culturing Nutrients. Analytical grade chemicals were used in the preparation of the culture media. Calcium lactate, $C_6H_{10}O_6Ca$, peptone from casein and other animal proteins, meat extract, agar, sodium hydrogen carbonate ($NaHCO_3$), anhydrous sodium carbonate (Na_2CO_3), and distilled water among other nutrients were purchased from Chem-Labs Limited, Nairobi, Kenya. *Lysinibacillus sphaericus* bacteria (DSM 28) and *Bacillus megaterium* (DSM 32) were purchased from Leibniz-Institut DSMZ-Deutsche Sammlung von, Germany.

2.2.1. Lysinibacillus sphaericus Microbial Culturing. The *Lysinibacillus sphaericus* microbial solution was cultured using nutrients as per the supplier manual. The liquid medium chosen for culturing the bacteria consisted of 5.00 g of peptone added to 3.00 g of meat extract and 3.95 g of calcium acetate per liter of distilled water was mixed to obtain liquid medium per stock culture. Initially, this mixture was sterilized for 20 minutes at a temperature of 121°C by autoclaving. This mixture was then cooled to room temperature. After cooling, a 1 M Na-sesquicarbonate solution (1.0 ml in 10.0 ml) prepared by mixing 4.2 g $NaHCO_3$ with 5.3 g anhydrous Na_2CO_3 and made up to 1 liter using distilled water was added to the stock culture to achieve a pH of 9.7. The *Lysinibacillus sphaericus* spore powder sample was added to this mixture in a laminar flow chamber. These cultures were then incubated on a shaker incubator at 130 shakes per minute maintained at 30°C for 72 hours. An optical density test was conducted using a spectrophotometer for determining the quantity of culture solution required to mix. This test was conducted in bacteria growing medium which was considered as blank. This solution was also taken to be the reference, for experimentation of optical density of the microbial solution. Separately, 0.5 mL of blank and bacteria solution of 0.5 mL were placed in the spectrophotometer at a wavelength of 600 nm and the machine was set to read. The microbial concentration was observed to be 1.0×10^7 cells/mL using the spectrophotometer. This microbial culture concentration was maintained throughout the mortar samples preparation as well as in prism curing solution.

2.2.2. Bacillus megaterium Microbial Culturing. The *Bacillus megaterium* microbial solution was cultured using nutrients as per the supplier manual. The same procedure and nutrients as used in preparing the *Lysinibacillus sphaericus* microbial solution were used in preparing the *Bacillus megaterium* microbial solution. The *Bacillus megaterium* spore powder sample was added instead of *Lysinibacillus sphaericus*.

Figure 1 shows (a) OPC mortar prepared and being cured in distilled water, (b) OPC mortar prepared using *Bacillus megaterium* solution but being cured in distilled water, (c) OPC mortar prepared using distilled water but being cured in *Bacillus megaterium* solution and (d) OPC mortar prepared and being cured in *Bacillus megaterium* solution.

2.3. Mortar Prism Molding and Flexural Strength Testing. Mortar mix prisms were fabricated according to KS EAS 18-1:2017 [33]. 450 g of OPC was placed in the mixing basin of an automatic programmable mixer model number JJ-5. 225.0 ml of distilled water was then added. The mix basin and its contents were clamped onto the automatic programmable mixer and allowed to run for three minutes. 1350 ± 5 g of the standard sand was placed in an automatic pour-trough and allowed to add automatically, until all 1350 ± 5 g sample was added while the mixer was still running at a speed of 30 vibrations per minute. The machine was let to run for ten minutes. The mortar prepared had w/c ratio of 0.5 and was sufficient to prepare three mortar prisms. Once the mortar was mixed, it was poured into steel molds of $40\,\text{mm} \times 40\,\text{mm} \times 160\,\text{mm}$. Using a trowel, the mortar paste was scooped from the automatic programmable mixing basin and placed in a compaction mold of a jolting compaction machine with 60 rpm vibrations. Leveling of the paste was done with a mold trowel in each of the three chambers of the mold after every jolting cycle until a good finish was achieved at the surface. The mold with the mortar paste was then placed in a humid chamber maintained at 95% humidity and 27.0°C for 24 hours. The mortar was then removed from the molds after 24 hours to obtain the usual OPC mortar. The distilled-water prepared mortars were categorized into two categories depending on their curing regime. The first category was cured in distilled water (labeled as OPC-H_2O [H_2O]). The second category was cured in microbial solution (labeled as OPC-H_2O [LB] for *Lysinibacillus sphaericus* and OPC-H_2O [BM] for *Bacillus megaterium*). The above procedure was repeated but this time using 225 ml of the microbial solution as mix media instead of distilled water which resulted in two more mortar categories (referred to as the third and fourth category): the third category was the OPC mortar prepared using the microbial solution and cured in distilled water (labeled as OPC-LB [H_2O] *Lysinibacillus sphaericus* and OPC-BM [H_2O] for *Bacillus megaterium*), while the fourth category was the OPC mortar prepared using the microbial solution and cured in microbial solution (labeled as OPC-LB [LB] for *Lysinibacillus sphaericus* and OPC-BM [BM] for *Bacillus megaterium*). The mortars were placed in requisite water or microbial solution for curing in a chamber maintained at 27 ± 1°C for curing. The flexural strength tests were conducted at the 2^{nd}, 7^{th}, 14^{th}, 28^{th}, and 56^{th} day of curing. Flexural strength tests in this study were performed on three samples per category for obtaining average results.

2.4. Scanning Electron Microscopy (SEM) Sample Preparation and Analysis. SEM analysis was determined for each set of test mortars after the 28^{th} day of curing. The SEM model used was Zeiss Ultra Plug FEG-SEM. The test mortar was prepared for SEM analysis as described in Scrivener et al.'s [38] guide for microstructural analysis of cementitious materials as summarized in Figure 2. Isopropanol alcohol was used to stop the hydration process while resin ERL-4206 was used to impregnate the hardened cement mortar.

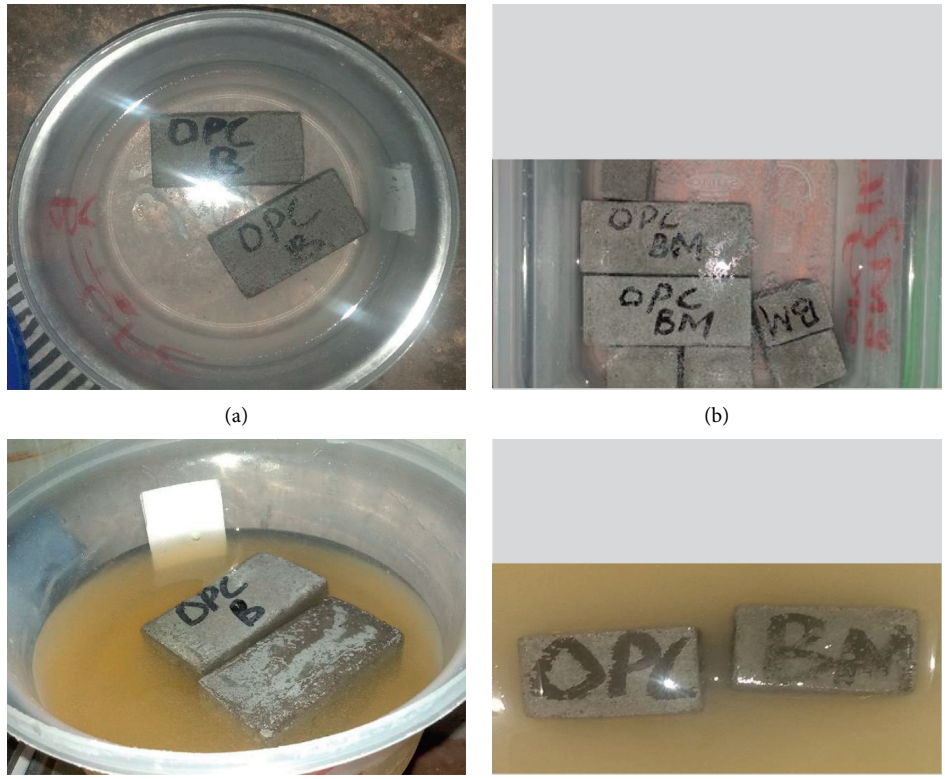

(a) (b) (c) (d)

Figure 1: Cement mortar curing in varied regimes. (a) OPC-H_2O [H_2O]. (b) OPC-BM [H_2O]. (c) OPC-H_2O [BM]. (d) OPC-BM [BM].

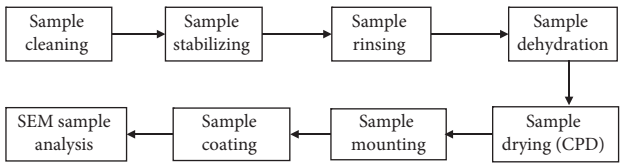

Figure 2: SEM sample preparation.

2.5. X-Ray Diffraction (XRD) Analysis. XRD analysis was determined for each set of test mortars after the 28th day of curing. The mineralogy of the newly formed cement hydration/bacterial material was determined using an X-Ray Diffraction (XRD) Instrument PW1710 Phillips. Before running the XRD analysis samples were oven-dried at 100°C and powdered with an electronic grinder. They were then placed in a zero-background silicon sample holder. The goniometer was calibrated using a silicon standard. Samples were analyzed using PANalytical software, with goniometer start and end angles at 5.00 and 80.002°Theta, step size of 0.0202°Theta, and scan step time of 0.5 seconds at an adjusted current and voltage of 40 mA and 35 kV. respectively.

2.6. Chloride Ingress. For each category of mortar, three prisms, cured for 28 days, were subjected to chloride profiling using the method prescribed in ASTM C 1552 [39]. After the NaCl solution exposure, a mortar prism was polished on the 40 mm × 40 mm face using sandpaper. The prism was drilled through the core center up to 10 mm interval along the length using a 15 mm radius drill bit up to 80 mm per mortar category. The powder was dried to a constant mass in an oven at 105°C. The dried powder was pulverized. Between each pulverization, the pulverizer was thoroughly cleaned to avoid cross-sample contamination. The ground samples were kept in individual-sample sealed reagent bottles awaiting chloride analysis.

2.6.1. Chloride Profiling. The chlorides at each depth of penetration were analyzed using Mohr titration procedure in all the mortar categories. The estimation of apparent chloride diffusion coefficients was achieved under non-steady state conditions assuming boundary conditions $C_{(x,t)} = 0$ at $t = 0$, $0 < x < \infty$, $C_{(x,t)} = C_s$ at $x = 0$, $0 < t < \infty$, constant effects of coexisting ions, linear chloride binding, and one-dimensional diffusion into semi-infinite solid [16]. Crank's solution to Fick's second law of diffusion is given by

$$C_{(x,t)} = C_{(s)}\left\{1 - \operatorname{erf}\left(\frac{x}{\left(4D_{\text{app}}t\right)^{(1/2)}}\right)\right\}, \quad (4)$$

where $C_{(x,t)}$ is the concentration of Cl^- at any depth x in the mortar bulk at time t, C_s is the surface concentration, and D_{app} is the apparent diffusion coefficient. The error correction function, erf, is the Gaussian error function obtained from computer spreadsheets. The chloride profiles were obtained by fitting equation (4) to experimentally

determined chloride profile concentrations, thus determining the values of D_{app} and C_s mathematically.

By using the accelerated migration diffusion coefficient D_{mig} determined graphically, D_{app} can be determined by using the following equation [40]:

$$D_{app} = \frac{RT}{ziF} D_{mig} \frac{Int^2}{\Delta \varnothing}, \quad (5)$$

where R is the Gas constant, F is the Faraday constant, T is the temperature of the electrolyte in K, zi is the valency of the ion i, $\Delta\varnothing$ is the Effective Applied Voltage in V, and t is the duration of the test/exposure in seconds.

3. Results and Discussion

3.1. Scanning Electron Microscope (SEM) Analysis. Figures 3(a)–4(c) show SEM analysis for both control and microbial mortar prisms after the 28th day of curing. The SEM images display the formation of calcium-silicate-hydrate, C-S-H, calcium carbonate precipitation, $CaCO_3$, needle type ettringite, and presence of portlandite/calcium hydroxide, CH.

As SEM images in Figure 3(a) illustrate, the OPC-H_2O (H_2O) mortar had no visible calcium carbonate deposits. However, the SEM images in Figures 3(b)–3(d) as well in Figures 4(a)–4(c), the microbial mortars OPC-H_2O (LB), OPC-H_2O (BM), OPC-LB (H_2O), OPC-BM (H_2O), OPC-LB (LB), and OPC-BM (BM) showed significant calcium carbonate precipitates. This is attributed to the MICP deposits from both *Lysinibacillus sphaericus* and *Bacillus megaterium* either present in mix media or present in the cultured curing solution [1, 41]. The morphology of C-S-H densifies from Figure 3(b) through Figures 3(c)–3(d) as well as from Figure 4(a) through Figures 4(b)–4(c). This is attributed to the calcium carbonate precipitation by the two bacteria under study. Image (c) from Figure 3, clearly shows biodeposition over ettringite needles resulting in the formation of biofilms on their surface and plugging of the pores on the mortar structure.

3.2. X-Ray Diffraction Analysis (XRD). Table 2 shows XRD analysis results for both control and microbial mortar prisms after the 28th day of curing. The results show formation of a new hydration compound, Bavenite in both bacterial mortars.

The XRD analysis of the OPC mortars confirms that microbial biocementation introduces a new cementitious product, Bavenite, $Al_2Be_2Ca_4H_2O_{28}Si_9$, which is absent in the control mortar, OPC-H_2O (H_2O), but present in the microbial mortars, OPC-LB (LB) and OPC-BM (BM) at 2.53% and 1.33%, respectively. Calcite, $CaCO_3$, is significantly more in OPC-BM (BM) and OPC-LB (LB) at 10.27% and 10.23%, respectively, as compared with 0.64% in OPC-H_2O (H_2O). This relates with improved calcite ($CaCO_3$) deposits and depleted Portlandite, $Ca(OH)_2$, in microbial mortars as seen in SEM morphological images in Figures 3 and 4. XRD diffractograms also confirmed the same as depicted in Figures 5(a)–5(c). The depleted $Ca(OH)_2$ in microbial mortars compared to that in control mortars could be attributed to the binding of Ca^{2+} with the microbial precipitated CO_3^{2-}.

More densification of C-S-H in microbial mortars than in control mortar is observed in SEM micrographs due to the high percentage of both Bavenite, $Al_2Be_2Ca_4H_2O_{28}Si_9$, and Dellaite, $Ca_6H_2O_{13}Si_3$, either individually or as combined in OPC-BM (BM) and OPC-LB (LB) compared to in OPC-H_2O (H_2O) as depicted in Figures 5(a)–5(c) and summarized in Table 2. The XRD quantifications confirm the presence of calcite as well as more C-S-H in microbial mortars. These depositions in the pores maximized the packing density of cement mortar consequently improving the mortar's physicochemical and mechanical properties.

3.3. Flexural Strength Gain. The percent gain flexural strength results obtained at 14th, 28th, and 56th day of curing are given in Figure 6.

Table 3 summarizes the significant difference in flexural strength gain between the control and microbial mortars across 2nd, 7th, 14th, 28th, and 56th day of curing.

Across all mortar categories, for both *Lysinibacillus sphaericus* and *Bacillus megaterium* there was no significant difference ($T_{calc} = 0.5$, $p = 0.05$) in their flexural strengths at 2nd and 7th day of curing. The flexural strength across all mortar categories for both bacteria under study increased with an increase in curing age as depicted in Figure 6. Considering the control and the microbial mortars across all the test bacteria mortars, the flexural strength increase was higher and more statistically significant between the 14th and 28th day than between the 28th and 56th day of curing as demonstrated by the results in Table 3. However, among the microbial mortars, flexural strength appears to be influenced more by the type of the bacteria as well as the preparation or curing regime than the curing age.

There was a statistically significant difference in flexural strength across all microbial mortar categories between different days of curing, as well as between the *Lysinibacillus sphaericus* mortars and *Bacillus megaterium* mortars as depicted in Table 3. This could imply the fact that the formation of C-S-H increases with curing age and that introduction of the microbial solution, either during preparation of mortars or as the curing regime enhances the formation of C-S-H results in improved flexural strength.

The flexural strength improvement for mortars of both bacteria under study was more pronounced when the microbial solution was used as the mix water than as the curing regime. Across all curing ages, OPC-LB (LB) exhibited the highest percentage gain in flexural strength than the other mortar categories. The highest percent flexural strength gain was observed at the 56th day of curing at 37.0%. There was observed a statistically significant difference in percent flexural strength gain both from one curing age to another as well from one microbial mortar category to another for all microbial mortar

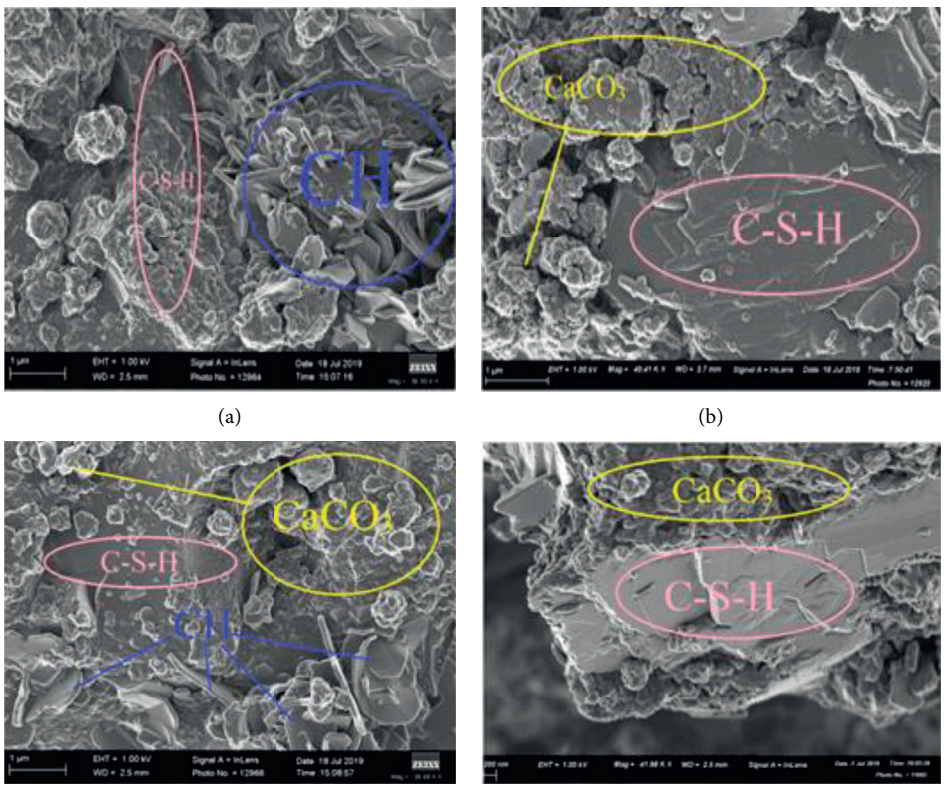

Figure 3: SEM analysis for (a) OPC-H_2O (H_2O), (b) OPC-H_2O (LB), (c) OPC-LB (H_2O), and (d) OPC-LB (LB).

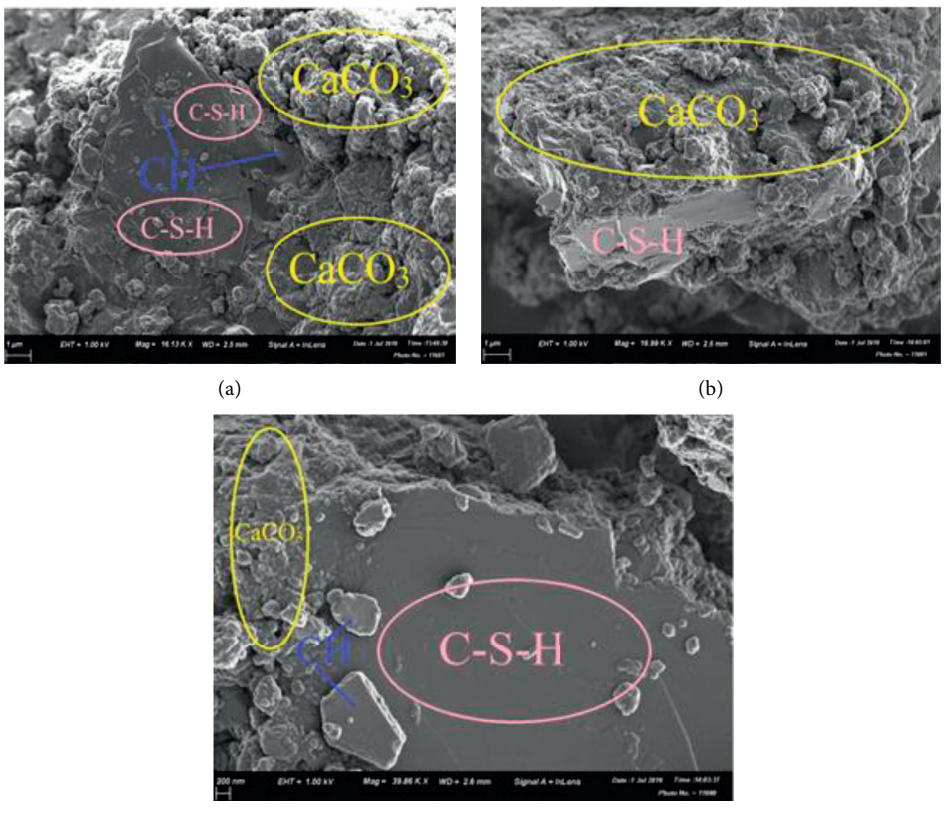

Figure 4: SEM analysis for (a) OPC-H_2O (BM), (b) OPC-BM (H_2O), and (c) OPC-BM (BM).

Table 2: XRD (% w/w ± SD values) summary for hydrated OPC microbial mortars prepared and cured in respective bacteria against control OPC mortar after 28th day of curing.

Hydration compound	Mortar category (% w/w ± SD)		
	OPC-H_2O (H_2O)	OPC-LB (LB)	OPC-BM (BM)
Bavenite, $Al_2Be_2Ca_4H_2O_{28}Si_9$			
Sample 1	—	2.55	1.36
Sample 2	—	2.52	1.33
Sample 3	—	2.51	1.29
Average	—	2.53	1.33
Std. dev.	—	±0.02	±0.03
% Average ± SD	—	2.53 ± 0.02	1.33 ± 0.03
Dellaite, $Ca_6H_2O_{13}Si_3$			
Sample 1	83.89	83.49	84.21
Sample 2	83.95	83.47	84.18
Sample 3	83.94	83.45	84.16
Average	83.93	83.47	84.18
Std. dev.	±0.03	±0.02	±0.02
% Average ± SD	83.93 ± 0.03	83.47 ± 0.02	84.18 ± 0.02
Calcite, $CaCO_3$			
Sample 1	0.67	10.26	10.24
Sample 2	0.63	10.22	10.29
Sample 3	0.61	10.21	10.27
Average	0.64	10.23	10.27
Std. dev.	±0.02	±0.02	±0.02
% Average ± SD	0.64 ± 0.02	10.23 ± 0.02	10.27 ± 0.02
Portlandite, CaH_2O_2			
Sample 1	15.43	3.86	4.21
Sample 2	15.48	3.82	4.17
Sample 3	15.49	3.84	4.19
Average	15.47	3.84	4.19
Std. dev.	±0.03	±0.02	±0.02
% Average ± SD	15.47 ± 0.03	3.84 ± 0.02	4.19 ± 0.02

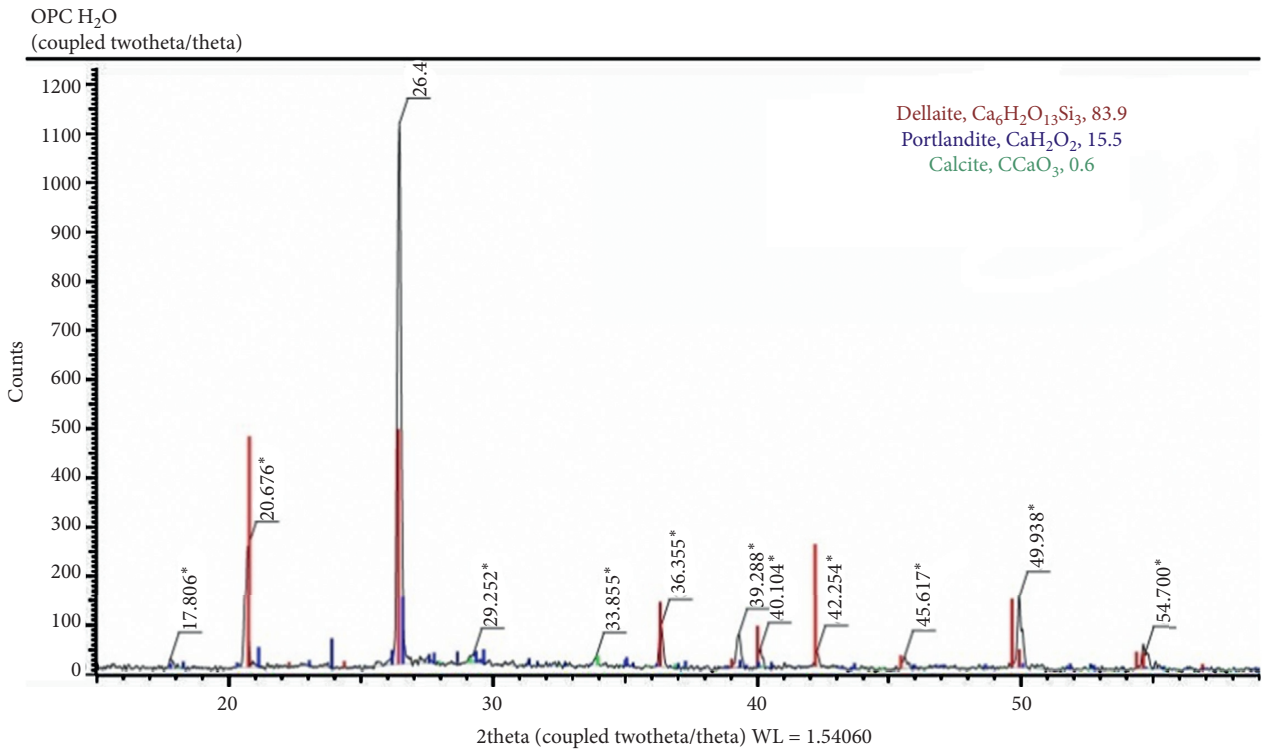

(a)

Figure 5: Continued.

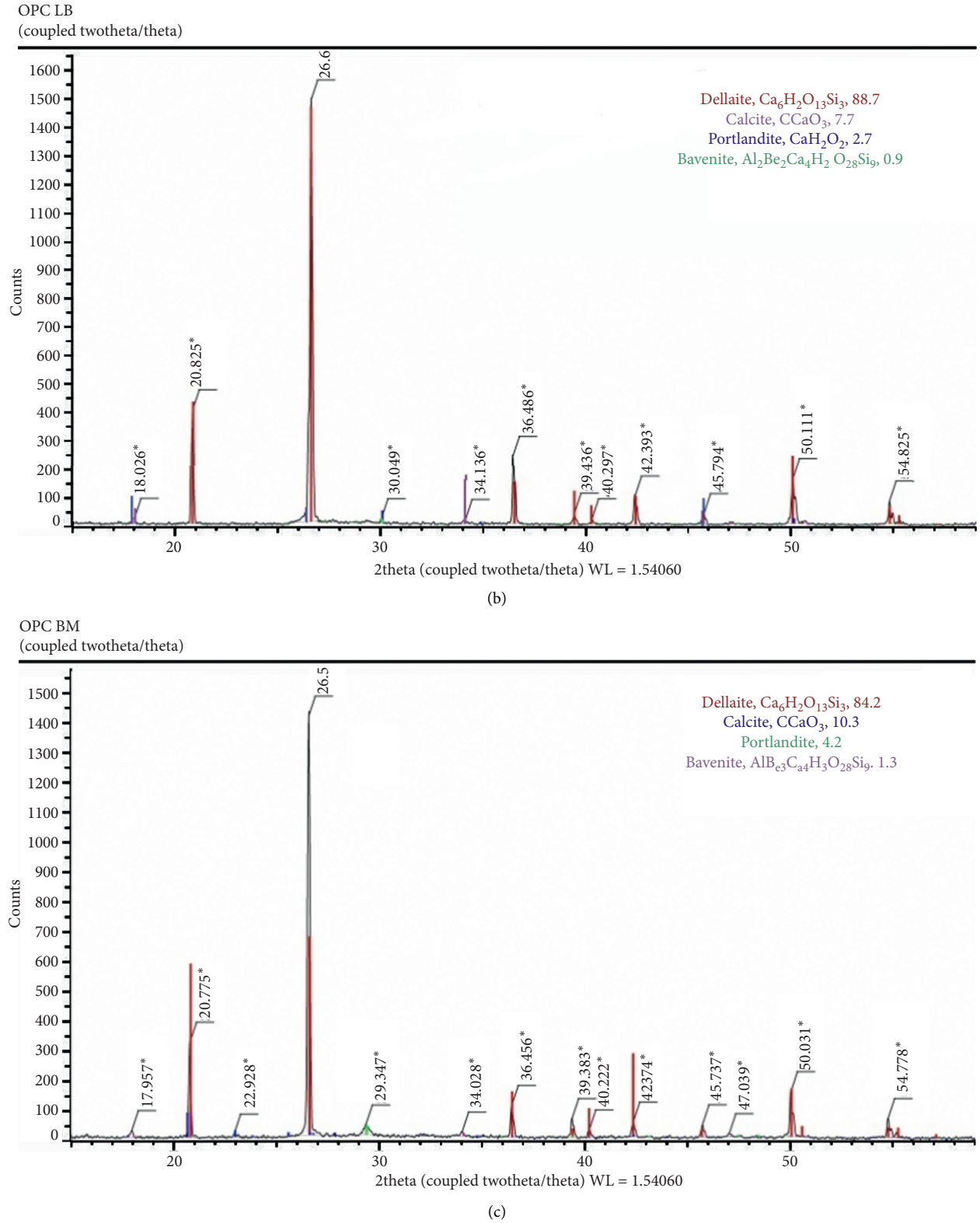

Figure 5: (a) Diffractograms for OPC-H_2O (H_2O). (b) Diffractograms for OPC-LB (LB). (c) Diffractograms for OPC-BM (BM).

categories as shown in Table 3 and Figure 7, respectively. The increase in flexural strength is attributed to the materials precipitated by the *Lysinibacillus sphaericus* being involved in the hydration process forming C-S-H responsible for strength development. The added Ca^{2+} together with calcium acetate, in presence of the microbial cell-wall as the nucleation site readily combine with the precipitated CO_3^{2-} and crystallizes out as $CaCO_3$ which

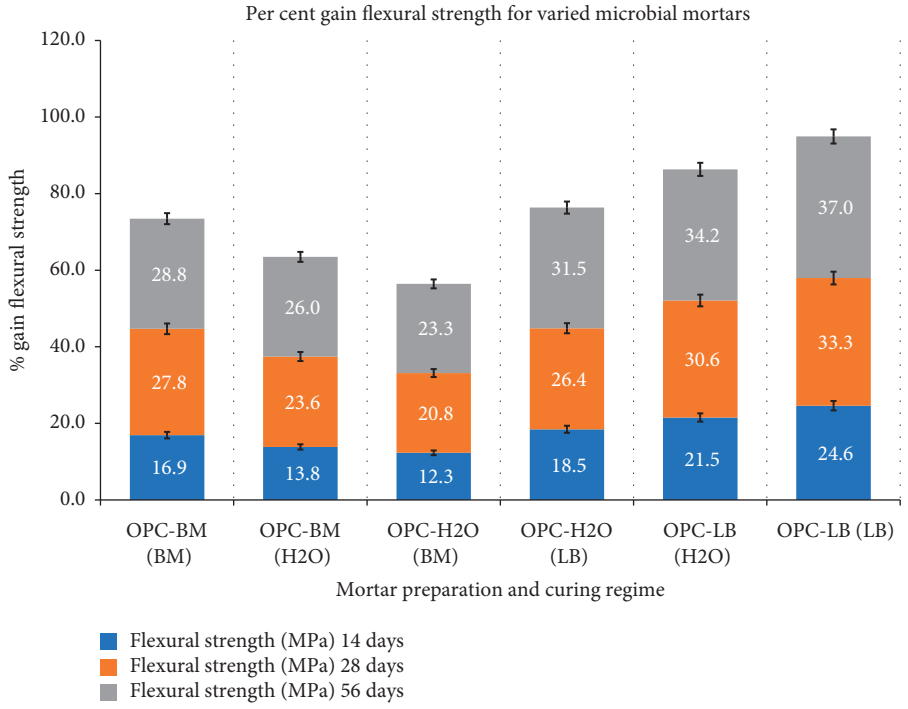

Figure 6: Percent gain flexural strength of test mortars at 14th, 28th, and 56th day of curing.

Table 3: $T_{calc.}$ values summary for microbial mortars against control mortar and among varied microbial mortar categories flexural strength across 2nd, 7th, 14th, 28th, and 56th day of curing ($T_{crit.} = 0.5$, $p = 0.05$).

Mortar categories	$T_{calc.}$ values				
	2nd day $T_{calc} \times 10^{-1}$	7th day $T_{calc} \times 10^{-1}$	14th day $T_{calc} \times 10^{-5}$	28th day $T_{calc} \times 10^{-5}$	56th day $T_{calc} \times 10^{-5}$
OPC-H_2O (H_2O) vs. OPC-H_2O (LB)	5.0	5.0	13.7908	6.8664	0.4725
OPC-H_2O (H_2O) vs. OPC-LB (H_2O)	5.0	5.0	46.4869	4.9426	1.2694
OPC-H_2O (H_2O) vs. OPC-LB (LB)	5.0	5.0	26.6329	6.1408	2.4344
OPC-H_2O (H_2O) vs. OPC-H_2O (BM)	5.0	5.0	4.9845	3.7064	3.9136
OPC-H2O (H_2O) vs.OPC-BM (H_2O)	5.0	5.0	67.1730	9.4017	1.0106
OPC-H_2O (H_2O) vs. OPC-BM (BM)	5.0	5.0	1.2815	1.2371	0.6787
OPC-H_2O (BM) vs. OPC-H_2O (LB)	5.0	5.0	302.5298	302.5298	133.2461
OPC-BM (H_2O) vs. OPC-LB (H_2O)	5.0	5.0	535.0033	38.8954	133.2461
OPC-BM (BM) vs. OPC-LB (LB)	5.0	5.0	22.3619	402.4947	436.5515

stimulate and accelerate the hydration of C-S-H [31, 32, 42].

In this study, it has been found that *Bacillus megaterium* and the *Lysinibacillus sphaericus* biomineralization process enhance the flexural strength. The enhanced MICP process could also be ascribed to the metabolic conversion of the organic acetate added as a microbial feed in form of calcium acetate which was aerobically oxidized under improved alkaline conditions by these ureolytic alkaliphilic *Bacillus* spp. *Lysinibacillus sphaericus* MICP precipitate is more crystalline while that from *Bacillus megaterium* is more amorphous as shown in Figures 3 and 4's SEM images, respectively. Perhaps, the more the crystalline MICP deposits, the more and the better the C-S-H bonding resulting in enhanced flexural strength gain by *Lysinibacillus sphaericus* which deposits relatively more crystalline precipitate than *Bacillus megaterium* which deposits more amorphous precipitates [3, 4, 31, 42]. The amorphous MICP deposition serves as a barrier as it fills any pore/pathway reducing porosity and thus improves impermeability and ingress resistance. Perhaps, this difference in MICP crystallinity and the quantity between the two test bacteria explain why *Lysinibacillus sphaericus* is a better flexural strength enhancer while *Bacillus megaterium* improves impermeability thus a better chloride ingress inhibitor. Similar observations have been made by other researchers, Azadi et al. [6], Chahal et al. [31], Abo-El-Enein et al. [43], and Kim et al. [44] though using other bacteria species. The MICP precipitation occurs according to the following equation [1, 32]:

$$\begin{aligned} CH_3COO^{1-} + 2O_2 &\longrightarrow 2CO_2 + OH^{1-} + H_2O \\ CO_2 + OH^{1-} &\longrightarrow HCO_3{}^{1-} \\ HCO_3{}^{1-} + OH^{1-} &\longrightarrow CO_3{}^{2-} + H_2O \\ \text{Bacterial Cell} - Ca^{2+} + CO_3{}^{2-} &\longrightarrow \text{Cell} - CaCO_3 \end{aligned} \quad (6)$$

Bacillus megaterium and *Lysinibacillus sphaericus* bacteria cause densification of the mortar due to increased cement products, $CaCO_3$, CSH, and ettringite.

3.4. Chloride Ingress

3.4.1. Chloride Profiling. Results for chloride ingress into the test microbial OPC mortars determined at the varied depth of cover within the mortar are presented in Figures 7 and 8 for *Lysinibacillus sphaericus* and *Bacillus megaterium*, respectively.

In all cases, the bacterial presence affected the presence of the Cl^-. As observed, the Cl^- ingress was sharper across all penetration depths in OPC-H_2O (H_2O) than in all microbial mortars up to the 60 mm and 40 mm along the penetration depths, respectively. Perhaps this is due to the lower chloride binding capacity in OPC-H_2O (H_2O) than in microbial mortars [1]. This could be attributed to the increased content of C-S-H and CAH gels that seal the microbial mortar pore connectivity as observed from SEM results above. The reduction in chloride ion in microbial mortars prepared and cured using microbial solution was higher than in the ones either prepared or cured in microbial solutions. This could also be attributed to more MICP precipitates in mortar hydrates, further decreasing the permeability. The trend correlates with that observed by Mutitu et al. [1], Chahal et al. [31], and Nosouhian et al. [45], although involving other types of *Bacillus* spp bacteria. The authors attributed higher chloride ingress in OPC-H_2O (H_2O) than in microbial mortars to continuous and interlinked voids through which the ions ingress.

3.4.2. Chloride Apparent Diffusivity Coefficients. The results obtained from the chloride error function fitting curve for selected mortars OPC-H_2O (H_2O), OPC-BM (BM), and OPC-LB (LB) are summarized in Table 4 showing D_{app} and D_{mig} with corresponding chloride surface concentration (C_s) and r^2 values of the test mortars from the two bacteria under study using 3.5% by mass sodium chloride solution.

OPC-BM (BM) and OPC-LB (LB) mortars exhibited the lowest apparent diffusion coefficient (D_{app}) compared to the other microbial mortars in both BM and LB mortar categories. With low chloride ingress, low D_{app} values were observed. OPC-H_2O (H_2O) mortar had the highest D_{app} value. Lower chloride D_{app} values were demonstrated by *Bacillus megaterium* across all mortar categories than *Lysinibacillus sphaericus* mortars. Perhaps *Bacillus megaterium* could be a suitable internal and external crack healing bacterium than *Lysinibacillus sphaericus* bacteria. This could

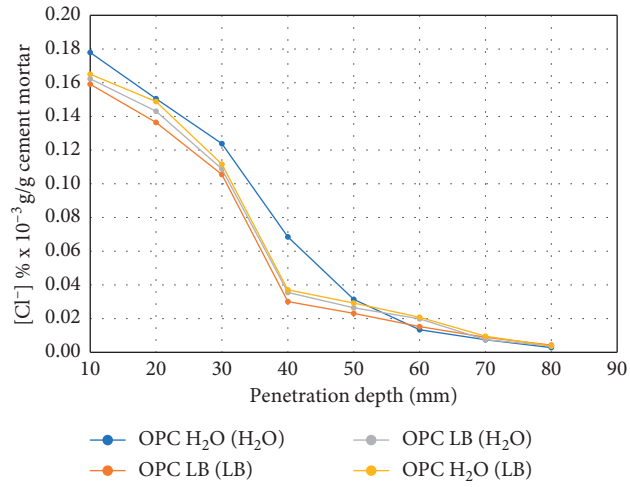

Figure 7: Chloride ion concentration at different depth of penetration for control OPC and varied *Lysinibacillus sphaericus* microbial mortars.

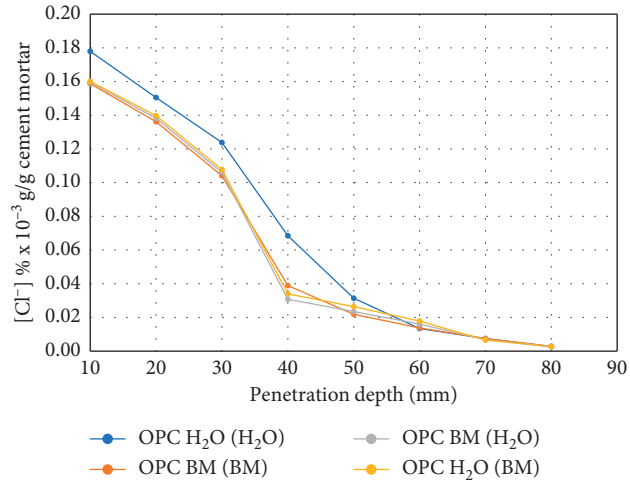

Figure 8: Chloride ion concentration at different depth of penetration for control OPC and varied *Bacillus megaterium* microbial mortars.

be attributed to the MICP deposits present in the microbial mortars which upon reacting with hydration cement products results in additional cementitious material that makes the mortar denser with increased resistivity to Cl^- ingress and lower chloride diffusivity.

4. Conclusions

(1) Both *Bacillus megaterium* and *Lysinibacillus sphaericus* have the ability to precipitate calcium carbonate that improves both flexural strength as well as the pore structure and thus lowering chloride ingress.

(2) Flexural strength of the mortar has a positive correlation with $CaCO_3$ precipitation, for both *Bacillus*

Table 4: C_S, D_{mig}, D_{app}, and r^2–values for different microbial mortars in NaCl.

Mortar type	C_s	$D_{mig.} \times 10^{-9}$ (m^2/s)	$D_{app} \times 10^{-10}$ (m^2/s)	r^2
OPC-H_2O (H_2O)	0.2255	5.6052	2.8430	0.9730
OPC-BM (BM)	0.1997	5.2161	2.6456	0.9655
OPC-BM (H_2O)	0.1965	5.3982	2.7380	0.9523
OPC-H_2O (BM)	0.2000	5.4596	2.7691	0.9555
OPC-LB (LB)	0.2016	5.2764	2.6762	0.9510
OPC-LB (H_2O)	0.2033	5.4801	2.7796	0.9552
OPC-H_2O (LB)	0.2099	5.5213	2.8005	0.9531

megaterium and *Lysinibacillus sphaericus* bacteria. This was exhibited by the higher strengths in microbial mortars cured in cultured solutions than those cured in distilled water.

(3) Lower chloride ingress was observed in both *Bacillus megaterium* and *Lysinibacillus sphaericus* bacteria microbial mortars prepared and cured using cultured solutions than those cured in distilled water. This was exhibited by the lower D_{app} values in microbial mortars cured in cultured solutions than those cured in distilled water. *Bacillus megaterium* bacteria improved the chloride ingress resistivity more than the *Lysinibacillus sphaericus* bacteria.

(4) *Lysinibacillus sphaericus* bacteria improved flexural strength more than the *Bacillus megaterium* bacteria. This was demonstrated by the higher flexural strength as well as higher percent flexural strength gain across all mortar curing ages across all mortar categories than *Bacillus megaterium* mortars. Perhaps *Lysinibacillus sphaericus* could be a better flexural strength enhancer than *Bacillus megaterium* bacteria.

Data Availability

The data used to support the findings of this study are available from the corresponding author upon request.

Conflicts of Interest

The authors declare that they have no conflicts of interest.

Acknowledgments

The authors wish to acknowledge the support granted by various institutions during the experimentation and writing of this paper. The institutions gave access to scholarly repository and library materials, laboratory facilities, and disposables. The institutions include the University of Embu, Kenyatta University, and Savannah Cement Limited, all from Kenya, and the University of Pretoria, South Africa.

References

[1] D. K. Mutitu, O. M. Mulwa, J. M. Wachira, R. Mwirichia, J. K. Thiong'o, and J. M. Marangu, "Effects of biocementation on some properties of cement-based materials incorporating *Bacillus species* bacteria–a review," *Journal of Sustainable Cement-Based Materials*, vol. 8, no. 5, pp. 309–325, 2019.

[2] R. K. Verma, L. Chaurasia, and V. Bisht, "Bio-mineralization and bacterial carbonate precipitation in mortar and concrete," *Journal of Bioscience and Bioengineering*, vol. 1, pp. 5–11, 2015.

[3] C. X. Qian, X. N. Yu, and X. Wang, "A study on the cementation interface of bio-cement," *Materials Characterization*, vol. 59, pp. 1186–1193, 2018.

[4] M. Luo and C. Qjan, "Influences of bacteria-based self-healing agents on cementitious materials hydration kinetics and compressive strength," *Construction and Building Materials*, vol. 4, pp. 1132–1141, 2016.

[5] D. K. Mutitu, *Diffusivity of Chloride and Sulphate Ions into Mortar Cubes Made Using Ordinary Portland and Portland Pozzolana Cement*, Chemistry Department, Kenyatta University, Nairobi, Kenya, 2013.

[6] M. Azadi, M. Ghayoomi, N. Shamskia, and H. Kalantari, "Physical and mechanical properties of reconstructed biocemented sand," *Soils and Foundations*, vol. 57, no. 5, pp. 698–706, 2017.

[7] Z. H. Dong, W. Shi, and X. P. Guo, "Initiation and repassivation of pitting corrosion of carbon steel in carbonated concrete pore solution," *Corrosion Science*, vol. 53, no. 4, pp. 1322–1330, 2011.

[8] T. W. Zewdu and S. Esko, "Service life prediction of repaired structures using concrete recasting method: state-of-the-art," in *Proceedings of the 11th International Scientific Conference on Modern Building Materials, Structures and Techniques, MBMST*, pp. 1138–1144, Vilnius, Lithuania, May 2013.

[9] M. U. Khan, S. Ahmad, and H. J. Al-Gahtani, "Chloride induced corrosion of steel in concrete: an overview of chloride diffusion and prediction of corrosion initiation time," *International Journal of Corrosion*, vol. 2017, Article ID 5819202, 9 pages, 2017.

[10] M. V. A. Florea and H. J. H. Brouwers, "Chloride binding related to hydration products," *Cement and Concrete Research*, vol. 42, no. 2, pp. 282–290, 2012.

[11] P. K. Mehta, *The Durability of Concrete in Marine Environment-A Review, the Performance of Concrete in a Marine Environment*, Vol. 68, ACI Publications, Farmington Hills, MI, USA, 2011.

[12] M. Uysal, K. Yilmaz, and M. Ipek, "The effect of mineral admixtures on mechanical properties, chloride ion permeability and impermeability of self-compacting concrete," *Construction and Building Materials*, vol. 27, no. 1, pp. 263–270, 2012.

[13] T. Luping and J. Gulikers, "On the mathematics of time-dependent apparent chloride diffusion coefficient in concrete," *Cement and Concrete Research*, vol. 37, no. 4, pp. 589–595, 2007.

[14] J. M. Marangu, J. K. Thiong'o, and J. M. Wachira, "Chloride ingress in chemically activated calcined clay-based cement," *Journal of Chemistry*, vol. 2018, Article ID 1595230, 8 pages, 2018.

[15] J. Wang, P. M. Basheer, S. V. Nanukuttan, and Y. Bai, "Influence of compressive loading on chloride ingress through concrete," in *Proceedings of the Civil Engineering Research Association of Ireland (CERAI)*, pp. 28-29, Belfast, UK, August 2014.

[16] J. Crank, *The Mathematics of Diffusion*, Oxford University Press, New York, NY, USA, 2nd edition, 1975.

[17] L. Cheng and R. Cord-Ruwisch, "Selective enrichment and production of highly urease active bacteria by non-sterile (open) chemostat culture," *Journal of Industrial Microbiology & Biotechnology*, vol. 40, no. 10, pp. 1095–1104, 2013.

[18] T. Rasheeduzzafar, E. S. Hussain, and S. S. Al-Saadoun, "Pore solution composition of hydrated cement pastes with reference to corrosion resistance performance of reinforcing steel in concrete," in *Proceedings of the Vetch Middle East NACE Corrosion Conference*, pp. 386–389, Manama, Bahrain, October 2004.

[19] J. M. Wachira, "Chloride ingress in pozzolana based cement," in *Proceedings of the 7th Kenya Chemical Society International Conference*, Kisumu, Kenya, October 2012.

[20] R. Alizadeh, J. J. Beaudoin, and L. Raki, "Mechanical properties of calcium silicate hydrates," *Materials and Structures*, vol. 44, no. 1, pp. 13–28, 2011.

[21] A. Dousti, M. Shekarchi, R. Alizadeh, and A. Taheri-Motlagh, "Binding of externally supplied chlorides in micro silica concrete under field exposure conditions," *Cement and Concrete Composites*, vol. 33, no. 10, pp. 1071–1079, 2011.

[22] C. Theodore and S. Karen, "Alkali fixation of CSH in blended cement pastes and its relation to alkali-silica reaction," *Laboratory of Construction Materials*, vol. 42, no. 8, pp. 1049–1054, 2012.

[23] P. Bamforth, "Concrete classification for RC structures exposed to marine and other salt-laden environments," in *Proceedings of. 5th International Symposium on Structural Faults and Repair*, pp. 31–40, Edinburgh, UK, June 2003.

[24] L. Bertolini, B. Elsner, P. Pedeferri, and R. Polder, *Corrosion of Steel in Concrete: Prevention, Diagnosis, and Repair*, Wiley-VCH Verlag GMbH & Co. KGaA, Weinheim, Germany, 2004.

[25] N. De Belie and J. Wang, "Bacteria-based repair and self-healing of concrete," *Journal of Sustainable Cement-Based Materials*, vol. 5, no. 1-2, pp. 35–56, 2016.

[26] V. N. Rao and T. Meena, "A review of carbonation study in concrete," *IOP Conference Series: Materials Science and Engineering*, vol. 263, no. 3, pp. 1–10, 2017.

[27] K. De Weerdt, D. Orsakova, A. C. A. Muller, C. K. Larsen, B. Pedersen, and M. R. Geiker, "Towards the understanding of chloride profiles in marine exposed concrete, the impact of leaching and moisture content," *Construction and Building Materials*, vol. 120, pp. 418–431, 2016.

[28] O. S. B. Al-Moudi, M. Masleuddin, and Y. A. B. Abdulal, "Role of chloride ions on expansion and strength reduction in plain and blended cement in sulphate environments," *Construction and Building Material Journal*, vol. 13, pp. 38–43, 2011.

[29] J. M. Wachira, J. K. Thiong'o, J. M. Marangu, and L. G. Muriithi, "Physicochemical performance of Portland–rice husk ash-calcined clay-dried acetylene lime sludge cement in sulphate and chloride media," *Advances in Materials Science and Engineering*, vol. 2019, Article ID 5618743, 12 pages, 2019.

[30] J. W. Jeffrey, P. Mondal, and C. M. Mideley, "Mechanisms of cement hydration," *Cement and Concrete Research*, vol. 41, no. 12, pp. 1208–1223, 2012.

[31] N. Chahal, R. Siddique, and A. Rajor, "Influence of bacteria on the compressive strength, water absorption and rapid chloride permeability of fly ash concrete," *Construction and Building Materials*, vol. 4, pp. 98–105, 2012.

[32] Y. C. Ersan, N. Hernandez-Sanabria, and N. De Belie, "Enhanced crack closure performance of microbial mortar through nitrate reduction," *Cement and Concrete Research*, vol. 70, pp. 159–170, 2015.

[33] EN 196-1, *Cement Part 1: Composition, Specifications and Conformity Criteria for Common Cement*, European Union Standards, Beckum, Germany, 2011.

[34] KS EAS 18-1, *Kenya Standard Test Method for Oxides Specification of Hydraulic Cement*, KEBS, Nairobi, Kenya, 2017.

[35] ASTM C 293, *Standards of Flexural Strength of Concrete, Part 3, Effects of Variations in Testing Procedures*, American Society for Testing and Materials, Elservier, London, UK, 1990.

[36] ASTM D7348, *Standard Test Methods for Loss on Ignition (LOI) of Solid Combustion Residues*, ASTM International, West Conshohocken, PA, USA, 2013.

[37] R. H. Bogue, "Chemistry of Portland cement," British Patent No. 5022, pp. 1927–1940, 1977.

[38] K. Scrivener, R. Snellings, and B. Lothenbach, *A Practical Guide to Microstructural Analysis of Cementitious Materials*, CRC Press, Boca Raton, FL, USA, 1st edition, 2017.

[39] ASTM C 1552, *Standard Test Method for Determining Chloride Concentration using Chloride Ion-Selective Electrode*, American Society for Testing and Materials, Elsevier, London, UK, 2005.

[40] C. Andrade, C. Castellote, C. Alonso, and C. Gonzalez, "Non-steady-state chloride diffusion coefficients obtained from migration and natural diffusion tests," *Materials and Structure*, vol. 33, no. 1, pp. 21–28, 1999.

[41] M. S. Vekariya and J. Pitroda, "Bacterial concrete: a new era for the construction industry," *International Journal of Engineering Trends and Technology (IJETT)*, vol. 4, pp. 9–16, 2013.

[42] H. Thiyagarajan, S. Maheswaran, M. Mapa et al., "Investigation of Bacterial activity on Compressive Strength of cement mortar in different curing Media," *Journal of Advanced Concrete Technology*, vol. 14, no. 4, pp. 125–133, 2016.

[43] S. A. Abo-El-Enein, A. H. Ali, A. H. Ali, F. N. Talkhan, and H. A. Abdel-Gawwad, "Application of microbial biocementation to improve the physico-mechanical properties of cement mortar," *HBRC Journal*, vol. 9, no. 1, pp. 36–40, 2013.

[44] H. K. Kim, S. J. Park, J. I. Han, and H. K. Lee, "Microbially mediated calcium carbonate precipitation on normal and lightweight concrete," *Construction and Building Materials*, vol. 38, pp. 1073–1082, 2013.

[45] F. Nosouhian, D. Mostofinejad, and H. Hasheminejad, "Concrete durability improvement in a sulphate environment using bacteria," *Advances in Materials Science and Engineering*, vol. 28, no. 1, Article ID 04015064, 2016.